
Atomic-scale characterization of a model catalytic system

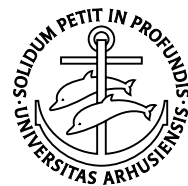
Pd nanocrystals supported
on $\text{Al}_2\text{O}_3/\text{NiAl}(110)$

Kim Højrup Hansen

Ph.D. thesis



Institute of Physics and Astronomy
University of Aarhus, Denmark



Atomic-scale characterization of a model catalytic system

Pd nanocrystals supported
on $\text{Al}_2\text{O}_3/\text{NiAl}(110)$

Kim Højrup Hansen

Ph.D. thesis, January 2001

Institute of Physics and Astronomy
Center for Atomic-scale Materials Physics
University of Aarhus, Denmark

The work described in this thesis has been performed in the STM group at the Institute of Physics and Astronomy at the University of Aarhus. The work has been conducted in the period from February 1, 1998 to January 31, 2001, with Ivan Stensgaard and Flemming Besenbacher as supervisors. The work was made possible through a Ph.D. grant from Center for Atomic-scale Materials Physics.

Acknowledgments

Working in the STM group, together with both people from the group and from outside the group has been a pleasant experience. Especially I would like to thank Peter, with whom I fought against the “Big chamber” and lost. Lars, for helping me getting something out of NiAl waves which I accidentally stumbled upon. Jakob, Željko and Bjørk for theoretical input. Sascha together with whom I first got atomic resolution on top of a nanocrystal. Turid, for cooperation as well as for obtaining some great images of Pd clusters, such as Fig. 4.11. And the three “chiefs” of the group: Ivan, Flemming and Erik for providing a pleasant and inspiring frame around the group.

During my time as a Ph.D. student I spent three months in the STM group at the department of chemical physics at the Fritz-Haber-Institute in Berlin. I would like to thank Marcus and H.-J. Freund for given me the opportunity of working there. And Marcus, Thomas and especially Michael for taking care of me while being in Berlin.

In the last period of my Ph.D. work, I have written this thesis. I would like to thank Stig, Michael and Renald for helping me through the awkwardness of writing it in English as well as for discussing the contents. And Jeanette for providing the final linguistic upgrade.

Tine gets the last, largest and most loving acknowledgment for being a fantastic wife.

List of publications

The publications related to the thesis are listed below. These are referred to with capital roman numerals, whereas others references are cited using arabic numerals and listed in the end of the thesis.

- [I] K. Højrup Hansen, T. Worren, E. Lægsgaard, M. Bäumer, H.-J. Freund, F. Besenbacher, and I. Stensgaard, “Palladium nanocrystals on Al_2O_3 : structure and adhesion energy”, *Physical Review Letters* **83**, 4120 (1999).
- [II] K. Højrup Hansen, J. Gottschalck, L. Petersen, B. Hammer, E. Lægsgaard, F. Besenbacher, and I. Stensgaard, “Surface waves on NiAl(110)”, *Physical Review B* **63**, 115421 (2001).
- [III] K. Højrup Hansen, T. Worren, E. Lægsgaard, F. Besenbacher, and I. Stensgaard, “Bias dependent apparent height of an Al_2O_3 thin film on NiAl(110), and of supported Pd clusters”, *Surface Science* **475**, 96 (2001).
- [IV] T. Worren, K. Højrup Hansen, E. Lægsgaard, F. Besenbacher, and I. Stensgaard, “Copper clusters on $\text{Al}_2\text{O}_3/\text{NiAl}(110)$ studied with STM”, accepted for publication in *Surface Science*.
- [V] K. Højrup Hansen, Ž. Šljivančanin, B. Hammer, E. Lægsgaard, F. Besenbacher, and I. Stensgaard, “An STM and DFT study of the ordered structures of NO on Pd(111)”, in preparation.
- [VI] K. Højrup Hansen, Ž. Šljivančanin, B. Hammer, E. Lægsgaard, F. Besenbacher, and I. Stensgaard, “Oxygen adsorption on oxide supported Pd nanocrystals: overlayer and edge structures”, to be published.

Contents

Introduction and motivation	1
Overview of the thesis	4
List of abbreviations	5
1 The scanning tunneling microscope	7
1.1 Principles of the STM	7
1.2 STM theory	9
1.3 The Århus STM	11
1.4 Remarks on STM images	13
2 The NiAl(110) surface	17
2.1 The NiAl(110) surface	17
2.2 Experimental details	18
2.3 Surface waves	19
2.4 Surface waves on NiAl(110)	20
2.4.1 Fourier transforms	24
2.5 Band structure calculations	25
2.6 Conclusion	27
2.7 End note	28
3 The Al₂O₃ thin film	29
3.1 Bulk alumina	29
3.2 Al ₂ O ₃ films	31
3.3 Preparation of the Al ₂ O ₃ /NiAl(110) film	31
3.4 Structure model of Al ₂ O ₃ /NiAl(110)	33
3.5 Appearance of the film when imaged by STM	34
3.5.1 Positive bias voltage	34
3.5.2 Negative bias voltage	37
3.5.3 Interface	37
3.6 Defect structure	39
3.7 Apparent film height	41
3.8 Vacancy islands	45
3.9 Defect structure of an incomplete film	45
3.10 Conclusion	47

4	Palladium nanocrystals on $\text{Al}_2\text{O}_3/\text{NiAl}(110)$	49
4.1	Experimental details	49
4.2	Nucleation and growth	50
4.3	Crystal shape	51
4.3.1	Wulff construction	52
4.3.2	Wulff theorem	54
4.3.3	Wulff theorem for a supported cluster	57
4.4	Wulff construction for an FCC crystal	59
4.4.1	The facet planes	60
4.4.2	Width of the (111) plane	61
4.4.3	Various features of a free cluster	62
4.4.4	Ratios on a cluster with a (110) facet	63
4.4.5	Ratios on a cluster without a (110) facet	64
4.4.6	A supported cluster	64
4.5	Tip broadening of a 3D cluster	66
4.6	Nucleation and growth of Pd on Al_2O_3	67
4.7	Orientation	71
4.8	Apparent cluster height	73
4.9	Atomic-resolution on the Pd nanocrystals	76
4.10	Planarity of the top facet	80
4.11	Cluster morphology	83
4.11.1	Imperfect nanocrystals	86
4.12	Observed shape vs. Wulff shape	87
4.12.1	Wulff shapes	87
4.12.2	The side length ratio	88
4.12.3	The (110) facet	90
4.12.4	The h/w ratio	91
4.12.5	Growth shape or equilibrium shape?	92
4.13	Adhesion energy	92
4.14	Temperature dependence of cluster morphology	95
4.15	Pd nanocrystals in a high-pressure hydrogen ambient	98
4.15.1	The high-pressure cell	98
4.15.2	The structure of Pd nanocrystals under high pressure	98
4.16	Metals on $\text{Al}_2\text{O}_3/\text{NiAl}(110)$	100
4.17	Conclusion	103

5	Adsorption of oxygen on Pd(111) and on Pd nanocrystals	105
5.1	Experimental details	105
5.2	Oxygen adsorption on Pd(111)	106
5.3	STM imaging of O/Pd(111)	106
5.4	Adsorption of oxygen on Pd nanocrystals	109
5.5	Oxygen on the top facet	110
5.6	The edge atoms	115
5.7	Oxygen-induced edge structures	117
5.8	Removal of oxygen	124
5.9	Conclusion	126
6	Adsorption of nitric oxide on Pd(111) and Pd nanocrystals	127
6.1	Experimental details	127
6.2	Nitric oxide adsorption on Pd(111)	127
6.3	STM imaging of NO/Pd(111)	129
6.3.1	Adsorption at room temperature	129
6.3.2	Adsorption at low temperature	131
6.4	DFT calculations	135
6.5	Discussion of the obtained STM images	135
6.6	Nitric oxide adsorption on the Pd nanocrystals	136
6.7	Conclusion	139
	Conclusion and outlook	141
	Summary	143
	References	146

Introduction and motivation

From ruby to rust metal oxides constitute a versatile and interesting class of materials. They span the entire range from high- T_C superconductors to insulators and seem to be ubiquitous in such different technological applications as corrosion passivation, gas sensing, medical implants, heterogeneous catalysis etc.

The basic understanding of the surface properties of metal oxides is much less developed than that of metals and semiconductors. Several reasons why it is so exist. One major problem is related to the fact that most surface sensitive techniques are electron or ion based [1], and therefore not readily applicable to investigate many of the metal oxides, which are often insulating. Another problem is related to the complexity of metal oxides, originating in their composite nature, in large unit cells and a lack of local order in the surface region. This results in difficulties in producing oxide surfaces with a well-defined and reproducible composition and defect concentration [2]. It is possible to circumvent many of the experimental problems related to bulk oxides and still obtain significant insight into the surface properties by using thin oxide films grown on a suitable substrate as model systems [3–6]. This will be discussed in further detail in section 3.1.

Nanosize metal clusters dispersed on a model oxide support have a fundamental resemblance to a broad class of real catalytic materials, the so-called metal-on-oxide catalysts. This resemblance is the main motivation for the present study. Heterogeneous catalysis has significant impact on the society, which can be illustrated by the fact that more than 90% of the chemical manufacturing processes throughout the world at present utilize catalysts. Much of the food we eat and the medicine we take have at some point run over a catalyst, and virtually all fuels are cleaned by heterogeneously catalysed reactions. Heterogeneous catalysis also plays an important role in minimizing environmental pollution products caused by industry and the modern way of living, e.g. in car exhaust catalysis by being able to convert environmentally toxic fumes to harmless gases [7, 8].

The term *catalysis* was introduced in 1836 by Berzelius but it was Ostwald who formulated the general definition, still valid today: “A catalyst is a substance that accelerates the rate of a chemical reaction without being part of its final products”. The effect of a catalyst is to lower the overall energy

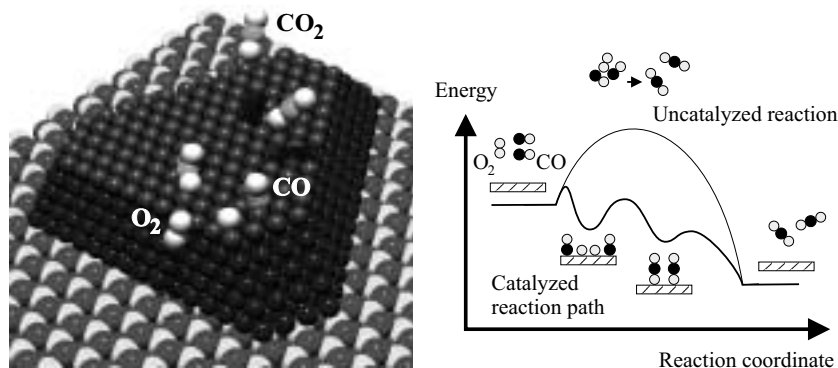


Figure 1: A sketch of a catalytic reaction occurring on top of a supported nanocrystal, along with a diagram of the free energy involved, here exemplified with the reaction $\text{O}_2 + 2\text{CO} \rightarrow 2\text{CO}_2$.

barrier from reactants to products in a chemical reaction. This is obtained by offering an alternative and more rapid reaction path to the final product compared to the reaction without a catalyst. A catalysed reaction usually contains several elementary steps, including adsorption of the reactants on the catalytic surface, breaking of chemical bonds, diffusion, bond formation and finally desorption from the catalyst surface [1]. An example is CO oxidation, which is schematically illustrated in Fig. 1. The first step in the reaction is molecular chemisorption of CO and dissociative chemisorption of O_2 . The latter requires an ensemble of empty neighboring surface sites, and the reaction is inhibited if the surface concentration of adsorbed CO is too high. The second step is the diffusion of CO and O so that they meet and react to form CO_2 . This requires a metal which does not bind the reactants too strongly so that diffusion is suppressed. The final step is desorption of CO_2 . The CO oxidation is catalysed by a Pd surface, but also e.g. Pt, Rh and Ru can be used [8].

An excellent example of a real catalyst which has undergone a huge development and is still being improved is the automotive exhaust catalyst. In the early 70'es the smog level in the larger cities in California became so high that it was necessary to take action. Rather than restricting the use of cars by e.g. raising the price on gasoline, a research effort was initiated, resulting in the invention of the car exhaust catalyst that was implemented from 1975 in

USA and from 1986 in Europe. The automotive catalyst originally consisted of Pt/Rh dispersed on a γ -Al₂O₃ support, but also Pd or mixtures of Pt/Rh with Pd can be used. A drawback of Pd is its much higher sensitivity to poisoning by Pb than Rh and Pt. In USA, where Pb has almost been removed from the gasoline, also Pd is now used, and many different formulations consisting of Pt/Rh/Pd, Pt/Rh, Pd/Rh or just Pd are available in the market today. The γ -Al₂O₃ support is usually mixed with CeO₂ and ZrO₂ for stabilization reasons (and gas storage which will not be discussed here). The purpose of the catalysts is to reduce the level of toxic NO_x, CO and unburned hydrocarbons, by conversion to harmless N₂, H₂O and CO₂. The automotive exhaust catalyst is at present capable of reducing the malign exhaust products with a high efficiency (80-90%). The main challenge for the future will be to increase the efficiency to almost 100% and to somehow circumvent the CO₂ emission which contributes to the green-house effect [9,10].

Real catalysts are extremely complex materials consisting of porous oxide support with a high surface area (100 m²/g) where a few weight percent of nanosize metal clusters are dispersed in the surface region. The catalytic reactions are often performed at extreme conditions with total pressures up to several hundred bar, temperatures of some hundred degrees Celsius and gas speed up to a few thousand km/h [1, 7]. The prospects for complete control over the catalytic reaction, e.g. to obtain higher reaction rates, better selectivity and long term durability, have spurred the surface science community to work for a better understanding of the microscopic processes in heterogeneous catalysis. The complexity of the real catalytic systems, however, hampers a characterization on the atomic level and explains why catalyst developments and improvements are largely based on the “trial and error” method [11].

The surface science approach is to address the catalyst by representing it with idealized model systems. Traditionally, the model systems of choice have been single crystal metal surfaces [12,13]. While a lot has been learned and still can be learned from single crystal studies, the surface science community has now developed the tools to include studies of more realistic sample surfaces such as oxide-supported nanosize metal clusters [2, 4,14,15]. This approach has shown that the catalytic activity can be influenced by several factors: The size of the metal clusters is important. This is partly a geometric effect due to the presence of edges and corners, which may completely dominate the reactivity [14,16], and partly an electronic effect related to different behaviours for small particles in comparison to the bulk material [14,17]. There may be important effects of cross talk between facets of different symmetry or nature [18]. Special

reactive sites may also be created in the interface between the metal particle and the substrate [19] or by an overall strain of the metal cluster such that the local geometry is altered [20, 21].

Among the surface sensitive techniques, the STM has proven to be an important tool in exploring systems at the atomic level [22–24]. In particular, the STM is a promising tool in the attempts to bridge the material and pressure gap that exists between model systems studied under ultra-high vacuum conditions and real catalysts. The metal-on-oxide catalyst is often modeled by nanosize metal particles dispersed on a suitable flat model oxide support. In order to be able to perform STM measurements on such a support, it must be at least partly conducting. This can be accomplished by using either thin oxide films supported on a conducting support or low band gap oxides as support materials [5, 25, 26].

The present thesis is an STM study of Pd nanoclusters dispersed on a thin aluminum oxide film supported on a NiAl alloy single crystal. The main goal is to push atomic-scale experiments to a higher level of complexity without losing resolution. The number of studies of metal clusters supported on oxides and oxide films is rapidly increasing, and so are the studies which include scanning probe microscopy. Many of the scanning probe studies on these types of systems, however, neither exhibit atomic resolution, nor even near atomic resolution.

Palladium was originally chosen because it was known to form nanosize crystallites when deposited on $\text{Al}_2\text{O}_3/\text{NiAl}(110)$ at room temperature [27], and therefore found to be a good candidate of oxide-supported nanoclusters on which atomic resolution could be obtained.

Overview of the thesis

The first chapter is concerned with the experimental technique used in the thesis, i.e. STM. The principles behind the STM are introduced, followed by a description of the experimental implementation of the setup.

The remaining part of the thesis is organized in a “bottom-up” manner. Chapter 2 describes the clean NiAl(110) surface. The NiAl surface can in principle be regarded as “just” the substrate of the thin aluminum oxide film, but the chapter goes beyond that opinion and describes two interesting phenomena taking place at the surface, namely that only one out of the two atomic species in the surface is depicted by the STM, and the presence of standing waves at room temperature.

Chapter 3 describes the thin Al_2O_3 film which is created by oxidation of the $\text{NiAl}(110)$ surface. The thin film is very fascinating due to a strong influence from the applied tunnel parameters. This influence is discussed both with respect to the appearance of the film and the apparent film height. Also the defect structure of the film is discussed.

Chapter 4 deals with palladium nanoclusters supported on the Al_2O_3 film. The chapter starts out in a textbook manner, discussing crystal shapes and provides a short proof of the Wulff construction. After that a rather detailed discussion of the free and supported Wulff construction for an FCC crystal follows. This discussion forms the basis for a morphology and atomic level characterization of the Pd nanocrystals. Then a few measurements of the Pd nanoclusters in a high-pressure of H_2 are discussed, and finally a brief overview of various metals which were studied on the Al_2O_3 film is provided.

The two following chapters, 5 and 6, discuss adsorption of simple molecules on $\text{Pd}(111)$ and on the nanocrystals. Chapter 5 deals with oxygen adsorption. Oxygen on $\text{Pd}(111)$ and on the top facet on the nanocrystals exhibits a strong tip dependence. This tip dependence is described along with the prominent oxygen-induced edge protrusions on the nanocrystals. Chapter 6 deals mainly with the ordered structures of NO on $\text{Pd}(111)$, but a small section concerning the imaging of NO on the Pd nanocrystals is also provided.

The thesis ends with a conclusion and an outlook, and the final chapter contains a summary.

List of abbreviations

In this thesis, the following abbreviations are used: **AES**: Auger electron spectroscopy. **ARUPS**: angle-resolved ultraviolet photoelectron spectroscopy. **DFT**: density functional theory. **DOS**: density of states. **EELS**: electron energy loss spectroscopy. **EXAFS**: extended x-ray absorption fine structure. **FCC**: face-centered cubic. **GGA**: Generalized gradient approximation. **HCP**: hexagonal close-packed. **HRTEM**: high resolution transmission electron microscopy. **LDA**: local density approximation. **LEED**: low energy electron diffraction. **LDOS**: local density of states. **ML**: monolayer. **RT**: room temperature. **STM**: scanning tunneling microscope (or microscopy). **TEM**: transmission electron microscopy. **TPD**: temperature-programmed desorption. **UHV** ultra-high vacuum.

The scanning tunneling microscope

The data presented in this thesis have been obtained in a standard UHV chamber equipped with a variety of surface science tools, such as LEED, AES and TPD. The main tool has, however, been the STM, and only this will be described here.

The scanning tunneling microscope was invented in the early eighties by Binnig and Rohrer at the IBM research laboratory in Zurich [28, 29]. Binnig and Rohrer together with Ruska, who had designed the first electron microscope, were awarded the Nobel prize in 1986. The argumentation for awarding Binnig and Rohrer the Nobel prize was, that the Nobel committee found it “... clear that entirely new fields are opening up for the study of the structure of matter” [30]. The STM has indeed proven to be a very successful characterization tool. The success is due to its ability to obtain real space images of the outermost atoms in a surface, and the STM is today among the most important surface science tools. Still, the STM has limitations. One of the most important limitations is the lack of providing chemical specificity.

According to the Nobel committee press release of 1986 [30], the scanning tunneling microscope is not a true microscope, because it does not give a direct image of the object under investigation. This is true and a very important aspect of the STM since it images the electron density. In the following first an overview of how the STM operates is given, followed by a simple theory of what is imaged with the STM. Then the STM design is presented and finally some remarks concerning STM images are included.

1.1 Principles of the STM

The principle behind the STM is astonishingly simple. A sharp metal tip, normally of W or Pt-Ir, is brought into close proximity of a surface ($\sim 5 \text{ \AA}$). By applying a bias voltage between the tip and the surface, in the range from millivolts to a few volts, a small current, in the nanoampere range, will flow through the vacuum gap. Depending upon the sign of the bias voltage, the current either flows from the sample to the tip, or vice versa. The tunnel current

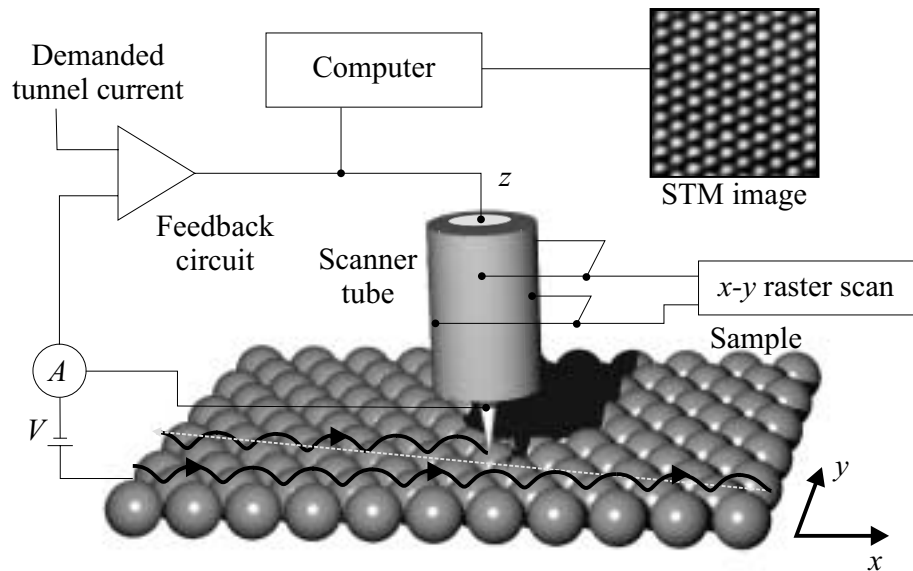


Figure 1.1: Operation principle of the STM. The tip is raster-scanned across the surface by bending a piezoceramic tube (the real height of a scanner tube is ~ 1 cm). A bias voltage is applied between the tip and the sample, such that a small current flows through the vacuum gap. The tunneling current is measured, and a feedback loop compares the measured current with the demanded tunnel current. The tip height is adjusted by contracting or expanding the scanner tube to maintain a constant tunnel current flowing through the vacuum gap.

depends exponentially on the width of the vacuum gap. In the constant current mode, the tunnel current is preset while the tip is raster-scanned across the surface. An electronic feedback loop continuously adjusts the tip height such that the tunnel current is held constant at the preset value. By storing the relative height of the tip as a function of position, an image of the height contours of the scanned area is obtained. An STM is capable of mapping out the height contours of atomic positions when scanning an area of atomic dimensions, but can also probe structures all the way up to micrometer dimensions. The operation principle of the STM is shown in Fig. 1.1.

1.2 STM theory

An exact theoretical treatment of the STM vacuum tunneling is a formidable task, as a proper description of the tunneling potential, the electronic states of both the tip and the surface, and a determination of the vacuum tail of the tunneling electron wave function, must be considered for a strongly interacting system. The interaction between the tip and the surface arises from their close proximity. Furthermore, the shape and chemical composition of the tip are poorly known, and may often even change during scanning. Luckily an exact theoretical treatment is not necessary to grasp the basic physics of the STM. This knowledge can be achieved on the basis of the Tersoff-Hamann theory [31, 32], according to which most STM images can be understood. The theory is based on a perturbative approach developed by Bardeen [33], where the tip and surface are treated as separated entities interacting through a barrier. The interaction is sufficiently weak, such that the tunnel current can be calculated from the wavefunctions of the separated systems and the overlap of the two wavefunctions in the gap region. The tunnel current reads [34]:

$$I = -\frac{2\pi e}{\hbar} \int [f(E_F - eV + \epsilon) - f(E_F + \epsilon)] \times \rho_s(E_F - eV + \epsilon) \rho_t(E_F + \epsilon) |M|^2 d\epsilon \quad (1.1)$$

where the indices s and t refer to the surface and to the tip, respectively. $f(E)$ is the Fermi-Dirac distribution function and ρ is the DOS. The term eV accounts for the applied bias voltage, while M is the tunneling matrix element governing the transition through the gap.

At zero temperature the Fermi-Dirac distribution function is a step function, and the tunnel current expression simplifies to:

$$I = -\frac{2\pi e}{\hbar} \int_0^{eV} \rho_s(E_F - eV + \epsilon) \rho_t(E_F + \epsilon) |M|^2 d\epsilon \quad (1.2)$$

The tunneling matrix element M , is related to the overlap of the sample and tip wavefunctions in the tunneling region, and it was shown by Bardeen that it could be found as [34]:

$$M = -\frac{\hbar^2}{2m} \int_S (\psi_s^* \nabla \psi_t - \psi_t \nabla \psi_s^*) \cdot dS$$

where ψ_t and ψ_s are wavefunctions of the tip and sample in a case without interaction between the two subsystems. The surface integration is over any surface lying entirely within the barrier region.

Tersoff and Hamann evaluated the tunneling matrix elements by use of a 2D Bloch expansion of the surface wavefunction, whereas the tip wavefunction was chosen to have the form of an s -wave. By choosing a proper surface over which to perform the integration, M is found as [31]:

$$M \propto \psi_s(\vec{r}_0)$$

where \vec{r}_0 is a vector pointing to the center of curvature of the tip apex.

In the limit of small bias voltage Eq. (1.2) reduces to:

$$I = \frac{2\pi e^2}{\hbar} V \sum_s |M|^2 \rho_t(E_F) \delta(E_s - E_F) \quad (1.3)$$

where the sum over sample states has not yet been carried out. Inserting the Tersoff-Hamann tunneling matrix element, Eq. (1.3) reduces to [31, 34]:

$$I \propto V R^2 \exp(-\sqrt{8m\phi/\hbar^2} z) n_s(\vec{r}_0, E_F) \quad (1.4)$$

where ϕ is the effective local barrier height, z the width of the gap, and R is the radius of curvature of the tip apex. $n_s = \sum_s |\psi_s(\vec{r}_0)|^2 \delta(E_s - E)$ is the LDOS of the surface. The LDOS should be evaluated at the Fermi level at a position in space right above the surface, in the center of the tip apex. Within this model the constant current STM images are simply contour maps of the LDOS of the surface, unaffected by the presence of the tip. If typical values are inserted in Eq. (1.4) one finds that the current decreases one order of magnitude when the distance between the tip and the surface is increased one Ångström, justifying that the outermost tip atom(s) carry the main part of the tunnel current. For metals the LDOS will in general reveal the positions of the individual atoms in the surface, so that the corrugation of the LDOS directly reflects the geometric structure of the surface [31].

The presence of adsorbates on the surface, however, perturbs the electronic structure in the vicinity of the adsorption site, and thereby the LDOS. As a consequence the adsorbates are imaged as protrusions or depressions in accordance to whether the adsorbate effectively add to or subtract from the LDOS of the bare surface [35, 36]. Thus, an electro-negative atom such as oxygen can actually be imaged as a depression [37].

In the case of tunneling to or from a non-metallic surface, e.g. an oxide surface, it is in general not possible to use the simplified expression, Eq. (1.4), for the tunnel current due to the presence of a band gap. By applying a large enough bias voltage a tunneling current can be drawn. The bias voltage necessary for tunneling is typical around half of the width of the band gap. However, a simple geometric interpretation does not necessarily exist. In practice it has been shown on a variety of non-metal surfaces that the constant current contours of the surface are directly connected to the geometric structure of the surface (for a review of STM on oxides see [24]). In the case of a thin film with a band gap, which resides on a metal substrate, the interpretation is further complicated because the tunnel current primarily originates from the metal substrate, and in general no connection between the constant current contours and the geometric structure can be expected. This will be discussed further in chapter 3 for the thin Al_2O_3 film on the NiAl alloy.

1.3 The Århus STM

The implementation of a working STM rises several technical problems concerning the positioning of two macroscopic objects with a size of centimeters, a few Ångströms apart, and furthermore, how to keep them separated in a controlled way on a sub-Ångström scale.

A schematic drawing of the STM designed and used here in Århus is shown in figure 1.2. The sample (4) is fastened to a tantalum plate, which is clamped into firm contact with the top plate of the STM house by two springs (3). In the beginning the tip was made from a single-crystalline tungsten wire, but later a cheaper poly-crystalline tungsten wire was chosen as no difference in stability or resolution between the two was found. The tip is electrochemically etched to form a sharp apex and mounted onto the scanner tube (6). The scanner tube is made of piezoceramic material which has been coated with gold on both sides. On the outer side the coating is sectioned lengthwise to form four electrodes of equal size, and on the inner side the coating is complete, forming one entire electrode. By applying suitable antisymmetric high voltages to opposite electrodes, the tube bends, and thus a positioning with sub-Ångström precision in the x - y plane is possible. When a high voltage is applied to the inner electrode, the tube will contract or expand, and thus positioning in the z -direction is possible. For the normal scanning mode (constant current mode) a deflection voltage is ramped on the x - y electrodes, while the

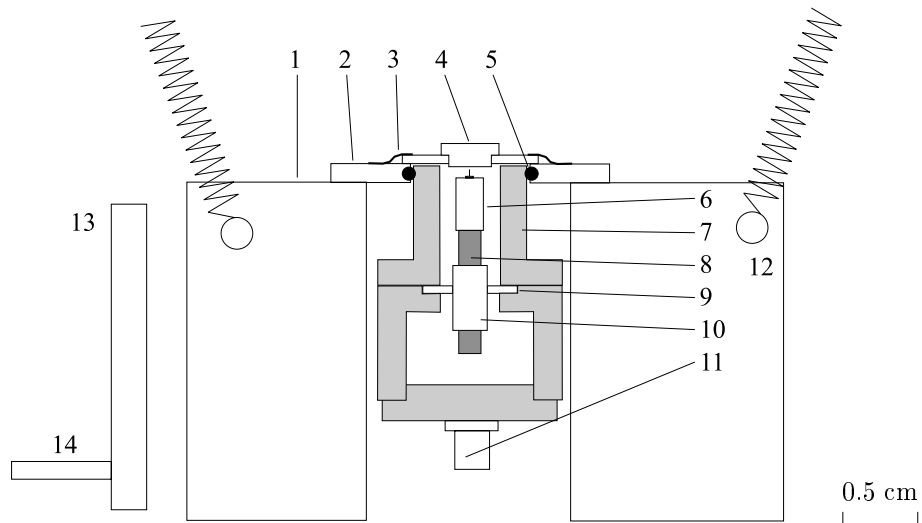


Figure 1.2: Sketch of the Århus STM. (1) Al cradle, (2) top plate, (3) springs, (4) sample and sample holder, (5) quartz balls, (6) scanner piezo tube, (7) STM housing, (8) ceramic rod, (9) ceramic disc, (10) inchworm piezo tube, (11) Zener diode, (12) spring, (13) cold finger, (14) LN₂ feedthrough.

z electrode is used to adjust the height of the tip above the surface so that the tunnel current is kept constant. The scanner tube is glued onto a rod (8) going through another piezo tube used for coarse approach – the inchworm (10). The inchworm consists of three piezo-sections, the upper and the lower section which simply clamp and unclamp respectively, to the rod upon an applied high voltage, and a center section capable of expansion and contraction. By alternately clamping each end of the tube to the rod while expanding or contracting the center part, the scanner tube can be moved towards or away from the sample – in a “worm-like” manner. The tube moves relative to the rod, since the tube is fixed to the STM housing (7) by a ceramic disc. The inchworm can move with around 1 mm/min. The housing is rigidly connected to the top plate (2) through three quartz balls (5) which provide thermal and electrical insulation from the top plate that is held at the bias potential. The top plate is mounted on the cradle (an aluminum block) that is suspended in three springs (12) with a low resonance frequency (2 Hz), effectively damping high frequency vibrations. Due to the compactness of the STM house, the resonance frequency

is around 8 kHz and no further vibrational damping is necessary. The STM design allows for a liquid nitrogen cooling (13, 14) of the aluminum block, and thus the sample, to ~ 120 K, while counter heating the STM by a Zener diode (11) placed at the bottom of the STM house. The counter heating is necessary to keep the STM temperature constant around room temperature as the piezoconstants are highly temperature dependent at lower temperatures. The aluminum block may, also by Zener diodes (not shown), be heated to around 400 K for experiments at elevated temperatures.

The STM is automated and entirely computer-controlled, both with respect to scanning and data acquisition. Typical images contain 256×256 measured points and can be recorded in a time interval ranging from 1 second and up to a few minutes. The setup allows for *in-situ* tip cleaning by applying small voltage pulses or current pulses to the tip, as well as the possibility of modifying the tip character by more or less controlled tip indentations into the surface.

In many respects the STM works as a black box under fatherly surveillance of Erik Lægsgaard.

1.4 Remarks on STM images

An example of an STM image is given in Fig. 1.3(a). The image shows Pd nanocrystals on the Al_2O_3 film. Like most images presented in this thesis this image is a grey-scale representation of a constant current image. A 3D image of the cluster is shown in (b). In the figure caption, all images contain information of the format: $300 \times 300 \text{ \AA}^2$, $U_s = 1.1 \text{ V}$, $I_t = 1.6 \text{ nA}$, which denotes the size of the image, the applied bias voltage and the demanded tunnel current. Bias voltage is, as mentioned above, applied to the sample with the tip at virtual ground, i.e. electrons will, at positive bias, tunnel from filled tip states into empty sample states.

When working with STM one should be aware of different factors that may distort the obtained images. Piezo creep is normally not present on the images which are shown, piezo creep is due to presence of a time constant involved in the response of the piezos to a rapid and/or large voltage change. After changing scanning position, scale or bias voltage the first few images may, thus, be distorted. Thermal drift can have a similar effect.

A major problem when working with the STM is the lack of control over the exact character of the tip. To obtain good images, one needs a “good” tip, but there is no clear recipe on how to obtain a such. Luck has a lot to

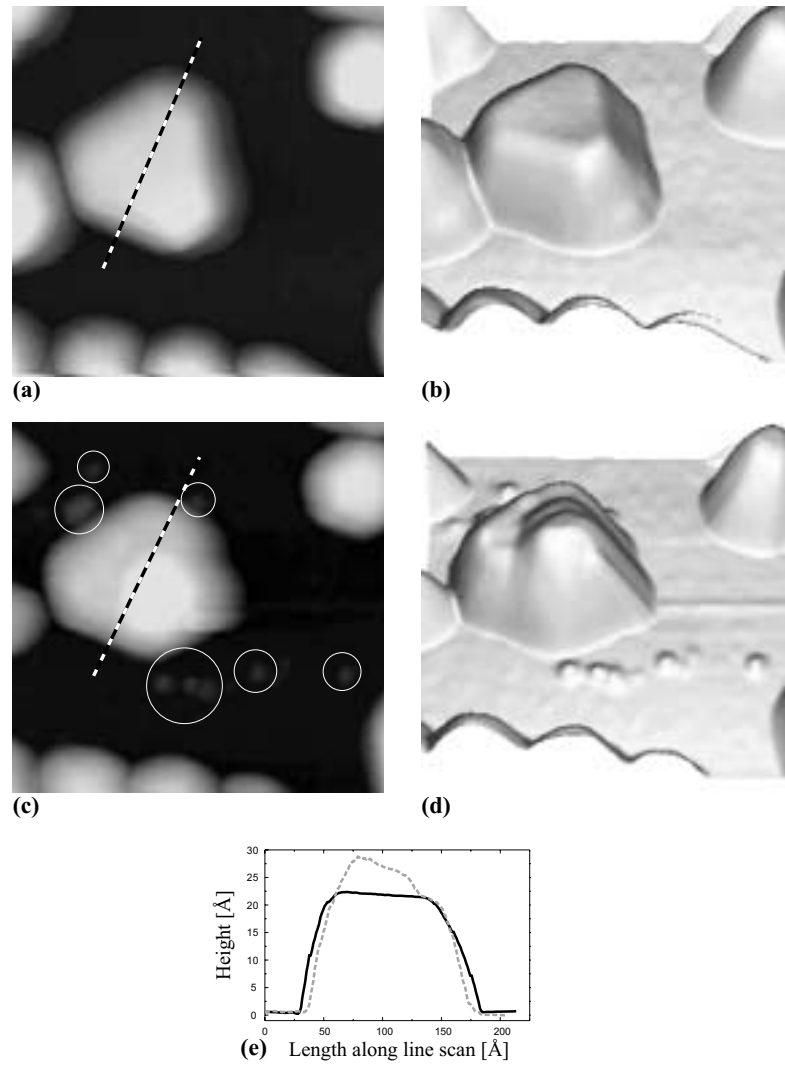


Figure 1.3: STM images of the same cluster. $300 \times 300 \text{ \AA}^2$, $U_s = 1.1 \text{ V}$, $I_t = 1.6 \text{ nA}$. (a) An image showing Pd clusters residing on the Al_2O_3 film. (b) A 3D view of (a). (c) The same clusters as those in (a), but after the tip has dropped material. (d) A 3D view of (c). (e) Line scans along the indicated lines in (a) and (c).

do with it, and perseverance and experience will help, too. A tip change may be induced by the operator to improve the resolution and/or the stability, but sudden unwelcome changes, which may destroy the resolution or, at worst, even the entire scanned area, often occur. An example of the large impact of a sudden tip change upon the scanned area is given in Figs. 1.3(c) and (d). The images are counterparts of the images presented in (a) and (b), in the sense that it is a 2D and 3D view of the same cluster, after a tip change right on top of the Pd nanocrystal has occurred. The tip has dropped some material, both on top of the cluster, and scattered around in the vicinity of it. In (e) two line scans are presented along the indicated line segments.

Another and more harmless tip effect is the inverse corrugation effect [34] which is present on some of the images presented in this thesis. When scanning with atomic resolution, protrusions are often imaged as depressions, and vice versa. The effect is only present on images exhibiting atomic resolution and is related to the orbital character of the tip apex. Clear atomic resolution is obtained when the orbital character of the tip apex is sharply pointed, e.g. the lobe of a d_{z^2} orbital. But the orbital character of the tip apex may as well be ring-shaped, e.g. like a d_{xz} state, which results in an inverse imaging [34].

Finally, one should be aware that the local character of the STM may lead to conclusions that are not representative of the general case, i.e. the whole surface; this is normally referred to as tunnel vision.

The NiAl(110) surface

The present chapter deals with the NiAl(110) surface. The NiAl(110) surface serves as the substrate on which the thin Al_2O_3 film is formed. The Al_2O_3 film is in itself non-conducting, therefore the metallic nature of the NiAl becomes important for the tunneling process. The bare NiAl surface is usually imaged in the course of checking the cleanliness of the system e.g. after a chamber opening, and atomically resolved images of the NiAl(110) surface are naturally used for calibrating the system. The clean NiAl(110) surface is an interesting system, e.g., two atomic species are present in the surface, but only one atomic species is depicted by the STM, and the surface shows the presence of standing waves at room temperature.

In the following data concerning the NiAl alloy are first presented. Then a discussion of the STM images of the NiAl(110) surface follows. The results presented in this chapter are from Ref. [II].

2.1 The NiAl(110) surface

NiAl is one of the several ordered nickel-aluminum alloys [38]. It has a CsCl structure, i.e. two interpenetrating simple cubic lattices of Ni and Al forming a body-centered cubic lattice. A sketch of the NiAl unit cell is shown in Fig. 2.1. The melting point of NiAl is quite high, $T_m = 1638\text{ }^\circ\text{C}$ [38]; higher than the melting points of both Al ($T_m = 660\text{ }^\circ\text{C}$ [38]) and Ni ($T_m = 1455\text{ }^\circ\text{C}$ [38]). The NiAl(110) termination (see Fig. 2.1) consists of 50% Ni and 50% Al. The outermost Al-atoms are, however, displaced 0.22 \AA outwards with respect to the outermost Ni-atoms, as it has been determined by LEED measurements, which also confirmed that the surface composition is nominally stoichiometric [39].

An atomically resolved STM image of the NiAl(110) surface is shown in Fig. 2.2(a). As can be seen from the image only one of the atomic species is depicted by the STM as no center atom is observed in the rectangular unit cell. The chemical identity of the atoms imaged is *a priori* unknown, but due to the high LDOS of the Ni $3d$ states in the vicinity of the Fermi level [40], it could be speculated that the Ni atoms are preferentially imaged. However, the

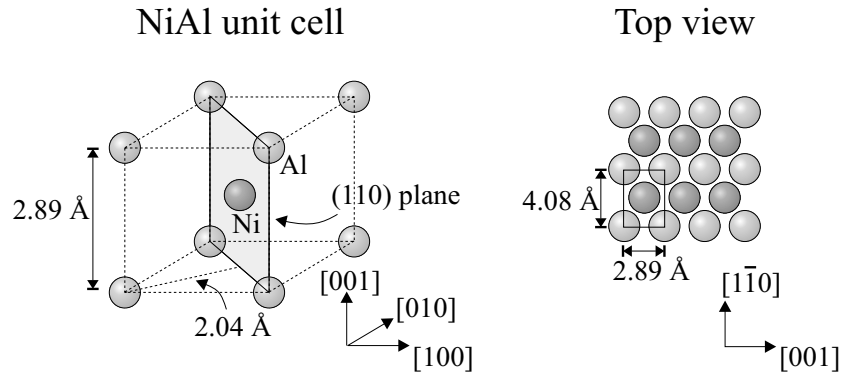


Figure 2.1: Ball models showing the 3D unit cell and a top view of the (110) plane.

Ni d -states are localized and decay rapidly away from the surface compared to the Al sp -states. In the STM it is therefore the more extended Al sp -states which contribute the most to the constant current images. This is shown in the simulated STM image presented in the inset in Fig. 2.2(a). The image was simulated by J. Gottschalck, using the DOS obtained from DFT calculations and a Tersoff-Hamann simulation scheme [31,32]. The decay of the d -states is illustrated in Figs. 2.2(b) and (c), which show two gray-scale representations of the state density *parallel* to the surface, calculated at two different heights above the surface. The contour plot in (b) is obtained close to the surface and the Ni d -character dominates. The contour plot in (c) is for a plane 2 Å above the surface and the more extended sp orbitals of the Al states now dominate. A strong localization of d -orbitals on transition-element surfaces has previously been pointed out by Lang [41].

2.2 Experimental details

The NiAl(110) surface is cleaned by cycles of ion sputtering and annealing. Either neon or argon ions were used for the sputtering, the time depended on the history of the sample. The sample was usually sputtered for 15 to 60 minutes at 1 to 2 kV (15 min. if the NiAl had not been exposed to oxygen, 20-30 min. if a film had been prepared, and up to 60 min. if metals had been deposited). The

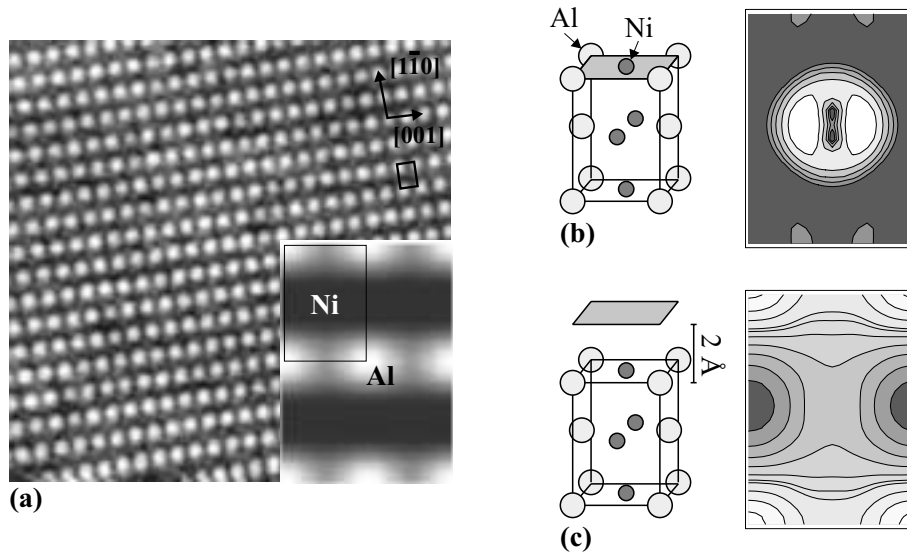


Figure 2.2: (a) STM of the NiAl(110) surface showing atomic resolution. $70 \times 70 \text{ \AA}^2$, $U_s = -6 \text{ mV}$, $I_t = -0.6 \text{ nA}$. Inset: Simulated STM images of NiAl(110). (b) and (c) Linear gray-scale representations of the state density parallel to the surface, calculated at the surface and 2 \AA above the surface. Inset, (b) and (c) by J. Gottschalck.

crystal was annealed to $1000 \text{ }^\circ\text{C}$ for 10 minutes by a combination of radiation heating and electron bombardment of the sample from a hot tungsten filament placed just behind the sample.

After a chamber opening it can be quite hard to obtain a clean surface with large terraces. By preparing a few oxide films (as described in section 3.3), the cleanliness can be improved and terraces as large as $2000 \times 2000 \text{ \AA}^2$ can be obtained. The NiAl surface was normally accepted to be clean if only a few point defects could be detected on a $\sim 1000 \times 1000 \text{ \AA}^2$ scale in the STM.

2.3 Surface waves

Prior to the discussion of how the presence of surface states affects the acquired STM images, a brief introduction to surface waves will be given here.

A thorough overview can be found in Refs. [42, 43].

At a crystal surface special electronic states may exist due to the lack of translational symmetry perpendicular to the surface. These surface states are localized perpendicularly to the surface and their wave functions decay exponentially into the bulk as well as into the vacuum [44]. In the surface plane, surface states may give rise to a quasi, two-dimensional, free-electron gas, which plays an important role for the screening of impurities. When electrons with a wave vector: $q = k_F$, scatter from impurities, they interfere with themselves, creating a quantum mechanical interference pattern in the form of a standing wave. In other words, the electron gas sets up screening waves in order to minimize the influence of impurity potentials, e.g. from point defects or step edges. These screening waves are standing waves in the charge density and are known as energy-resolved Friedel oscillations [43, 45]. In STM images it is the LDOS which is observed. The LDOS depends on the square of the wave function, which gives rise to a factor of two in the wave length, resulting in standing waves in the LDOS with a wave vector $q = 2k_F$.

Surface states crossing the Fermi level give rise to a surface Fermi contour, in complete analogy with the bulk Fermi contour. According to the Tersoff-Hamann model, STM images obtained at low bias are maps of the LDOS at the Fermi level evaluated at the tip apex. By Fourier transforming the LDOS at the Fermi level, only waves with a wave vector of $q = 2k_F$ will contribute [45]. This allows for an interpretation of STM images containing standing waves, as images of standing waves in the Fermi level LDOS due to screening of impurities. The Fourier transform of such an image directly yields the surface Fermi contour scaled with a factor of two [43, 45].

2.4 Surface waves on NiAl(110)

When the NiAl(110) surface is imaged with STM at RT, the typical image shows a blurred atomic resolution. In fact, as it will be discussed below, a such blurred image is a “superposition” of an atomically resolved image and an image of the standing waves in the LDOS. It is, however, some times possible to obtain images that are dominated by either atoms or waves. Examples of the two types are shown in Fig. 2.3.

Figure 2.3(a) appears at first sight to be an ordinary atomically resolved STM image, but it does in fact also contain a standing wave (this will be shown below). The image in Fig. 2.3(b) is obviously dominated by standing waves,

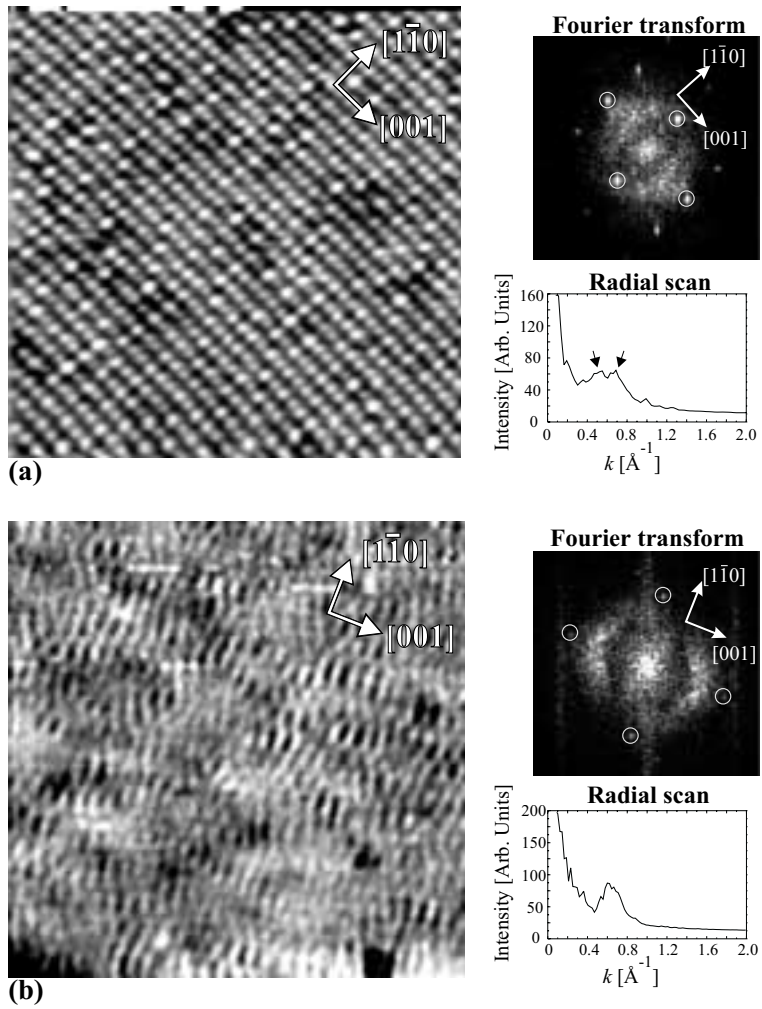


Figure 2.3: STM images of NiAl(110), with corresponding Fourier transforms and radial scans of the Fourier transforms. Both images were acquired at RT. (a) Image showing atomic resolution. $100 \times 100 \text{ \AA}^2$, $U_s = -0.9 \text{ mV}$, $I_t = -1.1 \text{ nA}$. (b) Image showing standing waves. $150 \times 150 \text{ \AA}^2$, $U_s = 743 \text{ mV}$, $I_t = 0.9 \text{ nA}$.

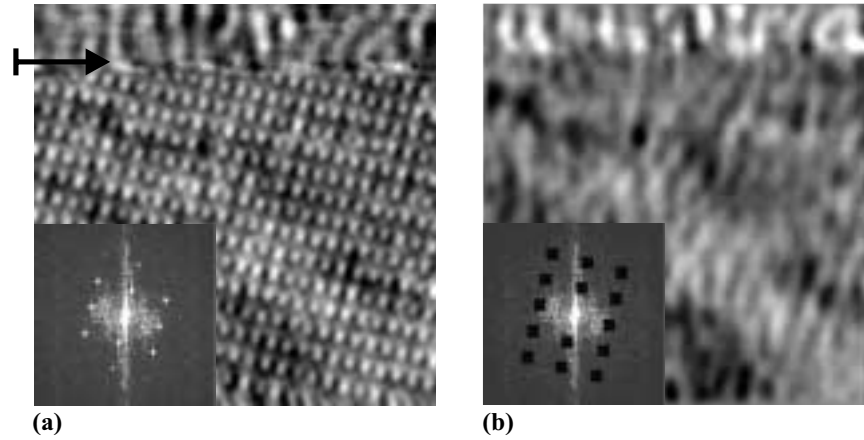


Figure 2.4: (a) STM image showing a tip change causing a shift from imaging atoms to imaging waves. $70 \times 70 \text{ \AA}^2$, $U_s = -1.8 \text{ mV}$, $I_t = -1.3 \text{ nA}$. (b) Modified real space image obtained by removing the lattice spots in the Fourier transform of the image in (a), and performing an inverse Fourier transform.

and the wave pattern completely overshadows the underlying lattice. The (110) face of NiAl is remarkable in the sense that standing waves can be detected at high bias. The image in Fig. 2.3(b) was acquired at a bias voltage of 0.7 V , which is the highest positive bias voltage with which wave images were acquired. The largest negative bias voltage, at which standing waves were observed, was -0.4 V . Still, most images exhibiting standing waves were acquired at low bias, and if the bias voltage was turned up, the waves usually faded away in a manner similar to the one observed when imaging with atomic resolution on a clean metal surface. No correlation between tunnel parameters and image appearance (atoms vs. waves) has been observed. The different imaging modes are solely determined by the detailed character of the tip, of which we have little control. This is illustrated in Fig. 2.4(a), showing an image with atomic resolution (lower part), but after a tip change waves are imaged (upper part). Since no tunnel parameters were changed, the shift from atoms to waves clearly shows that the tip character is decisive for the imaging mode. The inset displays the Fourier transform of the image. Figure 2.4(b) is a modified real space image

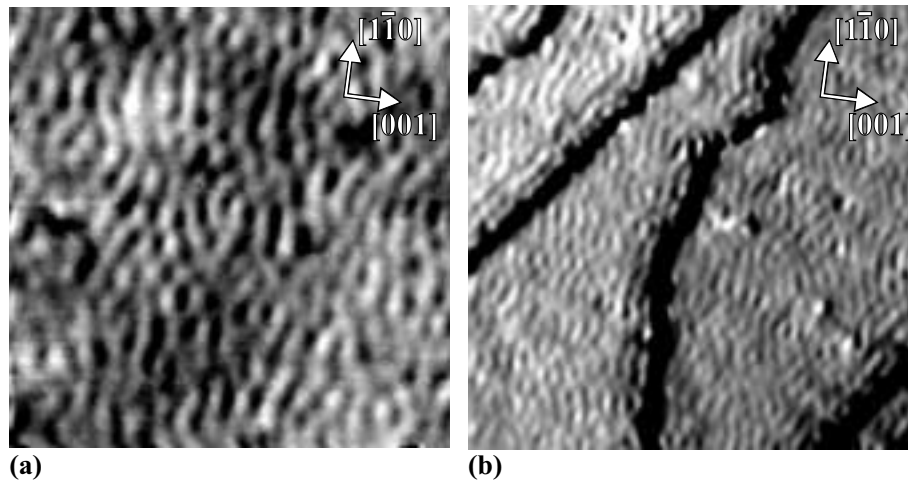


Figure 2.5: STM images of NiAl(110) obtained at 140 K. (a) $100 \times 100 \text{ \AA}^2$, $U_s = -1.8 \text{ mV}$, $I_t = -1.2 \text{ nA}$ (b) $200 \times 200 \text{ \AA}^2$, $U_s = -2.1 \text{ mV}$, $I_t = -1.3 \text{ nA}$.

obtained by removing the lattice spots in the Fourier transform of the image in (a), and performing an inverse Fourier transform. The image now shows waves on the entire surface, which once again illustrates the dual nature of the STM images.

In contrast to the case of the NiAl(110) surface, standing waves are usually detected only at temperatures below 150 K. STM images of NiAl(110) have also been acquired at 140 K. At this temperature, standing waves completely dominate the STM images and only fragments of “atom” images could be obtained. No qualitative difference between wave images acquired at low temperature and at RT is found, which can be verified by comparison of Fig. 2.5(a) and Fig. 2.3(b).

At zero temperature, only electrons in the energy window E_F to $E_F + eV$ contribute to the tunneling current. At “high” temperatures the Fermi-Dirac distribution is broadened, allowing electrons with energies slightly outside the energy window $[E_F, E_F + eV]$ to contribute to the tunneling current. Due to the dispersion $E(k)$ of the surface state, this leads to a broadening of the distribution of k -vectors contributing to the standing wave pattern. The coherence

length of the standing wave is of the order: $l_c \propto 1/\Delta k$ [43], and the broadening results in a faster decay of the waves. Similarly, high bias voltages result in electrons from a broad energy window contributing to the STM image, and again, this leads to a broad distribution in k -space and consequently a rapid decay of the waves. The observation of standing waves in constant current images obtained at bias voltages in the volt regime has to our knowledge never been reported before, and is not yet understood.

In the case of standing waves on, e.g., Cu(111), Au(111) and Be(10 $\bar{1}$ 0) [42], point defects and step edges influence the standing wave pattern. This is not the case for the waves observed on NiAl(110). Only at the very rim of the step edge are the standing waves observed to be aligned with the step. This is shown in Fig. 2.5(b), which has been acquired at 140 K and shows an area with a high step density, along with a few point defects. The image has been slightly differentiated in order to simultaneously show the waves on all terraces. In general, extremely few point defect are observed on NiAl images that exhibit standing waves. However, as can be verified on standing wave images of Cu(111) where every point defect is imaged very prominently, a defect concentration of only 0.1% or less is needed to sustain a standing wave [46].

2.4.1 Fourier transforms

In order to extract information about the wavelength of the standing waves, the STM images are Fourier transformed [45]. The Fourier transforms are presented in Fig. 2.3. Light colors imply large Fourier components. In the following the interpretation of these transforms is discussed.

In the Fourier transform of Fig. 2.3(a), the lattice spots are easily recognized (marked with circles), but in addition two areas with large Fourier components are seen in the $\langle 001 \rangle$ direction. The two ring sections are at first sight more easily recognized on the radial scan. The presence of two such ring sections demonstrates that two standing waves with different wavelengths are superimposed onto the “atom” image of Fig. 2.3(a). As the ring sections in the Fourier transform are incomplete, the corresponding standing waves propagate anisotropically (the surface Fermi contour is anisotrope), mainly in the $\langle 001 \rangle$ direction, and not at all in the $\langle 1\bar{1}0 \rangle$ direction. It is the presence of the superimposed standing waves which gives rise to the intensity variations in Fig. 2.3(a), as can be verified by removing the ring sections in the Fourier transform and performing an inverse transform to obtain a modified real space image.

In the Fourier transform of Fig. 2.3(b), only weak lattice spots are present

as the underlying lattice in the STM image is overshadowed by the standing wave pattern. Again large Fourier components are found in the $\langle 001 \rangle$ direction, but apparently only one broad ring section is present. The analysis of a large number of images shows convincingly that three situations arise: (i) Situation where two ring sections are clearly present (e.g. Fig. 2.3(a)). The inner ring section is always the most intense and is more extended in angle. (ii) Situations where apparently only one broad ring section is present (e.g. Fig. 2.3(b)). It is in this case, however, always possible to decompose the ring section into two underlying distributions centered around the same values as those with two separate ring sections. (iii) Finally, a few cases exist where only one rather narrow ring section can be observed, and here the wavelength corresponds to that of the inner ring section. The presence of two ring sections is similar to the case of standing waves on Au(111), where two complete rings were observed [46]. On Au(111) the inner ring was identified as the Fermi contour of the surface state, whereas the outer ring occurred due to contributions to the screening waves from electrons from the bulk Fermi surface edge. The DFT calculations presented below show that it is possible to make the same identification for the ring sections observed in the Fourier transforms of the STM images of NiAl(110). Using the lattice spots in the Fourier transforms for calibration, the radii of the two ring sections are measured and yield:

$$\begin{aligned} k_{\text{F,outer}} &= 0.72 \pm 0.08 \text{ \AA}^{-1} & (\lambda = 4.4 \text{ \AA}) \\ k_{\text{F,inner}} &= 0.55 \pm 0.04 \text{ \AA}^{-1} & (\lambda = 5.7 \text{ \AA}) \end{aligned}$$

The Fourier transforms presented are of STM images acquired at RT. Fourier transforms of low temperature STM images show no quantitative differences with respect to the appearance or the position of the ring sections.

2.5 Band structure calculations

Density functional band structure calculations have been performed by J. Gottschalck in order to explain the standing waves observed on the NiAl(110) surface. The calculations are only summarized here, but they are presented in their full extent in Ref. [II]. Band structure calculations can, however, only be performed in high symmetry directions, and the entire surface Fermi contour cannot be produced.

The band structure of NiAl(110), including surface, states has been reported earlier by Lui *et al.* [47]. A surface state in the bulk band gap in the $\langle 001 \rangle$

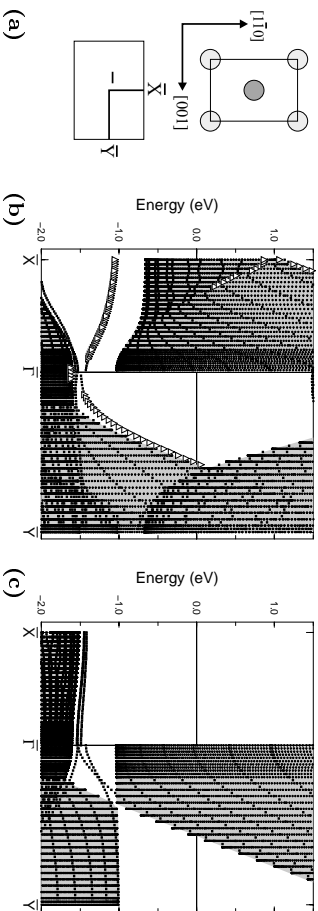


Figure 2.6: Band structure of NiAl(110) as calculated by J. Gottschalk; triangles indicate surface states, and dots indicates bulk states. (a) The NiAl(110) unit cell and corresponding surface Brillouin zone, with the two high symmetry directions $\bar{X} - \bar{\Gamma}$ and $\bar{\Gamma} - \bar{Y}$ (b) Even-state band structure. (c) Odd-state band structure.

direction was found, but the state did not cross the Fermi level. In their calculations Lui *et al.* used the experimental values [39] for the relaxation, which could influence the position of the surface state. In order to compare the STM results with theoretical data, a new band structure calculation was carried out.

Due to the symmetry of the crystal (see Fig. 2.6(a)), the single electronic states along the $\bar{X}\bar{\Gamma}\bar{Y}$ direction can be separated into even and odd states, corresponding to the mirror symmetry perpendicular to the k -vector. The band structure split in even and odd states is shown in Fig. 2.6. The figure contains both bulk and surface states. The states highlighted with triangles, are states with more than 8% of the weight further than 1 Å away from the slab. This somewhat strange identification is a practical way of detecting surface states from a calculation. It detects, however, both surface resonances and surface states. The highlighted state crossing the Fermi level has been verified to be a true surface state. As can be seen on Fig. 2.6, the even states contain both a surface state and a bulk edge which cross the Fermi level, whereas the odd band structure contains only a bulk edge that crosses the Fermi level. In the $\bar{X}\bar{\Gamma}$ direction, corresponding to the $\langle 1\bar{1}0 \rangle$ direction in real space, no bulk band gap is found for the even state and there are no odd states near the Fermi level. This is the reason why no surface waves propagate in that direction. In the $\bar{\Gamma}\bar{Y}$ direction, corresponding to $\langle 001 \rangle$ in real space, it is found that the bulk edge (BE) and the surface state (SS) cross the Fermi level:

$$\begin{aligned}
k_{F,BE} &= 0.63 \pm 0.03 \text{ \AA}^{-1} & (\lambda = 4.99 \text{ \AA}) \\
k_{F,SS} &= 0.62 \pm 0.02 \text{ \AA}^{-1} & (\lambda = 5.07 \text{ \AA})
\end{aligned}$$

Within the uncertainty, the BE crossing is at the same value of k for even and odd states.

Good agreement is obtained for the magnitude of the Fermi wave vectors, but as can be seen, some discrepancy between the calculated and measured values exists in the separation of the two states. The reason for this is a little unclear, but it is proposed that one reason could be the approximative exchange-correlation description employed in every density functional calculation. When the surface state is studied using LDA, no crossing of the surface state with the Fermi level is found [47]. By the use of a more accurate non-local GGA exchange-correlation description in the calculation, a crossing of the surface state with the Fermi level is found, i.e. qualitative agreement between experiment and theory is obtained, but maybe the GGA is not sufficiently accurate to also give quantitative agreement.

2.6 Conclusion

The present chapter mainly dealt with the two phenomena observed on the NiAl(110) surface: (i) only one out of the two atomic species in the surface is depicted by the STM, and (ii) the presence of standing waves at room temperature.

The atomic species depicted by the STM are found to be Al. The Ni d -character is localized and decays rapidly outwards; therefore the more extended Al sp -character dominates the constant-current STM images.

The standing waves can be imaged at both RT and low temperature. At 140 K, the standing waves dominate the STM images, whereas at RT both “atom” images and “wave” images can be obtained. It was shown that the character of the tip is decisive for the imaging mode. The strong influence of the tip on the appearance of the obtained STM images is a recurring topic in this thesis, but only in this chapter was it possible to show this as unambiguously as with Fig. 2.4(a).

The standing waves were analyzed by means of Fourier transforms of the STM images. From the Fourier transforms it was found that waves with two

different k -vectors are present. By means of band structure calculations the origin of the two standing waves was assigned to the surface state and the edge of the projected bulk bands. Good agreement was obtained only for the magnitude of the surface Fermi wave vector, whereas some discrepancy existed between the experimentally observed and the calculated separation of the two wave vectors.

2.7 End note

In the final phase of my thesis preparation I became aware of a preprint by Song *et al.* [48], which was submitted and accepted more or less simultaneously with the submission and acceptance of Ref. [II]. This paper also describes an STM investigation of surface waves on NiAl(110). Since it became available very late in the preparation process, it has not been taken into consideration in the above discussion. Here, the main point will be briefly considered.

The investigation was conducted at 4 K, and waves dominated the surface. Song *et al.* could, however, image the close-packed surface rows by scanning at a bias voltage above +1.5 V. These high-voltage images reveal a surprisingly large number of point defects. The wave images appear similar to the images presented here. The setup allowed for dI/dV measurements, and it was possible to obtain images in a limited bias interval of 100 mV around a certain bias voltage. By Fourier transforming the dI/dV images, Song *et al.* derived the surface Fermi contour including only waves from this limited bias interval, and thereby mapped the surface k -vector dispersion. Two types of Fermi contours were presented. A broad contour very similar to the contours presented in this chapter, and narrow contours obtained at low bias showing contributions from waves running in all directions. Song *et al.* find: $k_F = 0.61 \text{ \AA}^{-2}$ in the $\bar{\Gamma} - \bar{Y}$ direction, in good agreement with our theoretical value.

At the moment it is not clear how a detailed comparison between the two investigations can be made. The main concern is our decomposition into two ring sections, a feature Song *et al.* do not mention. This may question our assignment of the two k -vectors to contributions from the surface state and the bulk edge. Whereas the Fourier transforms which show a broad ring section (Fig. 2.3(b)) may not necessarily have to be decomposed into two contributions, the clear splitting on some of the Fourier transforms (Fig. 2.3(a)) can not readily be understood if the bulk edge, and thus a second k -vector, is not included in the interpretation.

The Al_2O_3 thin film

The present chapter deals with the thin Al_2O_3 film which serves as a model support for bulk alumina. First a general overview of some of the bulk alumina phases is given. The preparation of the $\text{Al}_2\text{O}_3/\text{NiAl}(110)$ thin film is then described, after which the structure model is briefly reviewed. The remains of the chapter will deal with tunneling on the thin film. The results presented in section 3.7 and 3.8 are from Ref. [III].

3.1 Bulk alumina

Alumina forms a large variety of phases, all written as Al_2O_3 , but often relatively large amounts of other compounds, such as water and alkali oxides, are also present. The alumina phases are usually obtained by dehydration of various aluminum hydroxides. The two most important ones are gibbsite, an aluminum-trihydroxide: $\text{Al}(\text{OH})_3$, and boehmite, an aluminum-oxidehydroxide: $\text{AlO}(\text{OH})$ [49]. The dehydration is done by heating the aluminum hydroxide in air (calcination) or in UHV. All aluminum oxides consist, in principle, of a more or less close-packed oxygen sub-lattice in which the Al-cations occupy tetrahedral and/or octahedral interstitial sites [7,50].

Among the many alumina phases, three will be accentuated here: $\alpha\text{-Al}_2\text{O}_3$, $\gamma\text{-Al}_2\text{O}_3$ and $\theta\text{-Al}_2\text{O}_3$. The α -phase is the most stable of the alumina phases. It has a slightly distorted hexagonal close-packed oxygen sub-lattice, where the aluminum ions occupy octahedral vacancies. $\alpha\text{-Al}_2\text{O}_3$ is the final dehydration product of both the aluminum-trihydroxide and the aluminum-oxidehydroxide, when heated above 1200 °C in air [7, 49]. The few single crystal surface terminations of alumina bulk samples which were successfully prepared are all terminations of $\alpha\text{-Al}_2\text{O}_3$ [2]. The γ -phase is with respect to catalytic support, the most important [2]. Structurally it has not been determined completely, but is most likely isostructural to MgAl_2O_4 , where the oxygen anions constitute a cubic spinel structure (basically a FCC oxygen sub-lattice), with 32 anions in the unit cell and 24 cation vacancies. Only 21 1/3 cations are available in stoichiometric Al_2O_3 , and the Al-cations are distributed

among the 24 vacancies of both octahedral and tetrahedral coordination. The details of the cation distribution is still under debate in the literature [49,51]. γ -Al₂O₃ is formed by heating boehmite to 450 °C in air, or by heating gibbsite in vacuum [7, 49]. The γ -phase contains some water in contrast to the α -phase, which is almost completely free of water [7]. Single crystals or geometrically well-defined surface terminations have not been prepared from bulk γ -Al₂O₃ [2]. The surface of γ -Al₂O₃ is under normal conditions rich in hydroxyl groups [7, 49]. The θ -phase of alumina is the final dehydration product of gibbsite when heated in vacuum. The structure is virtually the same as that of γ -Al₂O₃ with respect to bond length and bond angles. The crystal structure differs only in different occupation probabilities of the tetrahedral and octahedral vacancies [50].

It is interesting that even though the bulk structure of many metal oxides is well known from x-ray crystallography, the surface structure is often unknown [2]. This is partly an experimental problem related to difficulties in preparing clean compositionally and structurally well-defined surfaces. Many metal oxides are thermally and electrically insulating compound materials and therefore the renowned cleaning technique of sputtering and annealing may be difficult or impossible. Sputtering may suffer from preferential sputtering yields of the constituents as well as charging of the sample. Annealing can be problematic due to different segregation rates of the constituents, and electron beam bombardment may be inhibited by charging. A clean surface can be obtained by a cleavage of the crystal. To avoid contamination this can be done in UHV. It is, however, not possible to cleave along all crystallographic orientations, and the cleaving may lead to point defects, which are not readily removed by e.g. annealing.

One way of getting around the experimental problems with bulk oxides, and still be able to obtain significant insight into the surface properties, is to use thin oxide films grown on a suitable substrate as model systems [4–6]. The thin films furthermore have the advantage that one can prepare well-defined surfaces of phases which are not available from bulk samples. For example, thin films of α -, γ - and θ -Al₂O₃, have been reported grown on various faces of nickel-aluminum alloys [6]. If an insulating thin film is grown on a metal (or conducting) support, it may even be possible to use experimental techniques such as STM, which normally requires a conducting support. This is, however, only possible if the film is sufficiently thin to allow electron tunneling through the film.

A major concern with thin films as model systems, is the resemblance of

the thin film to the bulk counterpart. The thin film will in many cases deviate from bulk samples, and the game is to find or develop a system which mimic the property under examination.

3.2 Al₂O₃ films

The thin aluminum oxide film on NiAl(110) is just one among many thin aluminum oxide films supported on metal substrates.

Thin oxide films supported on a metal substrate are normally prepared in three ways. (i) They can be grown by oxidation of the native metal. (ii) They can be grown epitaxially on an inert metal substrate, and (iii) they can be grown by oxidation of an alloy [3]. Al₂O₃ thin films can be prepared in all three ways. If an aluminum surface is oxidized only an amorphous Al₂O₃ film can be created. This is due to the fact that the temperature needed to order the oxide film is higher than the melting point of aluminum [52]. By using refractory metal surfaces as substrates, various thin films can be grown either by deposition of Al and subsequent oxidation at elevated temperatures, or by depositing Al in an oxygen ambient onto the sample at elevated temperatures [6,53]. For alloy oxidation, NiAl and Ni₃Al are specially well-suited, and Al₂O₃ films have been prepared on all the low index faces of both NiAl and Ni₃Al [6]. At present, the Al₂O₃ films which exhibit the largest degree of uniformity as well as long and local range order, are the films grown by oxidation of NiAl(110) [54] and Ni₃Al(111) [55,56].

3.3 Preparation of the Al₂O₃/NiAl(110) film

An Al₂O₃ film is prepared by a recipe developed in the Freund group [57,58]. First, the NiAl-crystal is cleaned as described in section 2.2. After the last annealing cycle the crystal is kept at 300 °C, and the oxide is then formed by using one of two methods: either by backfilling the chamber via a leak valve to 6×10^{-6} torr of oxygen for 15 minutes, or by exposing the surface to a local fluence of oxygen from a gas doser. After the oxidation the crystal is finally annealed at 850 to 900 °C for 3 to 5 minutes. The oxygen used was 99.999% pure. The gas doser [59,60] consists of a small reservoir (~200 ml), which is initially filled with 10 to 25 mbar of oxygen. The reservoir is connected via a pin-hole (d a few μm) to a long Cu tube with an inner diameter of 5 mm. The Cu tube is positioned at less than 1 mm above the sample during the oxidation.

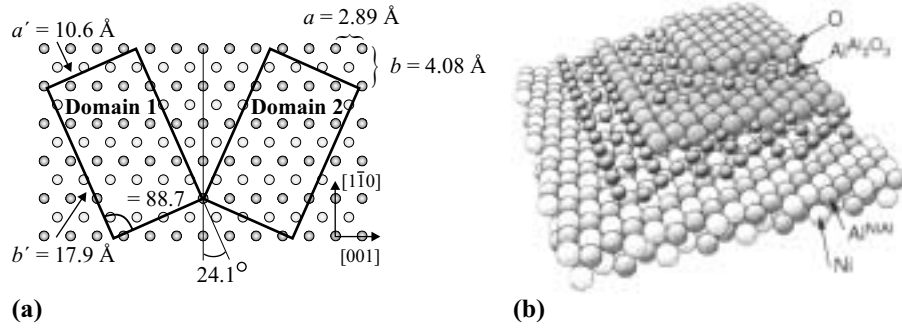


Figure 3.1: (a) Unit cell of the two reflection domains with respect to the NiAl(110) lattice, adapted from [57]. (b) Freund model of the oxide film, adapted from [52].

The local flux was normally chosen to be ~ 1 L/sec. The oxide film does not seem highly sensitive to the design details of the gas doser or the details of the preparation procedure. The most important factor seems to be the total exposure. If an oxygen dose less than ~ 100 L is used, the film is extremely rough and no areas with a well-developed structure are found. If the surface is exposed to a dose between ~ 100 L and ~ 1000 L, the film formed will have holes in it. To prepare a well ordered film which covers the entire surface, more than ~ 1000 L of oxygen should be used.

The advantage of the gas doser over backfilling of the chamber is that the total chamber pressure can be kept below 5×10^{-9} torr during oxidation which improves the subsequent vacuum conditions.

The scenario of the oxidation/annealing procedure is as follows: During oxidation the oxygen reacts with NiAl in the upper layers to produce an amorphous Al_2O_3 film and release Ni. During the final annealing the surplus Ni dissolves in the bulk, while the Al_2O_3 film crystallizes. No metallic Ni or any trace of NiO are detectable in ultraviolet photoelectron spectroscopy after this procedure, whereas the presence of Al^{3+} as in Al_2O_3 has been detected with Auger electron spectroscopy [57, 61].

3.4 Structure model of Al₂O₃/NiAl(110)

The oxide unit cell was determined by LEED [54,57] and found to be

$$a = 10.6 \text{ \AA}, \quad b = 17.9 \text{ \AA}$$

The film grows in two orientationally related domains on the substrate. The two domains are reflected through the $[1\bar{1}0]$ direction of the underlying substrate and rotated $\pm 24.1^\circ$ relative to the underlying NiAl(110) surface mesh. These domains are referred to as reflection domains. Figure 3.1(a) is a sketch of the oxide unit cell with respect to the NiAl(110) unit mesh.

The detailed atomic arrangement of the Al₂O₃ film has not yet been established, but many aspects of the film structure have been charted using a lot of the tools available in surface science. The experiments have mainly been conducted by, or in joint collaborations with, the group of H.-J. Freund. The Freund model of the film is shown in Fig. 3.1(b). The model is a (111) termination of γ -Al₂O₃. [25,54,57].

The growth of the Al₂O₃ film is self-limited and covers the entire surface. The film is oxygen-terminated with the oxygen-ions in a slightly distorted hexagonal arrangement. It is 5 Å thick, corresponding to two sandwich layers of Al-O, and the coordination of the Al-ions is a mix of both tetrahedral and octahedral coordination [62]. The film is proposed to resemble the γ -phase of Al₂O₃, as the EELS-spectrum of the film most resemble that of γ -Al₂O₃. One should, however, notice that, first of all, an important aspect of the γ -phase, the incorporation of water and hydroxyl groups, is not fulfilled by the film, and secondly the film is too thin to occupy the entire unit cell of γ -Al₂O₃ (it is even too thin to distinguish between FCC and HCP stacking of the O²⁻ lattice, which is an important difference between the α - and γ -phases).

Recently, Jennison and Bogicevic [63,64] have performed DFT calculations of thin Al₂O₃ films on the Al(111) and Ru(0001) surfaces to elucidate the structure of the film, and to provide a model system for which metal growth can be studied theoretically. The model, which has emerged from their calculations differs substantially from the Freund model. It consists of a chemisorbed oxygen layer on top of which a nearly co-planar layer of Al and O is situated. The Jennison and Bogicevic film does not mimic the Al₂O₃/NiAl(110) with respect to adhesion of Pd, which may be due to a structural difference between the calculated film on Al(111) and Ru(0001) and the film on NiAl(110) [64]. We return to the Jennison and Bogicevic calculations when metal adhesion is

discussed in chapter 4, as it was our data that lead Jennison and Bogicevic [64] to reconsider the resemblance between their film and the NiAl(110) film.

3.5 Appearance of the film when imaged by STM

The appearance of the oxide film when imaged by STM is not understood in detail, and especially the dramatic bias dependence is intriguing. The bias dependence was described by Libuda *et al.* [54], Stempel [65], and Bäumer and Freund [25]. In the following a detailed description of the film will be given. The aim is to provide a basis for the interconnection between the film structure and the growth of palladium.

The film possesses a band gap of ~ 6.7 eV [66], but due to the limited thickness of the film, it is possible to obtain stable tunneling conditions for bias voltages in the entire range from a few mV up to around 10 V at both positive and negative bias voltage. Two different tunneling regimes can be defined: tunneling in the film gap, such that film states do not contribute to the tunnel current, and tunneling outside the gap where the film states contribute to the tunnel current. The following describes these two situations for positive and negative bias voltage.

3.5.1 Positive bias voltage

The most prominent feature of the film when imaged with the STM is the appearance of domain boundaries. Two types of domain boundaries exist: reflection domain boundaries and antiphase domain boundaries [54]. The reflection domain boundaries are boundaries between the two domain orientations, whereas the antiphase domain boundaries are boundaries between areas which are only shifted laterally. The detailed nature of the antiphase domain boundaries is unknown, but it is assumed that they are caused by strain between the oxide and the substrate occurring during the growth process [25].

At positive bias voltages above 1 V the domain boundaries clearly protrude outwards from the surface. The appearance of the oxide areas in between the antiphase domain boundaries depends partly on the detailed tip character, but mainly in one of two ways. The first type of appearance is illustrated in Fig. 3.2(a) with an image acquired at $U_s = 4.2$ V. At this bias the oxide film exhibits a clear line structure with pairs of lines running along the close-packed direction of the oxide unit mesh, i.e. parallel to the antiphase domain

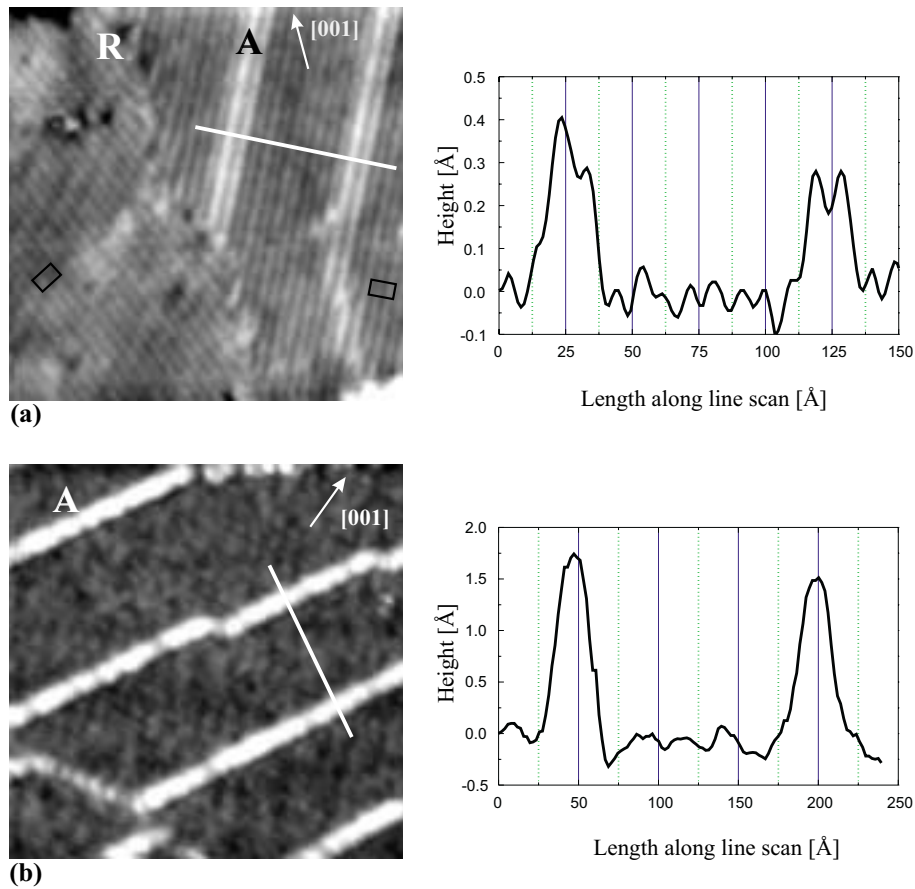


Figure 3.2: Examples of the film appearance when imaged with positive bias voltage. Reflection domain boundary (R) and antiphase domain boundaries (A) are indicated. Line scans are along the indicated lines. Rectangles indicate oxide unit cell. (a) $300 \times 300 \text{ \AA}^2$, $U_s = 4.2 \text{ V}$, $I_t = 1.0 \text{ nA}$. (b) $500 \times 500 \text{ \AA}^2$, $U_s = 2.5 \text{ V}$, $I_t = 0.7 \text{ nA}$.

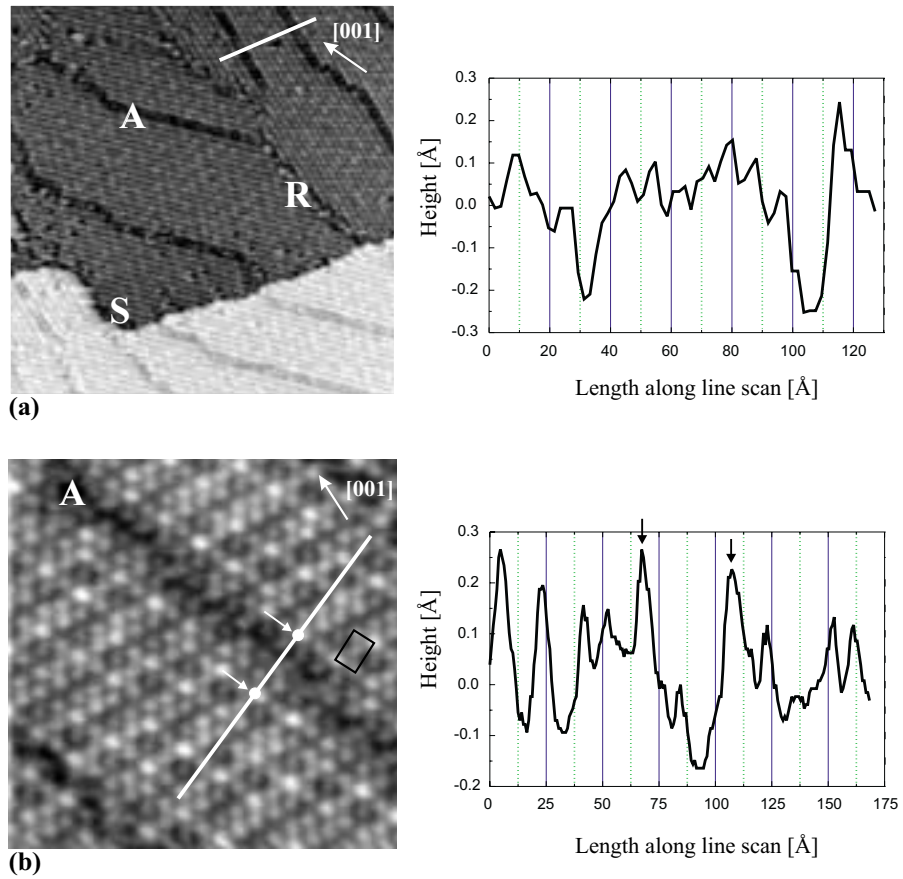


Figure 3.3: Examples of the film appearance when imaged with negative bias voltage. Step edge (S), reflection domain boundary (R) and antiphase domain boundaries (A) are indicated. Line scans are along the indicated lines. Rectangle indicates oxide unit cell. (a) $500 \times 500 \text{ \AA}^2$, $U_s = -1.3 \text{ V}$, $I_t = -0.4 \text{ nA}$. (b) $200 \times 200 \text{ \AA}^2$, $U_s = -2.5 \text{ V}$, $I_t = -0.8 \text{ nA}$.

boundaries. In this case the antiphase domain boundaries are observed as protruding double lines. The distance between the pair of lines is $\sim 18 \text{ \AA}$, and thereby directly reflects the structure of the oxide mesh. The second type of appearance is illustrated in Fig. 3.2(b) with an image acquired at $U_s = 2.5 \text{ V}$, here the areas between the antiphase domain boundaries appear gritty, and the antiphase domain boundaries are not resolved in two stripes. The width is, however, still $\sim 18 \text{ \AA}$.

The apparent height of the domain boundaries depends foremost upon the details of the tip, but trends exist. Usually the domain boundaries are observed to increase in height with increasing bias in the bias range between ~ 1 and $\sim 3 \text{ V}$. They are most prominent with $U_s \approx 2.5$ to 3 V , and above $\sim 3 \text{ V}$ the height slowly decreases with increasing bias voltage. With a bias voltage below $\sim 2.5 \text{ V}$ or above $\sim 3 \text{ V}$, the apparent height is generally below 1 \AA , whereas with a bias voltage between 2.5 and 3 V , the apparent height may be as high as 2.5 \AA , but it is normally between 1 and 1.5 \AA .

3.5.2 Negative bias voltage

At negative bias voltages the appearance of the film, with respect to the domain boundaries, is complementary to that at positive bias voltage above $\sim 1 \text{ V}$, as the domain boundaries here appear as depressions. At a bias voltage around -1 V , the area between the domain boundaries appears like in the case of Fig. 3.2(a) with a striped structure running along the close-packed direction of the oxide unit mesh. This is shown in Fig. 3.3(a). If the bias voltage is around -2 V the stripe structure is resolved into blobs, as shown in Fig. 3.3(b). The distribution of the protrusions clearly reflects the unit mesh of the film, but the individual blobs exhibit large and random intensity variations. The depth of the domain boundaries is not well determined as the corrugation of the oxide domain exceeds the depth of the domain boundaries. The depth seems not to be correlated with the bias voltage, and is normally around 0.5 \AA .

3.5.3 Interface

Finally, another type of image can be obtained in a large bias interval, and is more dependent on the detail of the tip character than on the bias voltage applied. In this imaging mode atomic resolution can indeed be obtained, the resolution is, however, not related to the surface structure of the oxide film, but rather to an interface layer between the NiAl substrate and the oxide

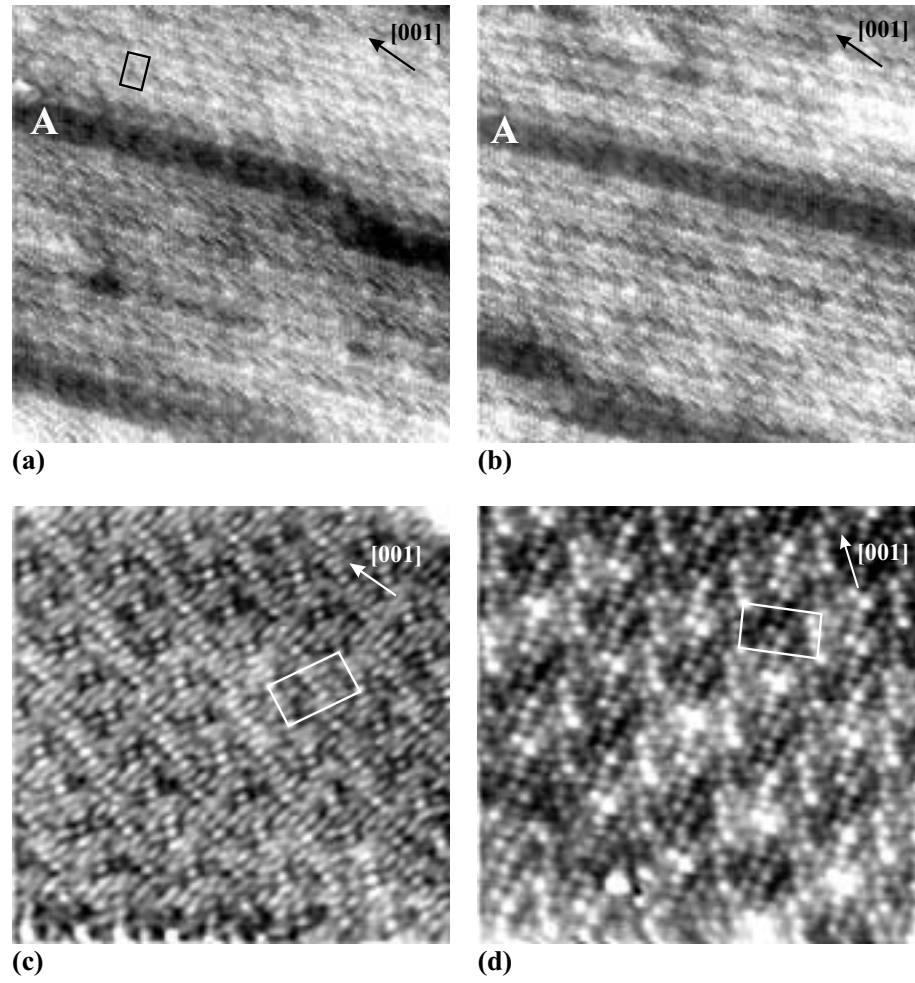


Figure 3.4: Atomic resolution images of the NiAl-interface, an antiphase domain boundary (A) is indicated. Rectangles indicate oxide unit cell. (a) $200 \times 200 \text{ \AA}^2$, $U_s = 33 \text{ mV}$, $I_t = 1.1 \text{ nA}$. (b) $200 \times 200 \text{ \AA}^2$, $U_s = -23 \text{ mV}$, $I_t = -1.2 \text{ nA}$. (c) $100 \times 100 \text{ \AA}^2$, $U_s = 1.1 \text{ V}$, $I_t = 1.2 \text{ nA}$. (d) $100 \times 100 \text{ \AA}^2$, $U_s = -2.1 \text{ V}$, $I_t = -1.0 \text{ nA}$.

film [54]. Examples of such images are shown in Fig. 3.4, where (a) and (b) were obtained with a bias voltage in the millivolt regime, whereas (c) was obtained at +1.1 V, and (d) at a negative bias voltage of -2.1 V. The images were obtained at bias voltages in the electronic gap of the film. A detailed model accounting for the positions of the protrusions on the domains has been put forth by Libuda *et al.* [54]. Libuda *et al.* proposed that the protrusions are related to Al atoms that have been displaced in order to compensate for the incommensurability between the Al_2O_3 unit cell and the NiAl(110) lattice, i.e., the bright protrusions in the images in Fig. 3.4 reflect the positions of the Al atoms at the interface. A recent theoretical work by Lozovoi *et al.* [67] proposes that an interface layer which solely contains Al is formed when oxygen is adsorbed on NiAl(110).

Figure 3.4(a) was obtained with positive bias voltage, whereas Fig. 3.4(b) was obtained at negative bias voltage. In this imaging mode the antiphase domain boundaries are depicted as depressions irrespectively of the polarization of the bias. Atomic force microscopy measurements have shown that the surface of the antiphase domain boundaries is depressed with respect to the film surface [25, 65]. The antiphase domain boundaries are observed as depressions in the interface, which strongly suggests that also the interface lies deeper in the domain boundary regions. It can, however, not be excluded that an electronic effect originating from a different electron transfer in the boundary regions and in the non-boundary regions is responsible for the effect. Protrusions can be imaged in the boundary region with an arrangement similar, but not identical, to that outside.

3.6 Defect structure

When the film is imaged at large scale, a fairly regular network of antiphase domain boundaries can be observed, as illustrated in Fig. 3.5. On the image in Fig. 3.5(a) the three line defects present on the film are readily recognized as: Step edges (S), which are the result of atomic steps in the underlying NiAl(110) substrate; reflection domain boundaries (R), which separate the two domain orientations of the oxide film, and the antiphase domain boundaries (A). Besides line defects, point defects are also present on the oxide domains. These are, however, not readily observable with the STM [25, 68]. Film of the type shown in Fig. 3.5(a) is what will be referred to as a high quality film, i.e., films where the antiphase domain boundaries mainly run along the

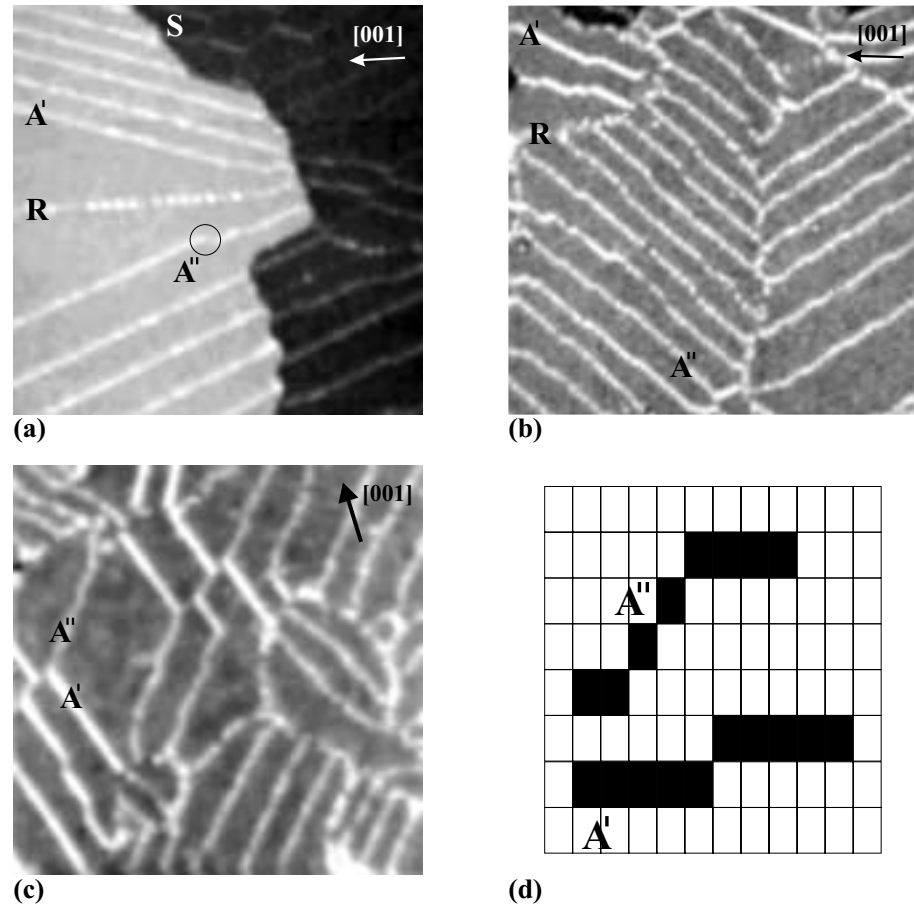


Figure 3.5: Defect structure of the film, see text for details. (a) $1500 \times 1500 \text{ \AA}^2$, $U_s = 1.1 \text{ V}$, $I_t = 0.8 \text{ nA}$. (b) $1000 \times 1000 \text{ \AA}^2$, $U_s = 3.5 \text{ V}$, $I_t = 1.0 \text{ nA}$. (c) $1000 \times 1000 \text{ \AA}^2$, $U_s = 5.0 \text{ V}$, $I_t = 0.5 \text{ nA}$. (d) Course of the antiphase domain boundaries.

close-packed direction of the oxide unit mesh (boundary type A'), and with few domain boundary segments that break off from that direction (boundary type A''). On some films domain boundary of the A'' type are favored over the A' type. A such film is shown in Figs. 3.5(b) and (c). These films are referred to as low quality film. The film area shown in Fig. 3.5(b) is atypical as the A'' network is very regular. Films with many domain boundary segments of the A'' type usually possess a more random domain boundary network, as in Fig. 3.5(c). Apart from the nature of the domain boundary network it is not possible to detect any significant differences between the different types of film with the STM, neither with respect to the structure nor with respect to the bias dependence. The reason why the domain network appears ordered or unordered is unclear. One important factor is the way the film was prepared. For instance, films with such a nice defect network as that in Fig. 3.5(a) have never been obtained when the film is prepared by backfilling the chamber, whereas such films are routinely obtained if the film is prepared with a gas doser. A possible explanation could be that by dosing with the gas doser a much cleaner oxidation is attained. No significant impurities, however, can be detected with AES on films of lower quality.

3.7 Apparent film height

As pointed out by Bertrams *et al.* [69], an oxide film containing holes can be grown, i.e. the film covers most of the surface, but at some places a small patch of the NiAl underneath is exposed, as seen in Fig. 3.6(a). The creation of such holes can be accomplished simply by exposing the crystal to an "insufficient" amount of oxygen during the oxidation step in the preparation procedure.

The transition from fully developed film to metal hole is abrupt, and only at the very rim can a change in the oxide film be detected in the STM images. When scanning across the surface from the hole to the film, the STM tip moves from clean metal to oxide, and the influence of the oxide's electronic structure on the tunneling current can thus be probed. Bertrams *et al.* noted that when scanning across a film edge, it was only for high bias voltages that an increase in the apparent height could be detected [69].

We have made a systematic study of how the apparent height of the film depends upon the tunnel parameters, by scanning along a predefined line (such as the arrow in Fig. 3.6(a)) at preset values of the tunnel parameters. While the magnitude of the tunnel current has little influence, a drastic dependence

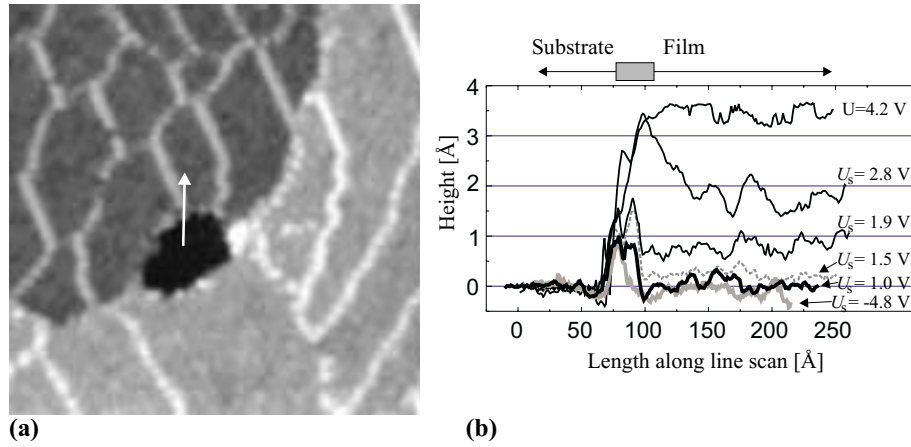


Figure 3.6: (a) STM image of the Al_2O_3 film with a hole. $700 \times 700 \text{ \AA}^2$, $U_s = 2.8 \text{ V}$, $I_t = 0.6 \text{ nA}$. (b) Line scans at different bias voltages across the edge of the hole. All scans have been acquired with $I_t = 0.6 \text{ nA}$.

on bias voltage is observed. The measurements are summarized in Fig. 3.6(b), which displays the height profiles across the metal hole and the oxide film at different bias voltages. One should focus only upon the mean height level of the oxide, rather than the height variations at the oxide edge, as the observed height at the edge depends strongly upon the exact position of the line scan. It is seen that when scanning at a negative bias voltage of -4.8 V , the film is imaged at the same level as the substrate. This applies for all negative bias voltages down to -10 V . On the other hand, if the scan across the hole is performed with positive bias voltages, a clear height variation is observed. From a few mV and up to $\sim 1.3 \text{ V}$ no or little height difference between the metal and the film is found, but from $\sim 1.3 \text{ V}$ and up to $\sim 4 \text{ V}$ the apparent height of the film gradually increases until a height difference of 3.5 \AA is observed. No further increase in height can be attained by raising the bias up to $+10 \text{ V}$. The height scale is calibrated with respect to the step height on the clean NiAl(110) surface.

In order to rationalize the above measurements, the tunneling current is split into the contribution from the substrate, and the contribution from the film. One could also include a contribution from the interface; this is, however,

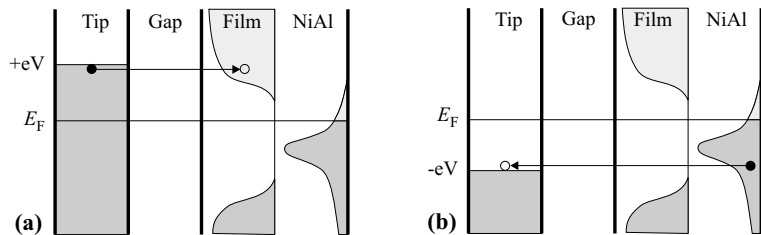


Figure 3.7: Schematic drawing of the tunneling situation at (a) positive and (b) negative bias voltage. E_F denotes the Fermi energy before bias is applied.

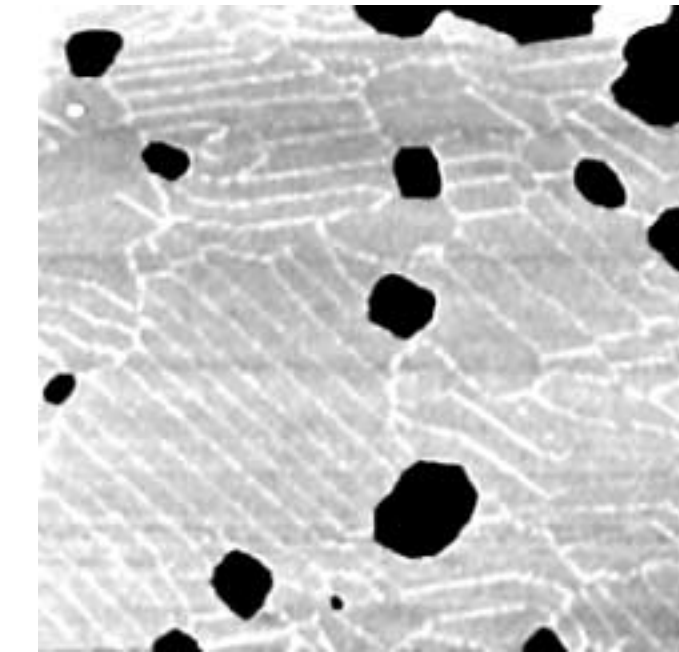
not expedient for the present discussion:

$$I \propto \int_0^{eV} [\rho_s(E_F - eV + \epsilon) |M|^2 + \rho_{\text{ox}}(E_F - eV + \epsilon) |M'|^2] \rho_t(E_F + \epsilon) d\epsilon \quad (3.1)$$

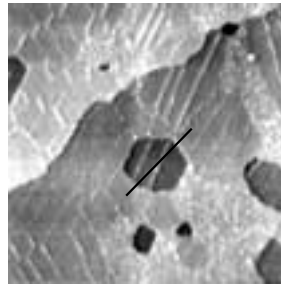
where ρ_s , ρ_{ox} and ρ_t are the density of states (DOS) of the sample, the oxide film and the tip, respectively, and $|M|^2$, $|M'|^2$ tunneling matrix elements.

The electronic band gap of the supported film has recently been characterized by Andersson *et al.* with x-ray absorption spectroscopy and photoelectron spectroscopy [66]. The gap was found to be asymmetric, ranging from -4.5 eV below to 2.2 eV above E_F with a continuum of defect states extending from the conduction band edge (and presumably the valence band edge) to E_F . Neglecting for a moment the presence of any defect states, one would expect that for bias voltages inside the band gap the film would be imaged at the same height as the metal, since the tunnel current would be drawn exclusively from the metal. For bias voltages outside the gap, current could be drawn from the film, the tip would retract and the film would be imaged higher than the metal. This is not what is observed.

At positive bias voltages below ~ 1.3 V, the oxide and the substrate are imaged at the same height, whereas the oxide height increases at increasing bias voltage. This is consistent with the presence of an electronic band gap where ρ_{ox} is negligible in the gap, i.e. at low bias, but non-zero above the gap, i.e. at high bias. The onset of tunneling to film starts at ~ 1.3 V rather than 2.2 V, this could be due to the defect states mentioned above and to the tail of conduction band states below the strongly sloping part of the alumina conduction band DOS.



(a)



(b)

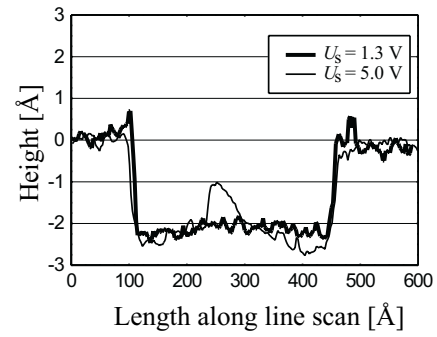


Figure 3.8: STM images of an Al_2O_3 film with vacancy islands. (a) $2000 \times 2000 \text{ \AA}^2$, $U_s = 2.5 \text{ V}$, $I_t = 1.3 \text{ nA}$. (b) STM image: $1500 \times 1500 \text{ \AA}^2$, $U_s = 2.5 \text{ V}$, $I_t = 0.7 \text{ nA}$. Line scans along the indicated line of a vacancy island, both line scans have been acquired with $I_t = 0.9 \text{ nA}$.

For negative bias voltages, one would expect a dramatic change in the film height around the lower band gap edge, i.e. around -4.5 V. This is, however, not observed. It is proposed that the reason for this should be found in the DOS of the substrate. As shown schematically in Fig. 3.7, the NiAl DOS is dominated by the Ni $3d$ states which form a strong band with its center ~ 2 eV below E_F , i.e. central in the band gap below E_F and with a very weak density above E_F [40, 66]. At negative bias voltage, where the tunneling takes place from occupied surface states into unoccupied tip states, the tunnel current is totally dominated by the Ni $3d$ states (relative to occupied film states). The reference level is therefore fixed at the interface for all negative bias voltages.

3.8 Vacancy islands

Apart from the holes in the film like that of Fig. 3.6(a), vacancy islands in the underlying NiAl substrate often appear on both complete and incomplete films, as shown in Fig. 3.8. The presence of vacancy islands is not observed on the clean NiAl(110) surface, and must therefore be induced in the oxidation process, probably related to the segregation of Al towards the surface.

Vacancy islands can be distinguished from holes on the basis of bias dependent imaging. A high positive bias may reveal that the hole actually contains an oxide film as the domain boundaries become visible, see Fig. 3.8(b). However, not all oxidized vacancy islands contain domain boundaries. As expected, line profiles across the hole reveal that the height profile does not depend upon the bias voltage for vacancy islands. This is illustrated by the line scans in Fig. 3.8(b). The only difference between the two scans is that at high bias the domain boundary is protruding, no height difference is observed.

3.9 Defect structure of an incomplete film

The general appearance of the film becomes heavily influenced by the reduction in oxygen exposure, as shown in Fig. 3.9(a). Apart from the holes and areas displaying the normal network of line defects, a large fraction of the surface is covered by a phase where the defect structure is completely random. The random line defects have the same bias dependence as those of the fully developed film, i.e. the line defects protrude only at positive bias, and are imaged as depressions at negative bias. An example is given in Figs. 3.9(c) and (d), where the same area was scanned with negative bias voltage in (c) and positive bias voltage in (d).

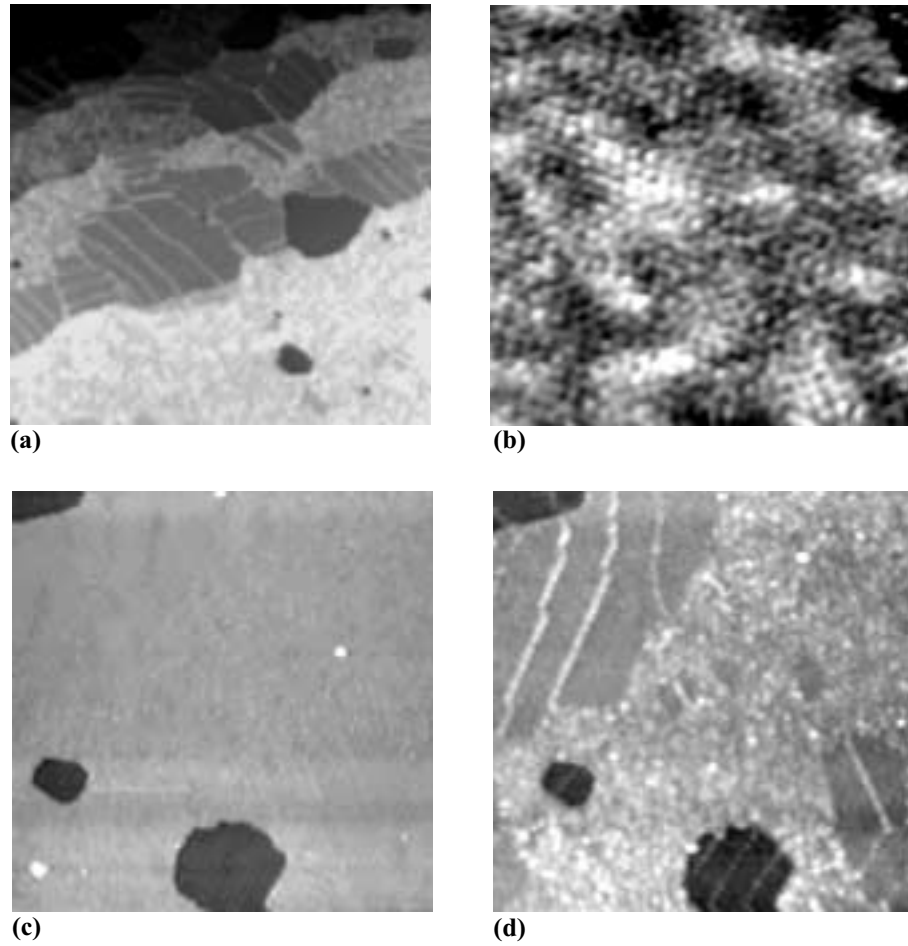


Figure 3.9: STM images of an incompletely oxidized Al_2O_3 film (a) Overview image showing domains with ordered and unordered defect structure. $2000 \times 2000 \text{ \AA}^2$, $U_s = 2.5 \text{ V}$, $I_t = 0.7 \text{ nA}$. (b) STM image of the NiAl-interface in a region with unordered defect structure. $70 \times 70 \text{ \AA}^2$, $U_s = -188 \text{ mV}$, $I_t = -1.6 \text{ nA}$. (c) and (d) STM images of the same area with different bias polarity. $1000 \times 1000 \text{ \AA}^2$, $U_s = \pm 2.5 \text{ V}$, $I_t = \pm 0.6 \text{ nA}$.

As already mentioned, the interface layer can be imaged by applying proper tunnel conditions. Such an interface STM image is presented in Fig. 3.9(b), which is recorded in a region with random defect structure. While the interface structure of the fully developed film is well ordered (see Fig. 3.4), no local or long range order is visible in the interface structure of the unordered film. Since the bias dependence of both domain boundaries and interface layer corresponds exactly to that of the fully developed film, we speculate that the defect filled areas are still Al_2O_3 .

A possible explanation why the unordered film areas appear at insufficient oxygen dosage, is related to the formation of the interface layer itself. As shown by Lozovoi *et al.* a very likely precursor of the Al_2O_3 film formation is an interface layer consisting of pure Al [67]; thus Ni was excluded from at least the uppermost layer, whereas Al was added from the bulk. The formation of such an interface layer must be very sensitive to the oxygen dosage. The unordered film areas could be due to a lack of oxygen in the interface zone, such that a pure Al interface layer, soft enough to allow for the long-range ordering of the Al_2O_3 film, is not formed. Ni-Al compounds are much stiffer than pure Al, probably inhibiting the large-scale ordering of the line defect network.

3.10 Conclusion

The appearance of the film has been described in details. When imaged by the STM the film exhibits a large voltage dependence which was first characterized by Libuda *et al.* [54], a complex dependence which we have been able to confirm completely as well as contribute to, so that a more complete description is now available. The fact that two independent studies find the same complex bias dependence clearly shows that the appearance of the STM images reflects the substrate and not the details of the tip. This provides a unique possibility for making a theoretical structure determination by comparing STM simulations with the obtained STM images. Unfortunately, at present, the task is too much of a challenge for theorists due to the large unit cell of the film.

A systematic study of the relationship between the applied tunnel bias voltage and the apparent height of a thin aluminum oxide film has been carried out. It was shown that a clear bias dependence of the apparent height is observed only in the interval from +1 V to +4 V, where the apparent height increases by 3.5 Å. A simple model explaining the observed dependence has been presented.

Palladium nanocrystals on $\text{Al}_2\text{O}_3/\text{NiAl}(110)$

The metal-oxide interface is of extreme importance in many technological applications as already discussed in the introduction. Extensive investigations have been undertaken to improve the understanding of the physics and chemistry of the metal-oxide interface [14, 15, 25, 70]. In spite of these efforts, quantitative information on the metal-oxide interface, such as adhesion and interface energies, are, in general, unknown, and attempts to characterize metal clusters deposited on oxides at the atomic level have so far not been successful.

In this chapter different aspects related to Pd nanoclusters residing on $\text{Al}_2\text{O}_3/\text{NiAl}(110)$ are discussed. The first part is concerned with general aspects of the growth and structure of small clusters. Most important, the Wulff shape is introduced, which provides the foundation for discussing the shape and properties of the supported Pd nanoclusters. The second part is related to measurements on the Pd clusters. The discussion starts out by considering the growth behaviour. Focus is then turned towards structural aspects of the nanocrystals, ranging from detailed atomic-scale insight to a morphological description from which the adhesion energy of palladium on the Al_2O_3 film can be derived. Then some measurements of the Pd nanoclusters in a high-pressure H_2 ambient are discussed, and finally a brief overview of various metals which have been studied on the Al_2O_3 film is given.

The results presented in section 4.8 are from Ref. [III], those in sections 4.9 and 4.13 are from Ref. [I], and those in section 4.16 are from Ref. [IV].

4.1 Experimental details

First an oxide film was prepared as described in section 3.3. Palladium was then deposited on the film under UHV conditions ($p < 10^{-9}$ during deposition) at a constant rate. Most of the experiments were obtained with Pd deposited from a home-built source consisting of a palladium wire wound around a tungsten filament, which could be heated resistively. The deposition rate was in this

case: $R \approx 0.16$ ML/sec. A few of the experiments were obtained with Pd deposited from a commercial e-beam metal evaporator. The deposition rate was not calibrated in that case.

4.2 Nucleation and growth

When metal atoms impinge on a surface, they may either be accommodated by the surface or desorb. If the sticking probability is non-zero (the sticking probability of metal atoms on oxide surfaces is in many cases between 0.5 and 1 [14]), atoms accumulate on the surface. In the simplest picture, a stable nucleus is formed first, then the cluster grows larger. On an oxide surface a stable nucleus can be formed either by attachment to a special site, i.e. a defect, or by meeting other atoms forming a stable nucleus. If the nucleation is controlled by attachment to defects, the nucleation is called heterogeneous, and if not, the nucleation is called homogeneous.

Classically three different growth modes are distinguished: (i) Island growth (Volmer-Weber growth), where the deposited material accumulates in isolated 3D clusters (islands). (ii) Layer-by-layer growth (Frank-van der Merve growth), where one monolayer is completed before the next layer starts. (iii) Layer plus island growth (Stranski-Krastanov growth), where the system start out with layer-by-layer growth, but after a certain thickness changes and continues in island growth [71]. The Volmer-Weber growth mode is found in many cases of metal on oxide growth [14,15]. It is expected that the system grows according to Volmer-Weber mode, if the deposits are bound stronger to each other than to the substrate. Introducing the surface free energy, γ_i , as the energy cost per area of sustaining a surface, the Volmer-Weber and Frank-van der Merve growth modes can be distinguished as:

$$\begin{aligned} \gamma_{\text{sub}} < \gamma_{\text{dep}} + \gamma_{\text{int}} &\rightarrow \text{Volmer-Weber growth mode} \\ \gamma_{\text{sub}} > \gamma_{\text{dep}} + \gamma_{\text{int}} &\rightarrow \text{Frank-van der Merve growth mode} \end{aligned}$$

where γ_{int} is the interface energy. In the intermediate growth mode of Stranski-Krastanov, γ_{int} changes after the completion of the first (few) layer(s), such that subsequent layer growth becomes unfavorable and islands are formed on top of the layers. Surface free energies of metals are usually larger than those of oxides [15], which is the reason why most metal-on-oxide systems grow according to Volmer-Weber growth. It is, therefore, assumed that Pd grow according to Volmer-Weber mode.

These three growth behaviors, however, only describe ideal situations. In the case of metal-on-oxide growth, at least two other growth behaviors can be found. The deposit may be incorporated in or buried by the oxide substrate, as it has recently been observed for Pt nanocrystals on $\text{TiO}_2(110)$ [72]. The deposit may also react with the oxide substrate, e.g. forming an oxide or mixed oxide by reducing the surface. An example of this is V deposited on $\text{Al}_2\text{O}_3/\text{NiAl}(110)$ [73]. Both of these growth behaviors are usually referred to as “strong-metal support interactions” or just SMSI-growth. The formation of a mixed oxide by reducing the substrate oxide is expected to occur if the enthalpy of formation for the new oxide is more negative than that for the substrate oxide, i.e. the system gains energy from the reduction [15].

4.3 Crystal shape

In the following only the Volmer-Weber growth is considered, and focus is on the shape of the individual clusters. A given cluster possesses either a growth shape, i.e. the actual shape which is determined by the growth kinetics, or an equilibrium shape, i.e. the thermodynamically most stable shape. The growth shape can be any shape, whereas the equilibrium shape is unique. In this section the equilibrium shape will be defined and discussed.

If the chemical potential of the bulk phase is higher than the chemical potential of the gas phase, then by forming a small crystal consisting of N atoms, the system gains: $N(\mu_{\text{gas}} - \mu_{\text{bulk}})$ in free energy. The condensation is, however, accompanied by an energy cost of forming a surface: $\gamma A_{\text{exposed}}$. By keeping the volume (and number of atoms) constant, the crystal shape which costs the least energy, can be obtained by minimizing the surface free energy:

$$\delta \int_S \gamma dA = 0 \quad (4.1)$$

The shape which fulfills this condition is the thermodynamically most stable cluster shape – the equilibrium shape or Wulff shape.

In the simple case where the surface free energy is isotropic, the shape of a free crystal is a sphere, and if the metal is deposited on a non-deformable substrate, the crystal will adapt the shape of a truncated sphere [74]. In the general case where the surface free energy is non-isotropic, the determination of the equilibrium crystal shape is somewhat more complicated. The problem of finding the equilibrium shape, given the surface free energies, can be solved

graphically, this is the so-called Wulff construction. The Wulff construction relies on the analytical solution to Eq. (4.1), the Wulff theorem.

The problem of finding the equilibrium shape was first addressed by Gibbs in 1878 and Curie in 1885 [74, 75], which is why the Wulff theorem is often referred to as the Gibbs-Curie-Wulff, or Gibbs-Wulff theorem. Wulff got his name on the theorem, as he in 1901 was the first to solve the problem [76]. Although Wulff solved the problem correctly, his proof was wrong [75]. By assuming that the solution was a polyhedron, a correct proof was given already in 1903 by Hilton. However, it was not ensured that the Wulff construction actually gave an absolute minimum of Eq. (4.1), only a relative minimum was ensured. In 1944 Dinghas proved that the Wulff construction indeed gives the absolute minimum, but still, only in the case where a polyhedral shape is assumed. Finally, in 1953 Herring [75] showed that the Wulff polyhedron is the absolute minimum by generalizing Dinghas' proof. The Wulff construction and the Wulff theorem only apply for a free crystal. If the crystal is placed on a substrate, the equilibrium shape changes. The Wulff construction and Wulff theorem for a crystal on a substrate were first derived in the early fifties by Kaichew, and later independently by Winterbottom in 1967 [77].

4.3.1 Wulff construction

The Wulff construction solves Eq. (4.1) graphically, i.e. it finds the shape that minimizes the total free energy keeping the cluster volume constant.

The starting point for constructing the equilibrium shape, is the surface free energy as a function of orientation. Then the equilibrium shape can be constructed as follows:

- The surface free energy, $\gamma(\theta, \phi)$, is plotted in all directions in a polar plot so that the radius equals the surface energy. This is called the γ -plot. An example is given in Fig. 4.1 for a hypothetical situation. The center of the γ -plot is called the Wulff point.
- At the end of each radius vector the tangent plane of the vector is placed.
- The equilibrium shape is obtained as the inner envelope of all the tangent planes. The symmetry of each plane/facet is the one which characterizes $\gamma(\theta, \phi)$, i.e. if (θ, ϕ) corresponds to e.g. the [100] direction, the facet is a (100) facet.

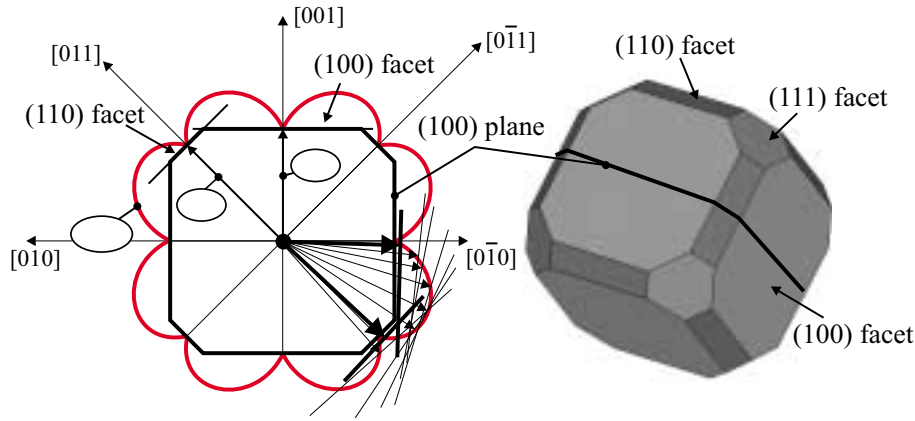


Figure 4.1: The Wulff construction scheme. The γ -plot is shown for a (100) plane on a Wulff shape obtained by use of a hypothetical set of surface free energies.

It is actually not necessary to know the exact course of $\gamma(\theta, \phi)$. Consider a plane with a normal vector, \hat{n} , pointing in a low Miller index direction, and another plane with a normal vector pointing in a slightly different direction, $\hat{n} + \delta\hat{n}$. Then the two planes are similar, except that the second plane contains steps. The surface free energy of the plane which contains steps is for small angles between \hat{n} and $\hat{n} + \delta\hat{n}$ given by [44]:

$$\gamma(\hat{n} + \delta\hat{n}) = \gamma(\hat{n}) + \frac{U_{\text{step}}}{a}|\alpha|$$

where U_{step} is the step free energy, a is the step height and α the angle between \hat{n} and $\hat{n} + \delta\hat{n}$. As $\delta\hat{n}$ grows larger, more and more steps will be present, and the surface free energy increases. Since the first plane was a low Miller index plane, the difference: $\gamma(\hat{n}) - \gamma(\hat{n} + \delta\hat{n})$ will be positive for any direction of $\delta\hat{n}$, and the γ -plot will have a cusp around \hat{n} [75]. Thus, the exact course of the γ -function between two low index directions is not important for the construction of the equilibrium shape.

The above discussion of the γ -plot is only strictly true at zero Kelvin. As the temperature is raised entropic terms have to be considered [44, 78]. This alters the extent of the various facets, and may lead to the presence of high Miller index facet planes situated in the crossing between low Miller index facets.

4.3.2 Wulff theorem

The Wulff construction relies upon the Wulff theorem:

$$\gamma(\theta, \phi)/d(\theta, \phi) = \text{constant}$$

stating that the real space distance, d , between the center of the cluster (the Wulff point) and a cluster facet in the (θ, ϕ) direction, is proportional to the surface free energy, γ , in that (θ, ϕ) direction. In other words, the polyhedron that emerges from the Wulff construction is, except for a scale factor, identical to the real space shape of a cluster in equilibrium. The largest facets always correspond to the close-packed surfaces. In this case the Wulff theorem simplifies to:

$$\gamma_{hkl}/d_{hkl} = \text{constant} \quad (4.2)$$

where (hkl) are the Miller indices of a low index direction. In this thesis the constant is set to 1.

Following Markov [74], the Wulff theorem is now proved. The proof is limited to the case where the solution is assumed to be a polyhedron.

The goal is to solve Eq. (4.1). The crystal is assumed to be in equilibrium with its vapor phase. Under the conditions of constant temperature, volume and chemical potential, the Helmholtz free energy is given as [75]:

$$F = G - PV = \int_S \gamma dA \quad (4.3)$$

where G is the Gibbs free energy, P the pressure and V the volume. Thus, minimizing Eq. (4.1) is equivalent to minimizing the Helmholtz free energy [74, 75]:

$$dF = 0 \quad (4.4)$$

As the cluster volume and number of atoms are kept constant, only the surface free energy needs to be minimized. The total Gibbs free energy at constant chemical potential is thus:

$$G = \sum_i \gamma_i A_i \quad (4.5)$$

where i enumerates the facets, γ_i are the surface free energies of the various facets, and A_i the areas of the corresponding facets. The total volume is split

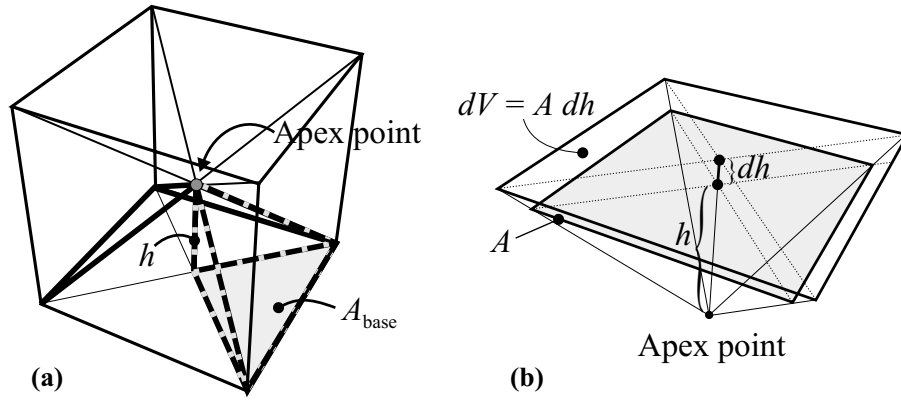


Figure 4.2: (a) Any polyhedron, here illustrated with a cube, can be split into “pyramids” with their base planes on the crystal facets and a common apex in an arbitrary point within the crystal. (b) Illustration of Eq. (4.9).

into the volume of the vapor and the volume of the crystal. The differential of the Helmholtz free energy now reads:

$$dF = -P_v dV_v - P_c dV_c + \sum_i \gamma_i dA_i = 0 \quad (4.6)$$

where P_c is the inner pressure of the crystal phase, P_v the pressure of the vapor phase, and V_v and V_c the volumes of the vapor and the crystal phases. Keeping the total volume: $V = V_v + V_c$ constant then $dV_v = -dV_c$, and Eq. (4.6) reduces to:

$$-(P_c - P_v)dV_c + \sum_i \gamma_i dA_i = 0 \quad (4.7)$$

As already mentioned, a polyhedral solution is assumed and all the facets are polygons. The volume of any polyhedron can be split into a sum of volumes of “pyramids” with their base plane on the crystal facets and a common apex in an arbitrary point within the crystal. This is illustrated in Fig. 4.2(a) with a cube. The volume of a pyramid with a polygonic base plane is fairly easily proven to be:

$$V_{\text{pyra}} = \frac{1}{3} h A_{\text{base}}$$

simply by splitting the pyramid into sub-pyramids with triangular bases, and showing that irrespective of the position of the apex point, the volume for a pyramid with a triangular base is given by $V_{\text{tri}} = \frac{1}{3}hA_{\text{tri}}$. The volume of the equilibrium shape is the sum of the volumes of the pyramids:

$$\begin{aligned} V_c &= \frac{1}{3} \sum_i h_i A_i \\ \Rightarrow dV_c &= \frac{1}{3} \sum_i (A_i dh_i + h_i dA_i) \end{aligned} \quad (4.8)$$

where h_i are the heights of the pyramids, and A_i the areas of the facet planes. An infinitesimal change of volume is to the first order equal to the area of the base plane times an infinitesimal height change, as illustrated in Fig. 4.2(b), such that $dV_i = A_i \times dh_i$ and the total differential volume element is:

$$dV_c = \sum_i A_i dh_i \quad (4.9)$$

Inserting Eq. (4.9) into Eq. (4.8) yields:

$$dV_c = \frac{1}{2} \sum_i h_i dA_i \quad (4.10)$$

Substituting Eq. (4.10) into Eq. (4.7) gives:

$$\sum_i \left(\gamma_i - \frac{1}{2}(P_c - P_v)h_i \right) dA_i = 0 \quad (4.11)$$

It is only the total volume which is kept constant, and dA_i are allowed to vary, thus each terms should equal zero:

$$\frac{\gamma_i}{h_i} = \frac{(P_c - P_v)}{2} = \text{constant} \quad (4.12)$$

This is the Wulff relation, stated in Eq. (4.2), since $(P_c - P_v)$ is independent of the crystallographic orientation.

The proof only ensures that the shape obtained is a relative minimum shape, not a global minimum shape. From a more general description of crystal forms it can be shown that Eq. (4.12) corresponds to a global minimum [75].

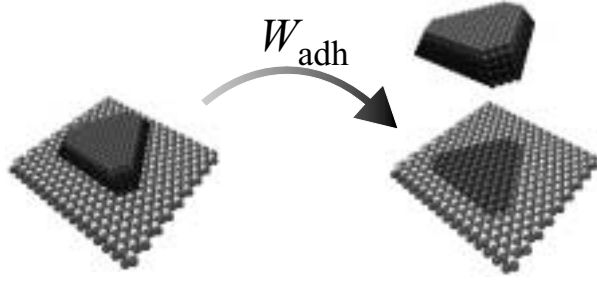


Figure 4.3: Graphical illustration of the adhesion energy.

4.3.3 Wulff theorem for a supported cluster

The Wulff theorem discussed above applies only to a free cluster. The present thesis, however, is concerned with crystals supported on a substrate. The interaction with the substrate surface alters the equilibrium shape.

By placing a crystal on a foreign substrate an interface boundary is created. The surface free energy of the interface is given by the Dupré equation [74]:

$$\gamma_{\text{int}} = \gamma_{\text{clu}} + \gamma_{\text{sub}} - W_{\text{adh}} \quad (4.13)$$

where γ_{int} is the energy of the interface per unit area, γ_{clu} the surface free energy of the contact facet of the cluster, γ_{sub} the surface free energy of the substrate and W_{adh} the adhesion energy. The adhesion energy is the work per unit area which is needed to separate the system into its constituents assuming no plastic or diffusional modifications. This is illustrated in Fig. 4.3. The adhesion energy is also called the work of adhesion.

When a crystal is formed on a substrate, the free energy relevant for the contact area is [74]:

$$\gamma^* = \gamma_{\text{int}} - \gamma_{\text{sub}} \quad (4.14)$$

which in terms of adhesion energy is:

$$\gamma^* = \gamma_{\text{clu}} - W_{\text{adh}} \quad (4.15)$$

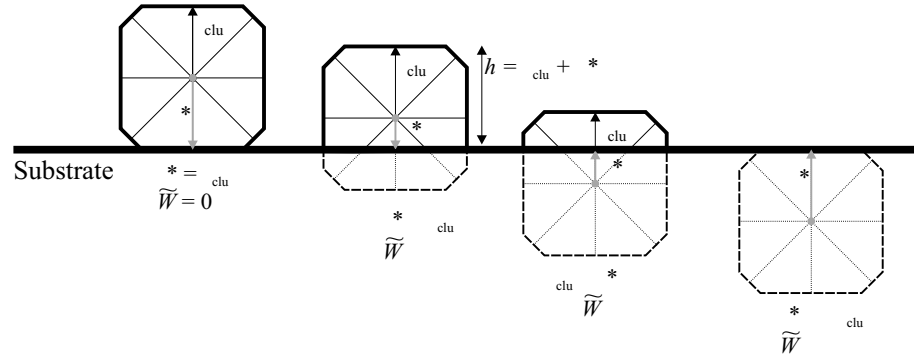


Figure 4.4: The relationship between the Wulff shape of a free and supported cluster. The solid line reflects the supported cluster shape, and the dashed line the free cluster shape.

The Helmholtz free energy of the system is now [74]:

$$F = -(P_v V_v + P_c V_c) + \left(\sum_{i \neq m} \gamma_i A_i \right) + \gamma^* A_m \quad (4.16)$$

where A_m is the area of the contact plane. Going through the same arguments as in section 4.3.2, one ends up with the Wulff theorem for supported clusters:

$$\frac{\gamma_i}{h_i} = \frac{\gamma^*}{h_m} = \text{constant} \quad (4.17)$$

Thus, determining the equilibrium shape of a supported particle is similar to determining the equilibrium shape of a free crystal, except that surface free energy in the direction of the interface is given by the effective surface free energy: γ^* . Graphically the supported equilibrium-shaped crystal can be found by first constructing the free equilibrium shape, and then lower this shape into the substrate until the protruding part has a height given by (see Fig. 4.4):

$$h = \gamma_{\text{clu}} + \gamma^* \quad (4.18)$$

The Wulff construction of a supported cluster leads to four different cases depending upon the magnitude of γ^* relative to γ_{clu} . This dependence is also

reflected in the relative adhesion energy:

$$\widetilde{W} = \frac{W_{\text{adh}}}{\gamma_{\text{clu}}} = 1 - \frac{\gamma^*}{\gamma_{\text{clu}}} = 1 - \widetilde{\gamma}^* \quad (4.19)$$

The four cases are shown in Fig. 4.4 which also illustrates the relationship between a free and supported cluster with respect to the Wulff construction:

- $\gamma^* = \gamma_{\text{clu}}$; $\widetilde{W} = 0$. The free cluster stands upright and unaffected on top of the substrate.
- $0 \leq \gamma^* < \gamma_{\text{clu}}$; $0 < \widetilde{W} \leq 1$. This corresponds to a lowering less than half of the free cluster into the substrate.
- $-\gamma_{\text{clu}} < \gamma^* < 0$; $1 < \widetilde{W} < 2$. More than half of the free cluster is lowered into the substrate.
- $\gamma^* \leq -\gamma_{\text{clu}}$; $\widetilde{W} > 2$. The entire cluster is lowered into the substrate. This situation is referred to as a wetting of the substrate.

The effective surface free energy can in contrast to an ordinary surface free energy be negative, meaning that in this case also h_m is negative.

4.4 Wulff construction for an FCC crystal

All facets, all lines, all edges and all points contained in the Wulff shape can be calculated from 3D geometry, using nothing but a sharp pencil, a large rubber and a lot of persistence. In this section a detailed example of how to calculate the width of the (111) facet is presented, and as all other relevant quantities can be calculated in a similar manner, their solutions are merely presented.

For very small clusters of FCC metals the more stable shape is the compact icosahedron [79,80]. In the icosahedral structure the central atoms are strongly compressed relative to bulk structure. At a given size, the strain energy, which increases with cluster size, is not compensated by the increase in cohesion and the FCC structure becomes more stable. The transition between icosahedron and the FCC structure already occurs around 50 atoms for Pd [81]. The nanocrystals presented in this thesis always contain more than 50 atoms, and only the shape of an FCC nanocrystal will be considered.

Figure 4.5 shows two Wulff shapes. Figure 4.5(a) shows a Wulff shape, which was obtained using the surface energies for Pd of the most recent calculations

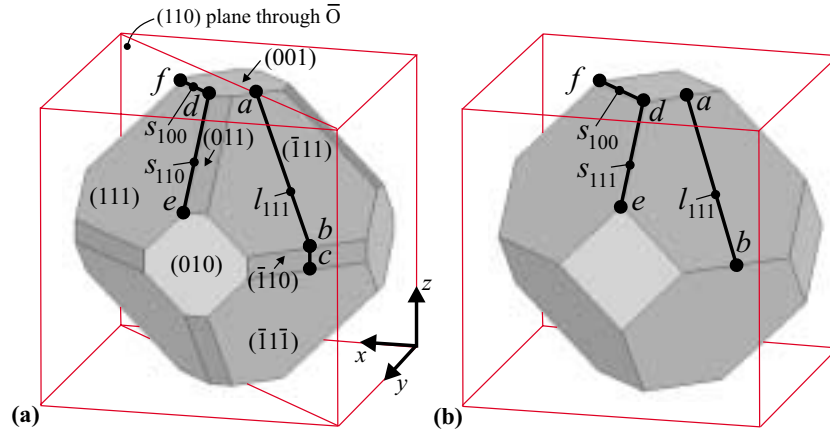


Figure 4.5: Wulff shapes showing relevant points and quantities. (a) Cluster containing small (110) facets. (b) Cluster without the (110) facets.

by Vitos *et al.* [82]. The one in Fig. 4.5(b) was obtained by neglecting the presence of the small (110) facets, but still using the surface free energies of the (111) and the (100) facets from the calculations of Vitos *et al.*

4.4.1 The facet planes

Origo is taken as the Wulff point, i.e. the center point of the free cluster. Then the equation for a plane containing \vec{r}_0 with \hat{n} as the normal vector is:

$$(\vec{r} - \vec{r}_0) \cdot \vec{n} = 0$$

We will now only consider planes which can be spanned by Miller indices (hkl) , with a normal vector \vec{n}_{hkl} . Taking \vec{r}_0 as the distance from the Wulff point to the center of a (hkl) facet, then

$$\vec{r}_0 = \gamma_{hkl} \cdot \frac{\vec{n}_{hkl}}{|\vec{n}_{hkl}|}$$

as the length of \vec{r}_0 per definition is γ_{hkl} , leading to:

$$\vec{r} \cdot \vec{n}_{hkl} = \gamma_{hkl} \sqrt{h^2 + k^2 + l^2} \quad (4.20)$$

which can be used to describe all facet planes in the Wulff shape.

4.4.2 Width of the (111) plane

The width of the (111) plane is found as the length of the line from a to b on Fig. 4.5(a).

Coordinates of point a : Point a is the common point of a (110) plane through the center, the (001) plane and the $(\bar{1}11)$ plane. Inserting these three planes into Eq. (4.20) one finds three equations for the three coordinates:

$$\begin{aligned} \text{(110) plane: } & \begin{pmatrix} x \\ y \\ z \end{pmatrix} \cdot \begin{pmatrix} 1 \\ 1 \\ 0 \end{pmatrix} = 0 \Rightarrow x + y = 0 \\ \text{(001) plane: } & \begin{pmatrix} x \\ y \\ z \end{pmatrix} \cdot \begin{pmatrix} 0 \\ 0 \\ 1 \end{pmatrix} = \gamma_{100} \Rightarrow z = \gamma_{100} \\ \text{(\bar{1}11) plane: } & \begin{pmatrix} x \\ y \\ z \end{pmatrix} \cdot \begin{pmatrix} -1 \\ 1 \\ 1 \end{pmatrix} = \sqrt{3}\gamma_{111} \Rightarrow -x + y + z = \sqrt{3}\gamma_{111} \end{aligned}$$

which are easily combined to yield the coordinates for point a :

$$a = \begin{pmatrix} x_a \\ y_a \\ z_a \end{pmatrix} = \begin{pmatrix} -\sqrt{3}/2\gamma_{111} + 1/2\gamma_{100} \\ \sqrt{3}/2\gamma_{111} - 1/2\gamma_{100} \\ \gamma_{100} \end{pmatrix} \quad (4.21)$$

Coordinates of point b : Point b is the common point of a (110) plane through origo, the $(\bar{1}10)$ plane and the $(\bar{1}11)$ plane. Inserting these three planes into Eq. (4.20) and solving the three equations, the coordinates of point b are found to be:

$$b = \begin{pmatrix} x_b \\ y_b \\ z_b \end{pmatrix} = \begin{pmatrix} -\sqrt{2}/2\gamma_{110} \\ \sqrt{2}/2\gamma_{110} \\ \sqrt{3}\gamma_{111} - \sqrt{2}\gamma_{110} \end{pmatrix} \quad (4.22)$$

The width of the (111) facet is the length of the line from a to b :

$$l_{111} = \sqrt{|ab|^2}$$

First the square of the length is calculated:

$$\begin{aligned} |ab|^2 &= \left| \begin{pmatrix} -\sqrt{2}/2\gamma_{110} \\ \sqrt{2}/2\gamma_{110} \\ \sqrt{3}\gamma_{111} - \sqrt{2}\gamma_{110} \end{pmatrix} - \begin{pmatrix} -\sqrt{3}/2\gamma_{111} + 1/2\gamma_{100} \\ \sqrt{3}/2\gamma_{111} - 1/2\gamma_{100} \\ \gamma_{100} \end{pmatrix} \right|^2 \\ &= \left| \begin{pmatrix} \sqrt{3}/2\gamma_{111} - \sqrt{2}/2\gamma_{110} - 1/2\gamma_{100} \\ -\sqrt{3}/2\gamma_{111} + \sqrt{2}/2\gamma_{110} + 1/2\gamma_{100} \\ \sqrt{3}\gamma_{111} - \sqrt{2}\gamma_{110} - \gamma_{100} \end{pmatrix} \right|^2 \end{aligned}$$

Since this length expression is on the form: $(\alpha X, \beta X, \gamma X)$ where α , β and γ are constants, the square of the length reduces to: $(\alpha^2 + \beta^2 + \gamma^2)X^2$, the length of the (111) facets is the positive root:

$$\begin{aligned} l_{111} &= \sqrt{|ab|^2} \\ &= \sqrt{(1 + 1 + 2^2)(-\sqrt{3}/2\gamma_{111} + \sqrt{2}/2\gamma_{110} + 1/2\gamma_{100})^2} \\ &= -3/\sqrt{2}\gamma_{111} + \sqrt{3}\gamma_{110} + \sqrt{3/2}\gamma_{100} \end{aligned} \quad (4.23)$$

One should remember the Wulff constant, otherwise Eq. (4.23) does not make sense.

4.4.3 Various features of a free cluster

In this section, most of the interesting points and length expressions of the Wulff construction are expressed in terms of the surface free energies of the close-packed surfaces. All points are found by calculating the crossing point of three planes using Eq. (4.20), all lengths are found as the length of a line between two points, as in Eq. (4.23). The expressions are given both on a Wulff shape containing a small (110) facet as in Fig. 4.5(a), as well as on a Wulff shape without the small (110) facet as in Fig.4.5(b).

Center Points

The center point of a (hkl) plane is simply the coordinates of a vector pointing from the Wulff point to the facet center:

$$c_{\{hkl\}} = \frac{\gamma_{hkl}}{\sqrt{h^2 + k^2 + l^2}} \begin{pmatrix} h \\ k \\ l \end{pmatrix} \quad (4.24)$$

The points: a to f

The points are shown on Fig. 4.5(a).

$$\begin{aligned}
 a &= \begin{pmatrix} -\sqrt{3}/2\gamma_{111} + 1/2\gamma_{100} \\ \sqrt{3}/2\gamma_{111} - 1/2\gamma_{100} \\ \gamma_{100} \end{pmatrix} & b &= \begin{pmatrix} -\sqrt{2}/2\gamma_{110} \\ \sqrt{2}/2\gamma_{110} \\ \sqrt{3}\gamma_{111} - \sqrt{2}\gamma_{110} \end{pmatrix} \\
 c &= \begin{pmatrix} -\sqrt{2}/2\gamma_{110} \\ \sqrt{2}/2\gamma_{110} \\ -\sqrt{3}\gamma_{111} + \sqrt{2}\gamma_{110} \end{pmatrix} & d &= \begin{pmatrix} \sqrt{3}\gamma_{111} - \sqrt{2}\gamma_{110} \\ \sqrt{2}\gamma_{110} - \gamma_{100} \\ \gamma_{100} \end{pmatrix} \\
 e &= \begin{pmatrix} \sqrt{3}\gamma_{111} - \sqrt{2}\gamma_{110} \\ \gamma_{100} \\ \sqrt{2}\gamma_{110} - \gamma_{100} \end{pmatrix} & f &= \begin{pmatrix} \sqrt{2}\gamma_{110} - \gamma_{100} \\ \sqrt{3}\gamma_{111} - \sqrt{2}\gamma_{110} \\ \gamma_{100} \end{pmatrix}
 \end{aligned} \tag{4.25}$$

The points: b' to f'

The points are shown on Fig. 4.5(b).

$$\begin{aligned}
 b' &= \begin{pmatrix} -\sqrt{3}/2\gamma_{111} \\ \sqrt{3}/2\gamma_{111} \\ 0 \end{pmatrix} & d' &= \begin{pmatrix} 0 \\ \sqrt{3}\gamma_{111} - \gamma_{100} \\ \gamma_{100} \end{pmatrix} \\
 e' &= \begin{pmatrix} 0 \\ \gamma_{100} \\ \sqrt{3}\gamma_{111} - \gamma_{100} \end{pmatrix} & f' &= \begin{pmatrix} \sqrt{3}\gamma_{111} - \gamma_{100} \\ 0 \\ \gamma_{100} \end{pmatrix}
 \end{aligned} \tag{4.26}$$

4.4.4 Ratios on a cluster with a (110) facet

The criterion for a cluster to contain a (110) can be found in many ways, one way is to simply ensure that the extent of the (110) facet is finite, thus

$$\begin{aligned}
 l_{110} > 0 &\Rightarrow 2\sqrt{3}\gamma_{111} - 2\sqrt{2}\gamma_{110} > 0 \\
 &\Rightarrow \frac{\gamma_{110}}{\gamma_{111}} < \sqrt{\frac{3}{2}}
 \end{aligned} \tag{4.27}$$

The extent of the small (110) facet with respect to the (111) facet is:

$$\frac{l_{110}}{l_{111}} = \frac{|bc|}{|ab|} = \frac{2\sqrt{3}\gamma_{111} - 2\sqrt{2}\gamma_{110}}{-3/\sqrt{2}\gamma_{111} + \sqrt{3}\gamma_{110} + \sqrt{3/2}\gamma_{100}} \tag{4.28}$$

The extent of the (100) edge with respect to the (110) edge is:

$$\frac{s_{100}}{s_{110}} = \frac{|df|}{|de|} = \frac{-\sqrt{3}\gamma_{111} + 2\sqrt{2}\gamma_{110} - \gamma_{100}}{-\sqrt{2}\gamma_{110} + 2\gamma_{100}} \quad (4.29)$$

4.4.5 Ratios on a cluster without a (110) facet

The extent of the (111) facet is:

$$w = l_{111} = |ab'| = \sqrt{\frac{3}{2}}\gamma_{100} \quad (4.30)$$

The extent of the (100) edge with respect to the (111) edge is:

$$\frac{s_{100}}{s_{111}} = \frac{|d'f'|}{|d'e'|} = \frac{\sqrt{6}\gamma_{111} - \sqrt{2}\gamma_{100}}{-\sqrt{6}\gamma_{111} + 2\sqrt{2}\gamma_{100}} \quad (4.31)$$

Introducing, $g = \gamma_{100}/\gamma_{111}$, and $s = s_{100}/s_{111}$, g and s are related as:

$$s = \frac{\sqrt{3} - g}{2g - \sqrt{3}} \quad (4.32)$$

$$g = \sqrt{3} \frac{s + 1}{2s + 1} \quad (4.33)$$

4.4.6 A supported cluster

The Pd nanocrystals are found to be supported on a (111) facet, and therefore only this case will be considered here. A cross section of a cluster supported on a (111) facet is shown in Fig. 4.6, which also contains a table of relevant angles and lengths. These are easily found by considering the (110) plane in an FCC lattice. Here we will take the opinion that the cluster in (a) possesses the smallest possible (110) facet, while the cluster in (b) only possesses a (110) step.

For a supported cluster it is possible to express the effective surface free energy, γ^* , in terms of the height-to-width ratio and the surface free energies. Dividing the height: $h = \gamma_{111} + \gamma^*$ of a supported cluster with the width of the top facet, γ^* is found to be:

$$\gamma^* = \frac{h}{w}l_{111} - \gamma_{111} \quad (4.34)$$

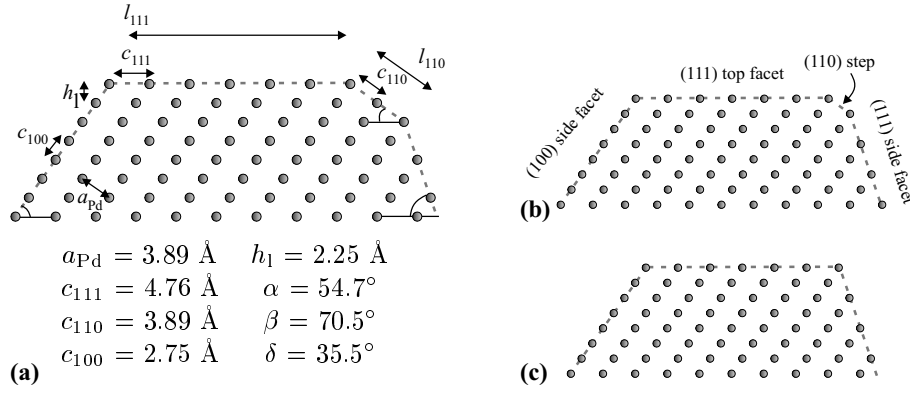


Figure 4.6: Atomistic model of a supported nanocrystal. (a) Cluster containing a (110) facet. (b) Cluster containing a (110) step. (c) Cluster without a (110) facet.

Inserting the width of the top facet from Eq. (4.23) yields:

$$\gamma^* = \frac{h}{w} \left(\frac{-3}{\sqrt{2}} \gamma_{111} + \sqrt{3} \gamma_{110} + \sqrt{\frac{3}{2}} \gamma_{100} \right) - \gamma_{111} \quad (4.35)$$

which in the case of a cluster without a (110) facet simplifies to (see Eq. (4.30))

$$\gamma^* = \sqrt{\frac{3}{2}} \frac{h}{w} \gamma_{100} - \gamma_{111} \quad (4.36)$$

and by using Eq. (4.33) it is possible to express the relative surface free energy as:

$$\tilde{\gamma}^* = \frac{\gamma^*}{\gamma_{111}} = \frac{3}{\sqrt{2}} \frac{h}{w} \frac{s+1}{2s+1} - 1 \quad (4.37)$$

The relationship between the adhesion energy and γ^* was defined in Eq. (4.15). The adhesion energy can in the general case be expressed as:

$$\begin{aligned} W_{\text{adh}} &= \gamma_{111} - \gamma^* \\ &= 2\gamma_{111} - \frac{h}{w} \left(\frac{-3}{\sqrt{2}} \gamma_{111} + \sqrt{3} \gamma_{110} + \sqrt{\frac{3}{2}} \gamma_{100} \right) \end{aligned} \quad (4.38)$$

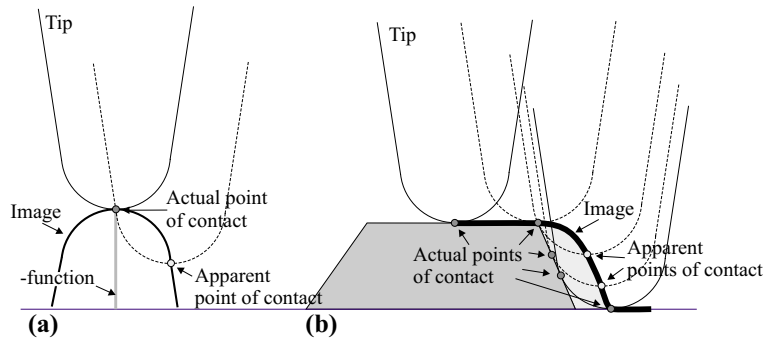


Figure 4.7: Schematic illustration of tip broadening. (a) Very sharp feature images the tip. (b) Extended object is broadened by the tip.

which in the case without a (110) facet simplifies to (expressed as a relative adhesion energy):

$$\begin{aligned}\widetilde{W} &= 1 - \widetilde{\gamma}^* \\ &= 2 - \frac{3}{\sqrt{2}} \frac{h}{w} \frac{s+1}{2s+1}\end{aligned}\quad (4.39)$$

As will become evident later, s and h/w can be measured on the nanocrystals, which means that the relative adhesion energy has been expressed solely in quantities which are experimentally measurable.

4.5 Tip broadening of a 3D cluster

The remaining part of the chapter will concentrate on imaging of nanocrystals. First the tip broadening will be discussed briefly.

The STM has mainly been used to study atomically flat surfaces, and the goal has in many cases been to obtain atomic resolution. For this type of experiments only the apex of the tip is important. If the STM is applied to sample surfaces which possess extended 3D features, the shape of the tip also becomes important and features are broadened and/or distorted.

Tip broadening is illustrated in Fig. 4.7. The problem arises from the separation of the actual point of contact and the apparent point of contact.

The apparent point of contact is the point on the tip which accounts for the tip position, i.e. the tip apex. The actual point of contact is the position on the tip which is closest to any feature on the sample, i.e. the point (or points) which carries the dominant part of the tunnel current. In Fig. 4.7(a) a case is presented where the sample feature is shaped like a δ -function whereas the tip has a finite size. For the tip apex situated right above the sample feature, the closest point is certainly the apex itself, but as soon as the tip apex is placed beside the sample feature the top of the sample feature hits the side of the tip and thereby inhibits the tip from reaching the flat part of the surface. In this ideal case the emerging image is that of the tip. The main conclusion from this example is that no real 3D feature observed in an STM image is smaller than the tip. When a feature with a finite size is imaged with a finite tip, the emerging image is a convolution between the tip shape and the true cluster shape [83,84], resulting in a broadening of the sample feature; this is illustrated in Fig. 4.7(b).

It is possible to some extent to correct for the tip broadening, using e.g. the method of blind reconstruction [83,84]. This does, however, not serve any purpose for the images obtained in connection with this thesis. The strong influence of the tip shape upon imaging of nanosize clusters has been elegantly demonstrated for Rh clusters residing onto the oxide film by Stempel *et al.* [85].

4.6 Nucleation and growth of Pd on Al₂O₃

The general nucleation and growth behaviour of Pd on Al₂O₃/NiAl(110) will now be addressed. At RT palladium nucleates exclusively along step edges and at domain boundaries. Point defects on the oxide domains do not act as nucleation centers. The nucleation sites can be verified at low coverage ($\lesssim 1$ ML) by scanning at high positive bias voltage so that the domain boundaries protrude (Fig. 4.8), or by scanning at a scale so that the underlying substrate can be resolved (Fig. 4.9). At higher coverage on high quality films, the clusters are observed to line up, see Figs. 4.10(a), (b) and 4.11(a). This suggests that nucleation continues at domain boundaries. On films of medium quality, a prominent line structure of the Pd clusters is only recognized at low coverage, whereas the Pd clusters appear nearly uniformly distributed at higher coverage (Fig. 4.10(c)). The apparently more random distribution of the clusters on a film of medium quality is on the basis of images such as Fig. 4.9, ascribed to the distribution of the underlying domain boundaries.

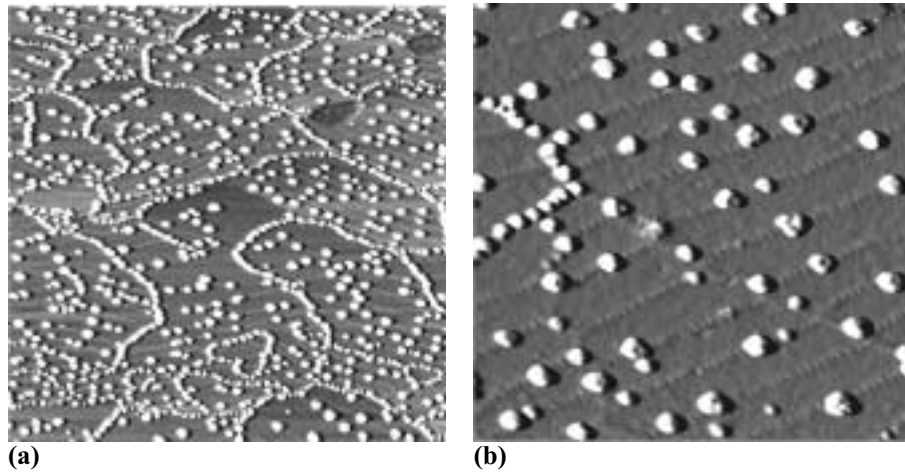


Figure 4.8: STM images of 0.25 ML of Pd deposited on $\text{Al}_2\text{O}_3/\text{NiAl}(110)$. The Pd clusters have nucleated at step edges and at domain boundaries exclusively. (a) $3000 \times 3000 \text{ \AA}^2$, $U_s = 6.9 \text{ V}$, $I_t = 0.8 \text{ nA}$. (b) $1000 \times 1000 \text{ \AA}^2$, $U_s = 5.2 \text{ V}$, $I_t = 0.8 \text{ nA}$.

On low quality films, i.e. films with areas of unordered defect structure, the Pd clusters are uniformly distributed on the areas with the unordered defect structure. An example is given in Fig. 4.10(d). In the upper left part of the image the clusters are distributed similarly to the clusters on a medium quality film, whereas the clusters in the lower right part reside on an area with unordered defect structure and are uniformly distributed.

From the images in Figs. 4.8, 4.9 and 4.10, it can be readily verified that the growth mode of Pd on $\text{Al}_2\text{O}_3/\text{NiAl}(110)$ is Volmer-Weber growth.

The above discussion has been concerned with nucleation and growth at RT. In connection with this thesis work, experiments have been performed only at or above RT. The nucleation and growth above RT will be described in section 4.14. The Freund group has published some measurements concerning the growth of Pd at 90 K [27,68]. At 90 K the step edges and domain boundaries still act as nucleation centers. A large fraction of the clusters is, however, also found to have nucleated on the domains, presumably at point defect [68].

Focus is now turned towards the morphology of the nanocrystals. In the

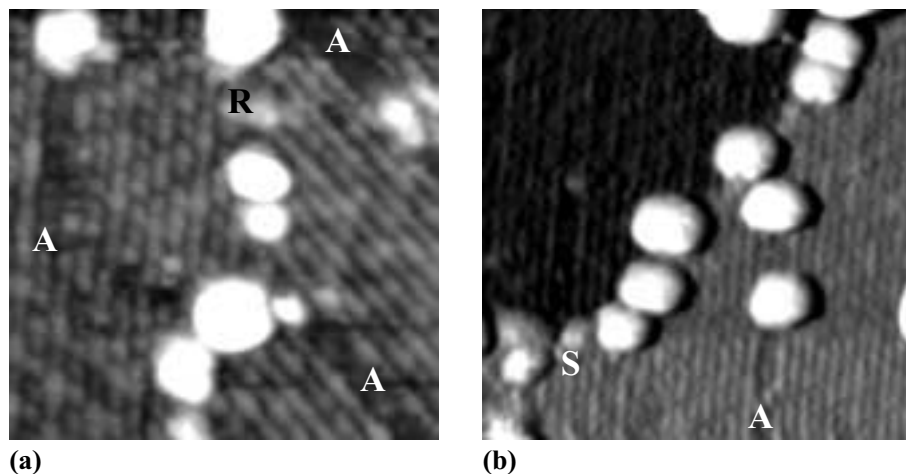


Figure 4.9: STM images of 0.5 ML of Pd deposited on $\text{Al}_2\text{O}_3/\text{NiAl}(110)$. Antiphase domain boundaries (A), reflection domain boundaries (R) and a step edge (S) are marked. (a) $200 \times 200 \text{ \AA}^2$, $U_s = -1.1 \text{ V}$, $I_t = -0.7 \text{ nA}$. (b) $300 \times 300 \text{ \AA}^2$, $U_s = -1.3 \text{ V}$, $I_t = -1.6 \text{ nA}$.

following the word *nanocrystal* will refer to clusters which appear well-ordered in the STM images, i.e. clusters which possess a flat top facet and are hexagonal shaped (see e.g. Fig. 4.10(b)). The word (nano)cluster will refer to any cluster, irrespective of the detailed shape.

Nanocrystals form spontaneously when Pd is deposited at RT, and the maximum number is observed for palladium coverages between $\sim 1 \text{ ML}$ and $\sim 2.5 \text{ ML}$ on a high quality film. The absence of nanocrystals at low coverage is most likely due to a tip broadening effect, not a real absence of nanocrystals. A flat top facet is simply not recognized until a certain minimum width is reached. Nanocrystals have been found from coverages larger than $\sim 0.25 \text{ ML}$, where the top facet of the smallest nanocrystals have obtained a width of $20\text{-}30 \text{ \AA}$. These clusters are $5\text{-}10 \text{ \AA}$ high, corresponding to $2\text{-}4$ layers. At a coverage of 2.5 to 3 ML , the clusters became too large for the tip to reach the substrate in most areas, and also coalescence becomes prominent.

The step edges are the most prominent nucleation sites, but the clusters which nucleate there rarely appear on a well-ordered form. On high quality

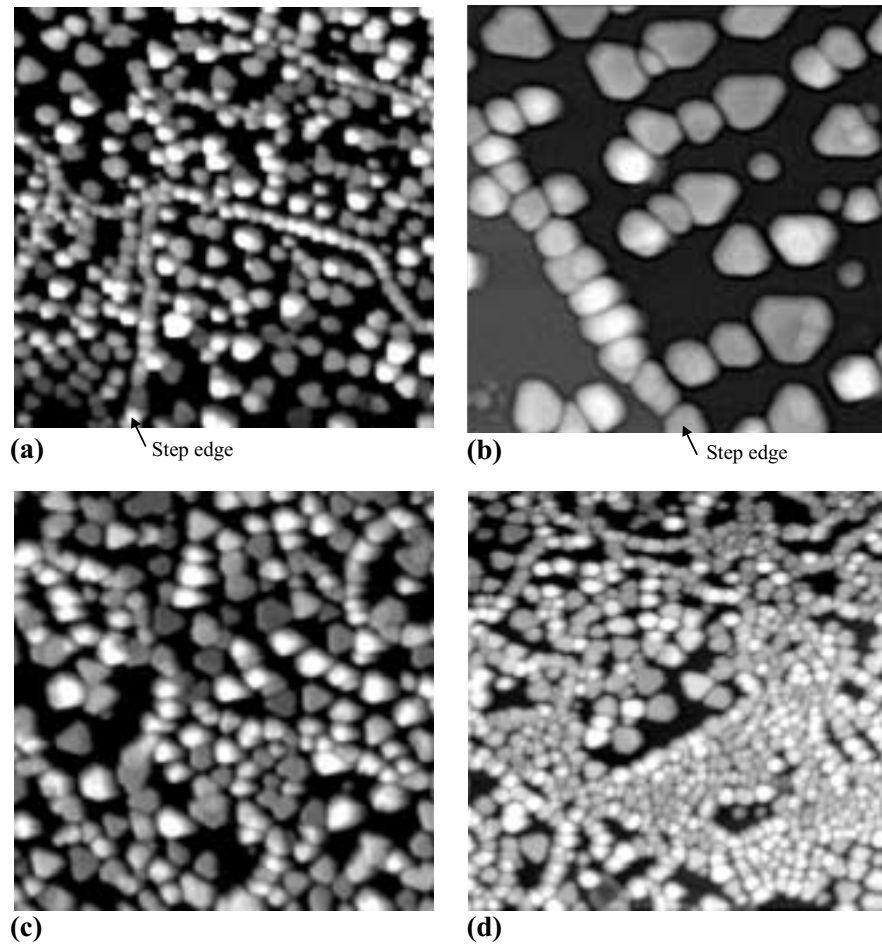


Figure 4.10: STM images showing different types of cluster distributions. (a) $2000 \times 2000 \text{ \AA}^2$, $U_s = 1.1 \text{ V}$, $I_t = 1.1 \text{ nA}$. (b) $700 \times 700 \text{ \AA}^2$, $U_s = -1.5 \text{ V}$, $I_t = -0.9 \text{ nA}$. (c) $1500 \times 1500 \text{ \AA}^2$, $U_s = 1.1 \text{ V}$, $I_t = 1.1 \text{ nA}$. (d) $2000 \times 2000 \text{ \AA}^2$, $U_s = 0.9 \text{ V}$, $I_t = 1.1 \text{ nA}$.

films up to $\approx 50\%$ of the clusters which have nucleated away from the step edges appear crystalline in shape. This fraction may be significantly smaller on low quality films. At the step edges the density of hexagonal clusters is lower than along the domain boundaries, and the overall cluster density is higher. This can be seen from the images in Figs. 4.10(a), (b) and 4.11(a), where both the step edges and the domain boundaries are decorated.

Comparing the images in Fig. 4.10 with respect to the number of hexagonally shaped clusters, one finds that it is not straight-forward to determinate whether a cluster is hexagonally shaped or not. The determination is best done with the human eye, but still, it can be quite tedious on large-scale images and/or if the tip is blunt.

It has been discussed how the quality of the film influences the spatial distribution of Pd clusters. The quality of the film also influences the size distributions and the cluster densities; this can be verified by a comparison of the upper left part of Fig. 4.10(d) with the lower right part. The quality of the film only influences the number of well-ordered clusters: the better the film, the larger the fraction of well-ordered clusters. No correlation between the morphology of the nanocrystals and the quality of the film has been observed.

4.7 Orientation

The nanocrystals which have nucleated on the domains are oriented with respect to the unit mesh of the oxide film. This was first found in a LEED experiment [27] and will be confirmed in the following.

The orientation of a nanocrystal is characterized by a set of all three close-packed directions of the (111) top facet, and the orientation of these three directions with respect to the [001] direction of the underlying NiAl-substrate. In this way clusters separated by 60° or 120° are regarded as orientated along the same direction.

Due to the presence of two domains, the nanocrystals fall into two groups which are separated by an angle of $10 \pm 3^\circ$. This separation is consistent with the expected one of 9° , due to the fact that the angular separation of the oxide unit mesh on each reflection domain is 51° around the [001] direction of the NiAl(110) substrate (see Fig. 3.1(a)).

A cluster is orientated on the oxide domain, so that one of the $\langle 11 \rangle$ -directions of the hexagonal cluster mesh is aligned to the close-packed direction of the oxide unit mesh (see Fig. 4.11(b)). The nanocrystals nucleate on the domain

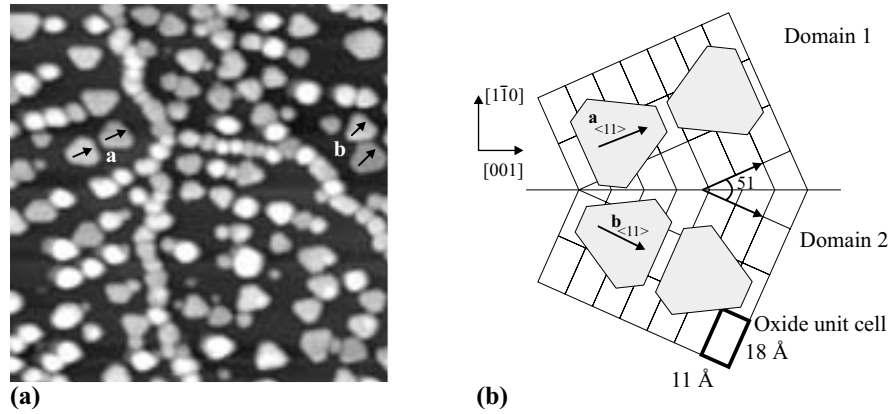


Figure 4.11: (a) STM image with the $\langle 11 \rangle$ -cluster direction indicated on a couple of clusters. $1500 \times 1500 \text{ \AA}^2$, $U_s = -1.5 \text{ V}$, $I_t = -0.8 \text{ nA}$. (b) Model of the cluster orientation.

boundaries, and this orientation corresponds to an alignment along the straight segments of the antiphase domain boundaries (see Fig. 3.5(a)), which run along the close-packed direction of the oxide unit mesh. A few nanocrystals have been found to be oriented in a random direction. This is most likely related to nucleation on an antiphase domain segment which breaks away from the close-packed direction of the oxide unit mesh.

The image in Fig. 4.11(a) shows an area where the two domain orientations are present, and a couple of clusters have been marked with the $\langle 11 \rangle$ -cluster direction. Figure 4.11(b) illustrates the orientation of the nanocrystals on the oxide unit mesh, and shows the equivalent clusters rotated 60° (a rotation of 120° would bring the cluster back to the same orientation). The orientation measurements were done only on atomically resolved clusters to have a clear determination of the close-packed Pd directions. Atomic resolution on the Pd nanocrystals is discussed in section 4.9.

4.8 Apparent cluster height

In section 3.7 the bias dependence of the apparent height of the film was discussed. This height-bias variation has implications for height measurements and line profiles of metal clusters supported on the oxide film. A such effect was first noted for supported Pt clusters by Bertrams *et al.* [86], although no systematic investigation was performed. In this section we provide a systematic investigation of the height-bias dependence of the supported palladium clusters.

In Fig. 4.12 line profiles across supported Pd nanocrystals are shown for different bias voltages. As in the case of the apparent height of the film, no height variation is observed when applying a negative or low positive bias voltage. For positive bias the apparent height depends on the magnitude of the bias. Above ~ 2 V, the apparent height of the cluster decreases steadily until it reaches ~ 4 V. The change in apparent height amounts to 5 Å, different from the 3.5 Å observed for the film hole measurements presented in section 3.7.

If the properties of the film away from the clusters are unaffected by the evaporated Pd, then the reference level for the cluster height measurements would go up by the 3.5 Å originating from the film when increasing the (positive) bias and the clusters would appear 3.5 Å lower. To explain the consistently observed change of 5 Å, other effects related to either the film or the presence of the Pd clusters must be invoked as well.

The electron transport through the Pd cluster is considerably more complicated than through the film. The tip/vacuum/cluster/oxide/NiAl system forms two mesoscopic tunnel junctions coupled in series. Under proper conditions, a such system may exhibit quantum dot characteristics, i.e. phenomena related to single electron tunneling events, such as the Coulomb blockade and the Coulomb staircase. Although the presence of any significant Coulomb blockade can be excluded, because it is possible to draw current through the clusters even at very low bias voltages ($\lesssim 1$ mV), it is still worth considering whether the current-voltage characteristics could be influenced by quantum size effects. In order to observe quantum dot characteristics the charging energy: $E_c = e^2/2C$ should be larger than the thermal energy: $k_B T$ (25 meV at RT) [87]. Here C denotes the cluster's capacitance to the surroundings. It suffices to consider the tunnel junction with the largest capacitance [88], which is the junction: cluster/oxide/NiAl. The capacitance of the system is approximated by that of a parallel-plate capacitor, using a film thickness of 5 Å, a dielectric constant for the Al₂O₃ film of $10 \epsilon_0$ [89], and a circular contact area with $r \sim 25$ Å.

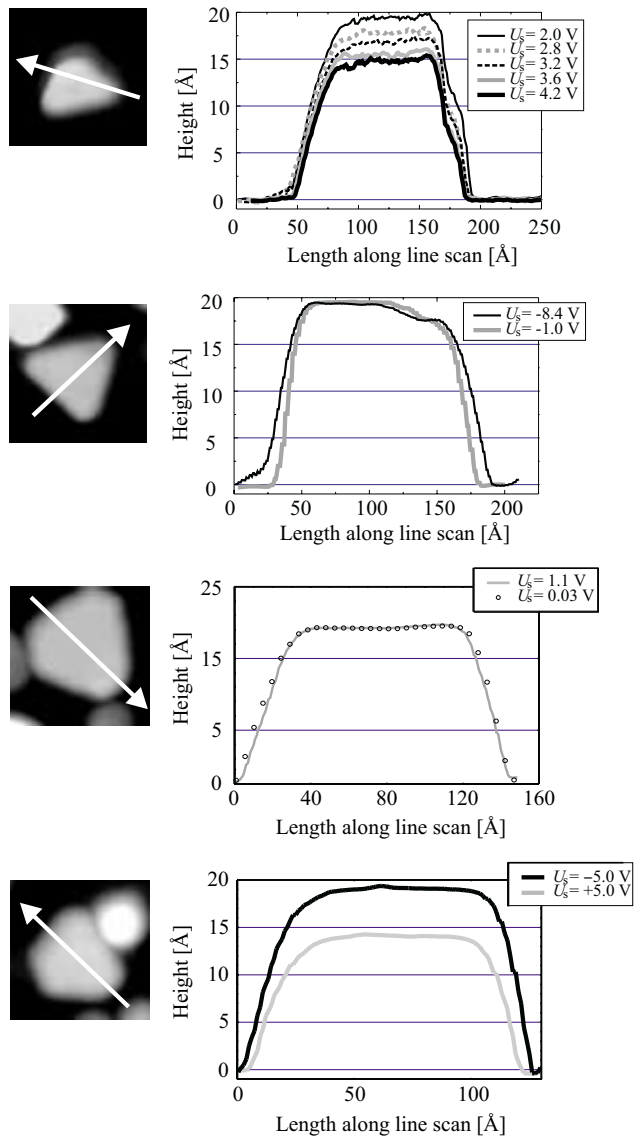


Figure 4.12: Line profiles of Pd nanocrystals, at different bias voltages. Line scans were acquired along the indicated lines with a tunnel current of 0.5 nA in the case of positive bias voltage, and -1 nA in the case of negative bias voltage.

height, h_a , is the tip height above the substrate, and h_b the tip height above the cluster. If the tunneling current is totally unaffected by the presence of the film then $h_a \approx h_b$ and the measured height is the cluster height plus the film height. In order to extract the correct cluster height, the measured cluster height should be reduced by the film height. The film height has been measured to be ~ 5 Å [54], but due to a possible difference in h_a and h_b , as well as a possible effect of the thin film, a reduction of 5 Å may be slightly incorrect.

The reference level at high positive bias is unclear. For the tip residing above the film, it is certainly at least 3.5 Å higher than the substrate. Assuming that the reference level above the cluster is the same as above the film, the exact level is unimportant as it cancels out in the subtraction. The measured height is then, $H_H = (h_\beta + h_\gamma) - (h_\alpha)$. In the simplest case the tip height above the film and above the cluster is the same, and the measured cluster height is the true cluster height. This may be too simplified, but due to the exponential height dependence in the tunnel current, it is expected to be correct within 1-2 Ångströms.

4.9 Atomic-resolution on the Pd nanocrystals

The present section addresses the atomic-level structure of the nanocrystals. As observed in Figs. 4.14 and 4.15, it is indeed possible to zoom in and obtain atomic resolution on the top layer of the ordered clusters. The atomic arrangement of the top layer facet is seen to be that of a (111) layer, with a nearest neighbor distance (measured as an average over several clusters) of $d = 2.76 \pm 0.07$ Å, equivalent to that of the (111) plane of Pd ($d = 2.75$ Å). Thus, no evidence of any significant strain in these clusters is found. This was not to be expected either. Recent measurements based on TEM have shown that for both Pt and Pd clusters residing on the Al₂O₃ film, the lattice constant decreases with decreasing cluster size. For Pd, a lattice constant reduction of 5% was observed for 12 Å clusters [91, 92]. The smallest Pd clusters, on which it was possible to image with atomic resolution, have a width of ≈ 40 Å, and most of the crystalline clusters are higher than 4 layers.

It is possible to obtain atomic resolution across the entire cluster surface. At the edge of the top facet, the tunneling current from the tip will change from being drawn from the outermost tip-apex atom to being drawn from somewhere on the side of the tip, normally resulting in loss of resolution. This

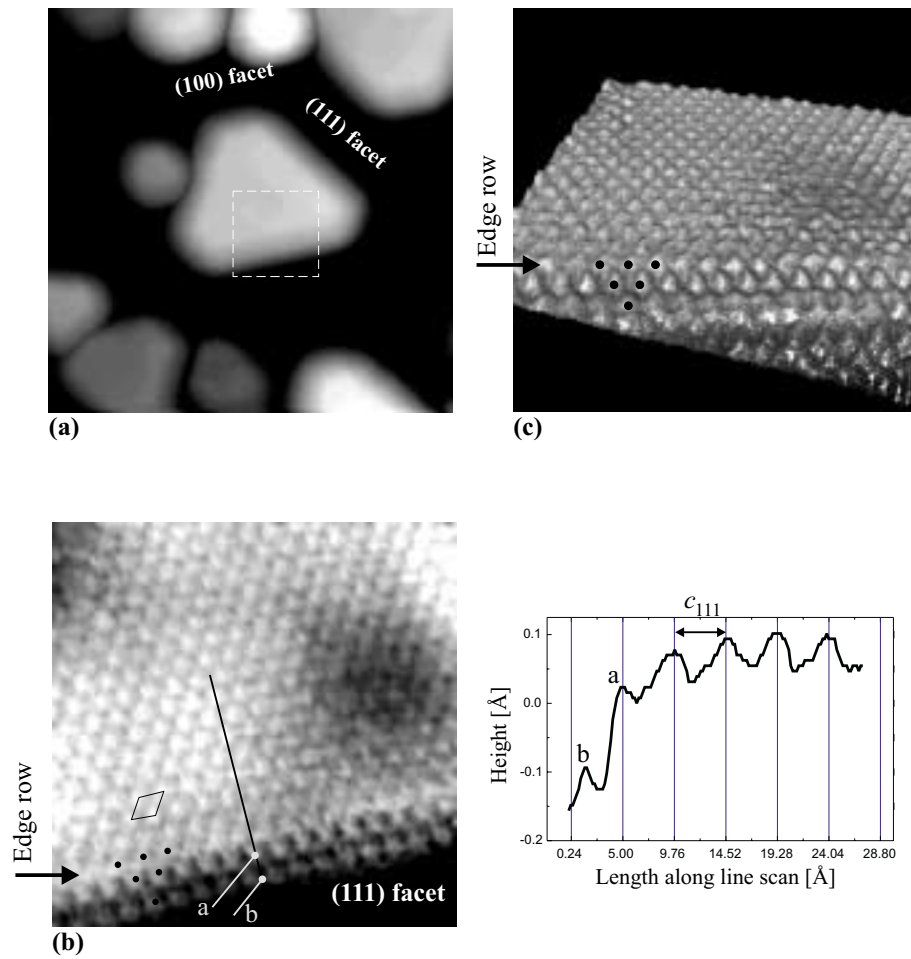


Figure 4.14: Zooming in on a Pd nanocrystal. (a) $300 \times 300 \text{ \AA}^2$, $U_s = 1.1 \text{ V}$, $I_t = 1.1 \text{ nA}$. (b) Zoom of the marked part in (a) and a line scan along the indicated line, c_{111} can be found on Fig. 4.6. Surface unit cell indicated. $50 \times 50 \text{ \AA}^2$, $U_s = -0.9 \text{ mV}$, $I_t = -1.6 \text{ nA}$. (c) 3D view of (b). Dots in (b) and (c) indicate atomic positions consistent with a (111) facet.

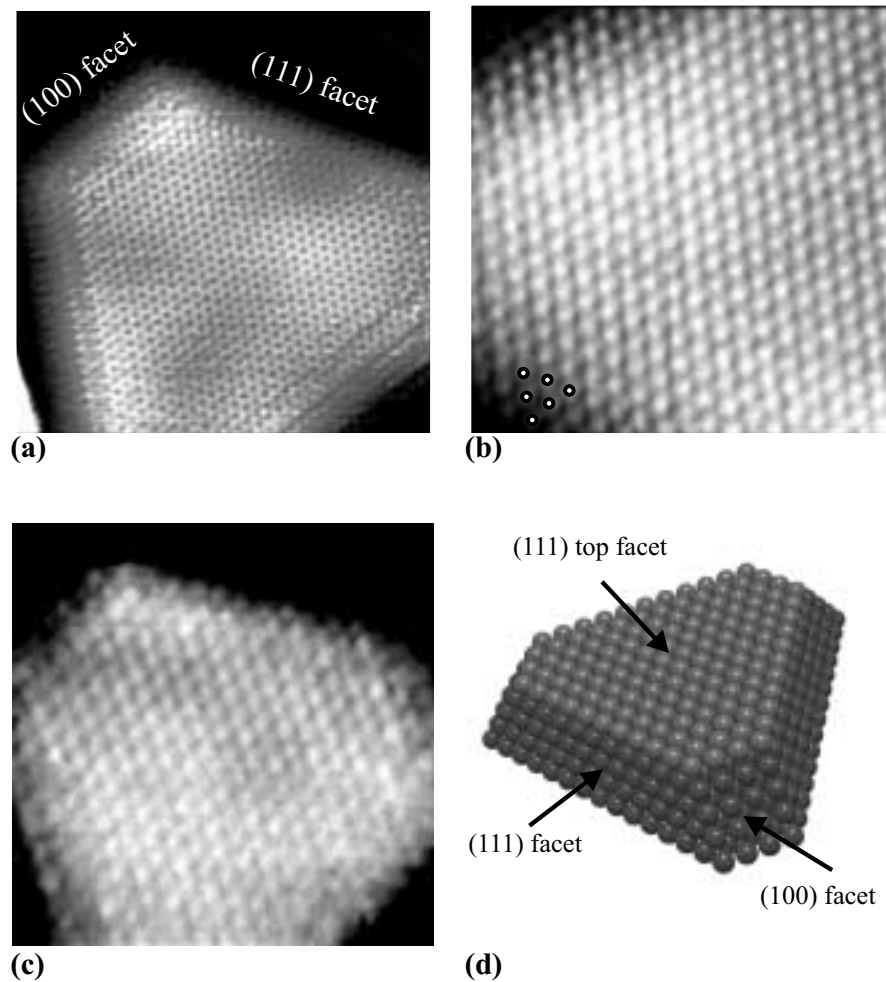


Figure 4.15: Attomically resolved STM images of Pd nanocrystals. (a) $100 \times 100 \text{ \AA}^2$, $U_s = -5 \text{ mV}$, $I_t = -0.8 \text{ nA}$. (b) $50 \times 50 \text{ \AA}^2$, $U_s = -1.5 \text{ mV}$, $I_t = -1.8 \text{ nA}$. Dots indicate atomic positions consistent with a (111) facet. (c) One of the smallest nanocrystals on which atomic resolution could be obtained. $50 \times 50 \text{ \AA}^2$, $U_s = 3.4 \text{ mV}$, $I_t = 1.0 \text{ nA}$. (d) Ball model of the observed Pd cluster shape.

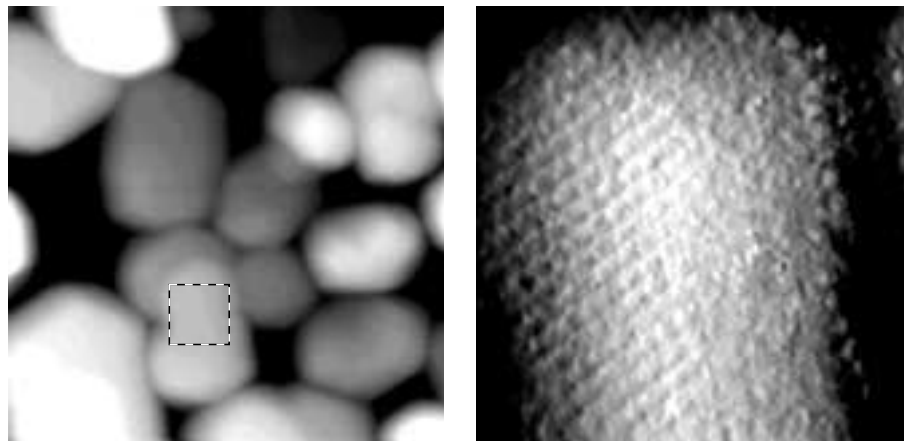


Figure 4.16: STM image with atomic or near atomic resolution on a semi-ordered cluster. (a) $300 \times 300 \text{ \AA}^2$, $U_s = 1.3 \text{ V}$, $I_t = 1.2 \text{ nA}$. (b) Zoom of (a). $50 \times 50 \text{ \AA}^2$, $U_s = 2 \text{ mV}$, $I_t = 2.1 \text{ nA}$.

makes it extremely difficult to achieve insight into the structure of the side facets. In a few cases, however, it has been possible to maintain the atomic resolution a few layers down on the larger facets. This is the case for the cluster in Fig. 4.14 of which a 3D view of the edge is shown in (c), as well as the clusters in Fig. 4.15(b), where the atomic positions of the uppermost few layers are marked. These images clearly demonstrate that the larger side facets are (111) facets. According to the crystal structure of Pd, the smaller facets are then (100) facets. A ball model of the Pd nanocrystals is presented in Fig. 4.15(c). The Wulff construction predicts different slopes of the two facets, and the identification of the facets has been confirmed by comparing the apparent steepness of the side facets.

The apparent height difference between two subsequent layers on the atomically resolved clusters is somewhat less than 2.25 \AA , which is the height difference between two adjacent (111) planes in bulk palladium. The discrepancy is related to tip broadening. There is always a clear level difference between the observed layers. This is most apparent in the 3D image in Fig. 4.14(c), or in the line scan in (b), where point a is on the edge atom, and point b is on the bridge between the two atoms in the second highest layer. In the cases where

resolution down on the side facets have been obtained along the larger sides, the symmetry is always that of a (111) plane. But one should note that resolution down on the facets has only been obtained on approximately 10 clusters. If the resolution of the side facet originated in double imaging of the top facet edge, the positioning of the second and third highest layer would be random.

Finally, we briefly touch upon unordered/semi-ordered clusters. As seen on Fig. 4.16 it is indeed also possible to zoom in and obtain atomic or near atomic resolution on clusters which are not flat on the top facet. It is, however, not straightforward to obtain qualitative information from the image. No resolution is observed on the right side, neither can any specific symmetry be assigned to the protrusions. The imaging of unordered clusters is more difficult than imaging the nanocrystals, and imaging of unordered clusters has therefore not been pursued in detail.

4.10 Planarity of the top facet

As mentioned previously, up to 50% of the clusters appear well-ordered. A closer inspection reveals that the top facet of nearly all of the nanocrystals is not planar, but depressed in the center zone.

In Fig. 4.17 two non-planar clusters are shown. By non-planarity we mean clusters where all the atoms in the top layer belong to the same crystal plane, but still a clear curvature of the top facet is observed. The top facet protrude in the edge region. Usually the (100)-edges protrude more than the (111)-edges, giving rise to a depressed area as indicated on the clusters in Fig. 4.17. Line profiles of the clusters are also presented. The apparent depth of the depression varies from cluster to cluster, but is usually below 1 Å. The example given in Fig. 4.17(b) is quite extreme, it should be noted that the depression is 2.5 Å over 130 Å, thus the effect is quite exaggerated by the representation. Although no clear correlation between cluster size and the depth of the depression has been observed, the effect is more pronounced on larger than on smaller clusters. The depressed area is seldom found to be completely symmetric, but that could originate from instrumental distortion.

First, one should consider instrumental effects, such as overshooting. Overshooting would stem from a retardation of the STM feedback loop, when the tip crosses over from scanning up the steep side facet and moves along the flat top facet. Such overshooting can be encountered if the scan speed is too high or the gain too low. Overshooting can easily be excluded. The protrusion at the

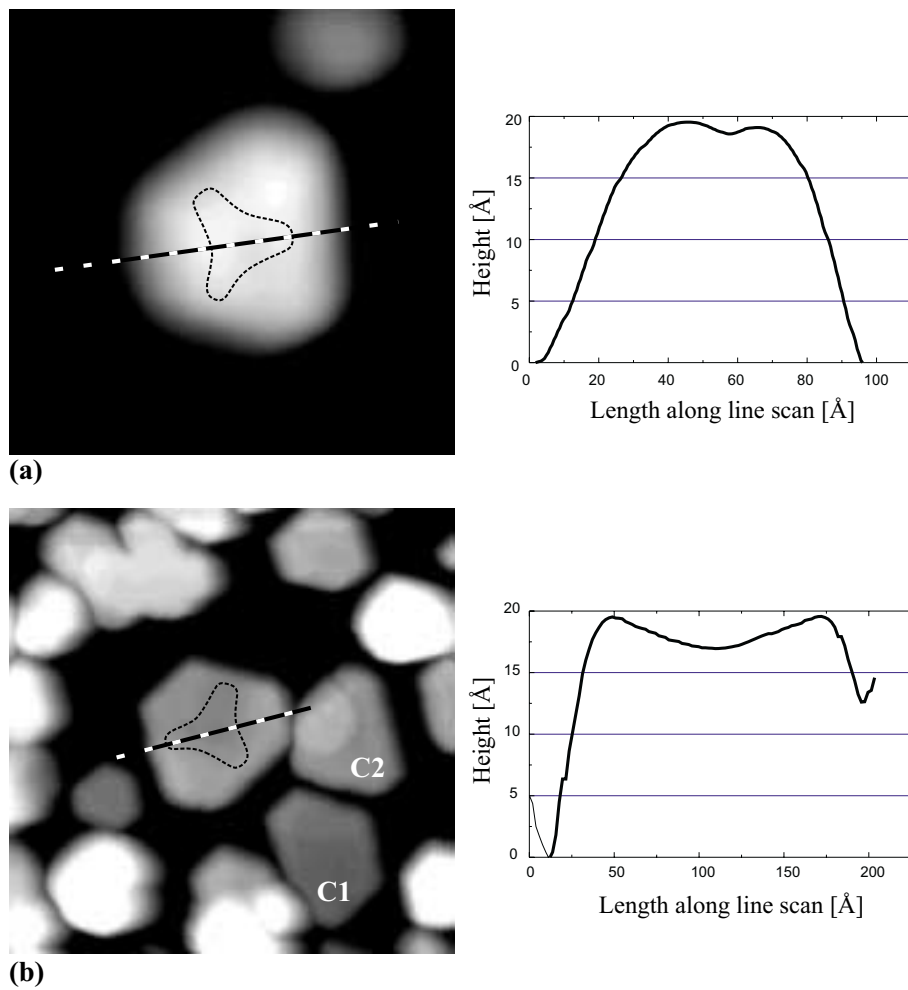


Figure 4.17: Palladium nanocrystals with a non-planar top facet. The dotted line indicates the depressed area. Clusters designated C1 and C2 are clusters which have undergone coalescence. (a) $150 \times 150 \text{ \AA}^2$, $U_s = -1.3 \text{ V}$, $I_t = -1.2 \text{ nA}$. (b) $500 \times 500 \text{ \AA}^2$, $U_s = 1.1 \text{ V}$, $I_t = 1.3 \text{ nA}$.

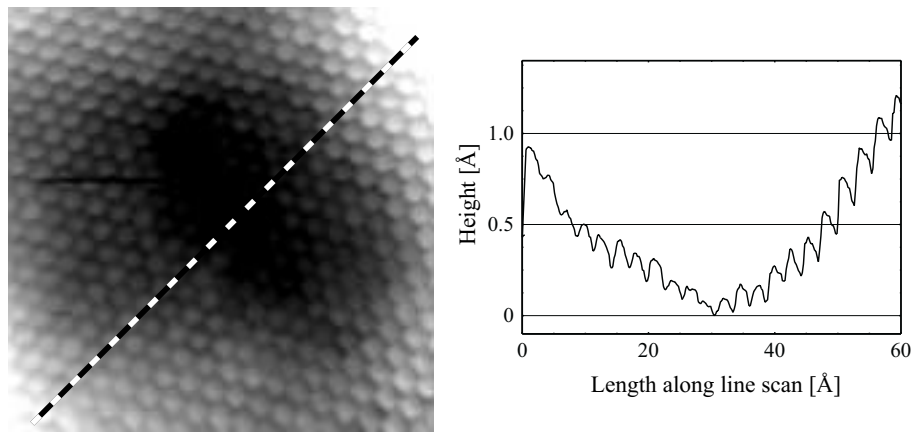


Figure 4.18: Atomically resolved nanocrystal with a non-planar top facet. The image has been acquired in the center zone of the cluster in Fig. 4.17(b). $50 \times 50 \text{ \AA}^2$, $U_s = -7 \text{ mV}$, $I_t = -1.6 \text{ nA}$.

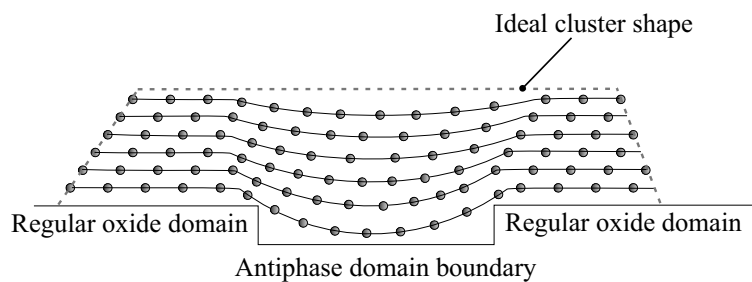


Figure 4.19: Model of the possible origin of the non-planarity observed on most nanocrystals.

edges does not depend upon whether the tip crosses over from the side facet to the top facet, or vice versa, and furthermore, the curvature of the central part remains even when scanning in the center zone of a large cluster, as shown in Fig. 4.18. Secondly, even though it has been shown that there is no overall strain in large clusters [92], small strain field could still be present around the cluster edges due to the general undercoordination of the atoms positioned there. In which way a such strain field influences the LDOS is unclear, but it does not seem unreasonable that the electronic wavefunction would leak differently into vacuum at the corners and edges compared to the central part of the cluster. Finally, the non-planarity could also be an effect of the interface between the nanocrystal and the substrate. An atomic force microscopy study of the clean film have revealed that the real space domain boundaries are depressed with respect to the surface of the oxide domain [25, 65]. The nanocrystals nucleate on the domain boundaries, but as they grow larger they spread beyond the boundary zone, and force the bottom facet to be non-planar. The effect probably diminishes up through the layers of the cluster, and whether it can sustain up through the cluster is unclear. A model of the effect is shown in Fig. 4.19. The model exaggerates the effect. If the cluster has not grown symmetrically around the domain boundary, the effect would also account for why not all clusters have a symmetrically depressed area. Any of these possibilities, or combinations of some of them, could likely be the reason for the non-planarity of the top facet.

4.11 Cluster morphology

Since the apparent shape results from a convolution between the actual cluster and tip shapes, care should be taken when analyzing the detailed 3D shape of the nanocrystals based on STM measurements. Three characteristic cluster parameters can, however, be measured convincingly from STM line scans: the height, the width of the top facet, and the ratio between the side lengths of the top facet. These parameters were measured on 79 nanocrystals formed by Pd evaporation at RT and at elevated substrate temperature. In this section, however, only the RT measurements will be discussed; the measurement at elevated temperatures will be discussed in section 4.14. Figures 4.20(a) and (b) illustrate how the various parameters are related to the nanocrystals.

The height of a nanocrystal can be measured if the cluster lies isolated from other clusters, so that the substrate level can be determined. The cluster height

was measured on images obtained at low bias, and therefore reduced by 5 Å, as discussed in section 4.8. The possible systematic error of 1-2 Å caused by this method was included in the error bars.

Measurements of the cluster width have already been discussed in section 4.5, where it was illustrated how the tip broadens the cluster. In order to investigate how well one can estimate the true width of the top facet, the apparent width of the cluster in Fig. 4.20(a) is compared to the true width, which can be obtained from an atomically resolved image of the same cluster, as shown in (c). On the atomically resolved image the edge rows have been identified, so the true width is obtained. A line scan of the atomically resolved top facet is shown in (d).

The hexagon superimposed on the image in (a) reflects the true width obtained from the atomically resolved line scan, and in (b) the edges are marked with arrows on the line scan. At first sight it appears as if the measurements of the apparent width exaggerate the true cluster width. Comparing it with the atomically resolved line scan in (d), it is, however, seen that there is, in fact, a rather good agreement between the two line scans. It is thus evident that the width of the top facet can be determined from images as (a) without atomic resolution. Only very few clusters fulfill the criterion of lying isolated from other clusters and at the same time also being resolved atomically. The line scans have, therefore, been measured exclusively on overview images. The uncertainty of the width measurements has been estimated to 10% of the measured width based on considerations as those presented above.

In Fig. 4.21 the height-to-width ratio (aspect ratio) is plotted against the cluster width, revealing a clear correlation. The smaller clusters have a larger aspect ratio than the larger clusters. In general, the aspect ratio for a strain-free nanocrystal which possesses its equilibrium shape, is independent of volume, i.e. the supported crystal shape is self-similar. This is clearly not the case here. For the clusters with a top-facet width larger than ~ 55 Å, the height-to-width ratio, however, stabilizes at:

$$h/w = 0.18 \pm 0.03$$

Relatively few, fairly isolated clusters with a top facet larger than 85 Å were observed. This is due to the fact that more than ~ 3 ML of palladium is necessary in order to grow an appreciable amount of such large clusters. At that coverage only in few areas is the substrate exposed, and height determination is not possible.

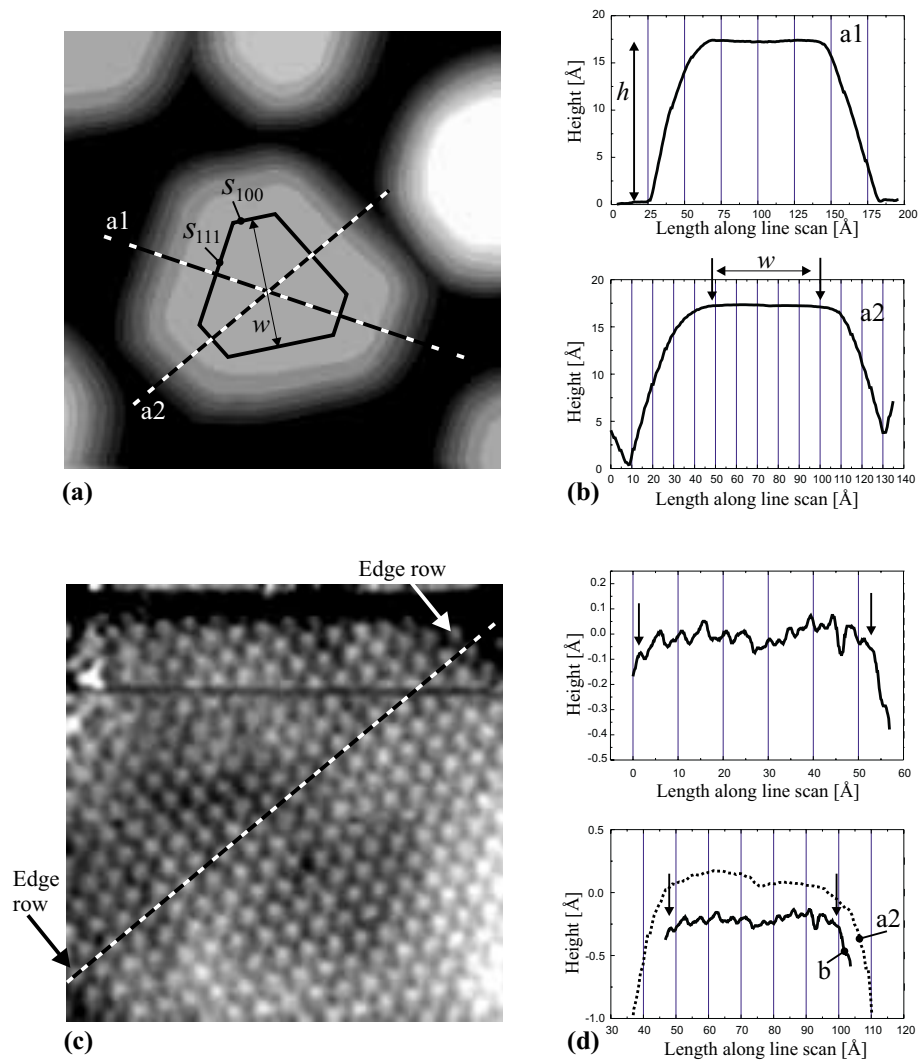


Figure 4.20: (a) Contour representation of an STM image showing characteristic cluster parameters. $200 \times 200 \text{ \AA}^2$, $U_s = 1.1 \text{ V}$, $I_t = 1.0 \text{ nA}$. (b) Line scans along the indicated lines in (a). (c) Atomic resolution on the top facet of the cluster in (a). $50 \times 50 \text{ \AA}^2$, $U_s = -4 \text{ mV}$, $I_t = -1.1 \text{ nA}$. (d) Line scan along the indicated line in (c), and a comparison with a corresponding line scan obtained from the overview image in (a).

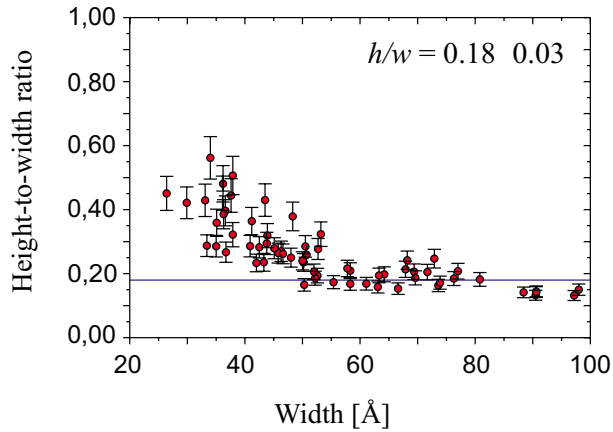


Figure 4.21: Height-to-width ratio of 55 Pd nanocrystals deposited at RT.

The side length ratio is found to be uncorrelated with the cluster size, and yields:

$$s = s_{100}/s_{111} = 0.4 \pm 0.1$$

The fairly large error bar is a result of prominent tip rounding of the corners, which makes it difficult to determine s_{100} and s_{111} precisely. The error bar is based on an estimate.

4.11.1 Imperfect nanocrystals

Only few clusters possess a step and terrace on the top facet. Two examples are given in Fig. 4.22. The actual fraction of imperfect nanocrystals varies a lot from preparation to preparation and even from area to area; but it ranges from 10 to 25%. The terraces are hexagonally shaped and the step height is ~ 2.25 Å, the separation between (111)-planes in bulk palladium. The size of such terraces varies from only a few atoms to an almost complete coverage of the the top facet.

Some of the larger nanocrystals have undergone coalescence. Examples of such nanocrystals are given in Fig. 4.17(b). The cluster designated C1 has emerged from the coalescence of two growing nanocrystals, resulting in this

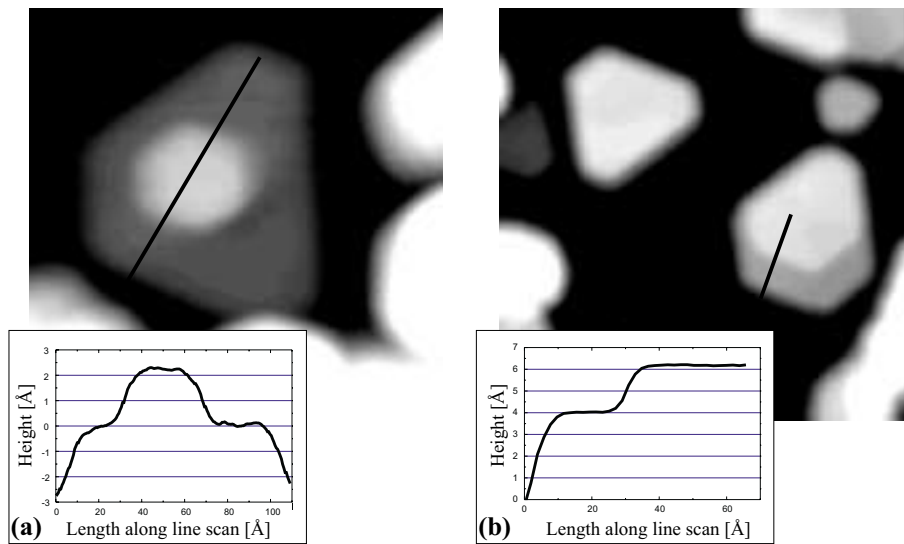


Figure 4.22: STM images of nanocrystals with a terrace. Line scans are along the indicated lines. (a) $150 \times 150 \text{ \AA}^2$, $U_s = 0.8 \text{ V}$, $I_t = 1.1 \text{ nA}$. (b) $300 \times 300 \text{ \AA}^2$, $U_s = 1.1 \text{ V}$, $I_t = 0.9 \text{ nA}$.

very elongated hexagonally shaped cluster. The cluster designated C2 has emerged from the coalescence of a nanocrystal and an unordered cluster.

4.12 Observed shape vs. Wulff shape

In the following we try to clarify whether the observed nanocrystal shape corresponds to the equilibrium shape.

4.12.1 Wulff shapes

In order to find the Wulff shape the surface free energies, which are *a priori* unknown, are needed. As a starting point we will use the two most recent sets of free energies obtained from DFT calculations by Methfessel *et al.* [93] and Vitos *et al.* [82]. Both calculations were conducted using the LDA approxi-

mation, but different calculational methods are applied. The calculations of Methfessel *et al.* include relaxations, where a relaxation of the topmost layer is taken into account.

The theoretical surface free energy values are applicable only at 0 K. According to Tyson and Miller [78], the surface free energy is, however, only weakly dependent upon the temperature, and the difference between the surface free energy obtained at 0 K and at RT is only a few percent. The magnitudes of both sets of surface free energies are in fair agreement with non-orientation specific values derived from experiments [78,94].

Figure 4.23 shows four different Wulff shapes. The Wulff shape in (a) is obtained using the values from Methfessel *et al.* In (b), the Wulff shape is obtained using the values from Vitos *et al.* Assuming for a moment that the Pd nanocrystals possess their equilibrium shape, it is possible from the measured side length ratio and Eq. (4.33) to find the corresponding equilibrium shape. The Wulff shape presented in (c) is obtained using the measured side length ratio, whereas the cluster in (d) is the Wulff shape that one would obtain if the side facet assignment had been wrong, such that the larger edges were (100) edges, and the smaller ones (111) edges. From observing just the side length ratio it is not possible to distinguish between (c) and (d), atomic resolution down on one of the side facets is necessary. As atomic resolution has been obtained on the (111) side facets, it can therefore be ascertained that the observed cluster shape corresponds to (c).

4.12.2 The side length ratio

A comparison between the observed side length ratios and the calculated ones raises a small dilemma. Since a (110) facet is not observed on the atomically resolved images, does the measured side length ratio correspond to the s_{100}/s_{110} ratio on a cluster where a (110) facet has not developed, or does it correspond to a cluster which does not contain a (110) facet, so that it should be compared to the s_{100}/s_{111} ratio? The reason why this is a problem, is a strong dependence on the ratio between the surface free energies of the (110) and the (111) facets. Inserting the surface free energies of Vitos *et al.* in Eqs. (4.29) and (4.32) one finds: $s_{100}/s_{110} = 0.43$ and $s_{100}/s_{111} = 0.75$, respectively, which are rather different values. Geometrically the diversity is easily understood. Removing the (110) facet corresponds to pushing it outwards until the top and the side (111) facets meet. This, simultaneously diminishes the (111) side length and enlarges the (100) side length.

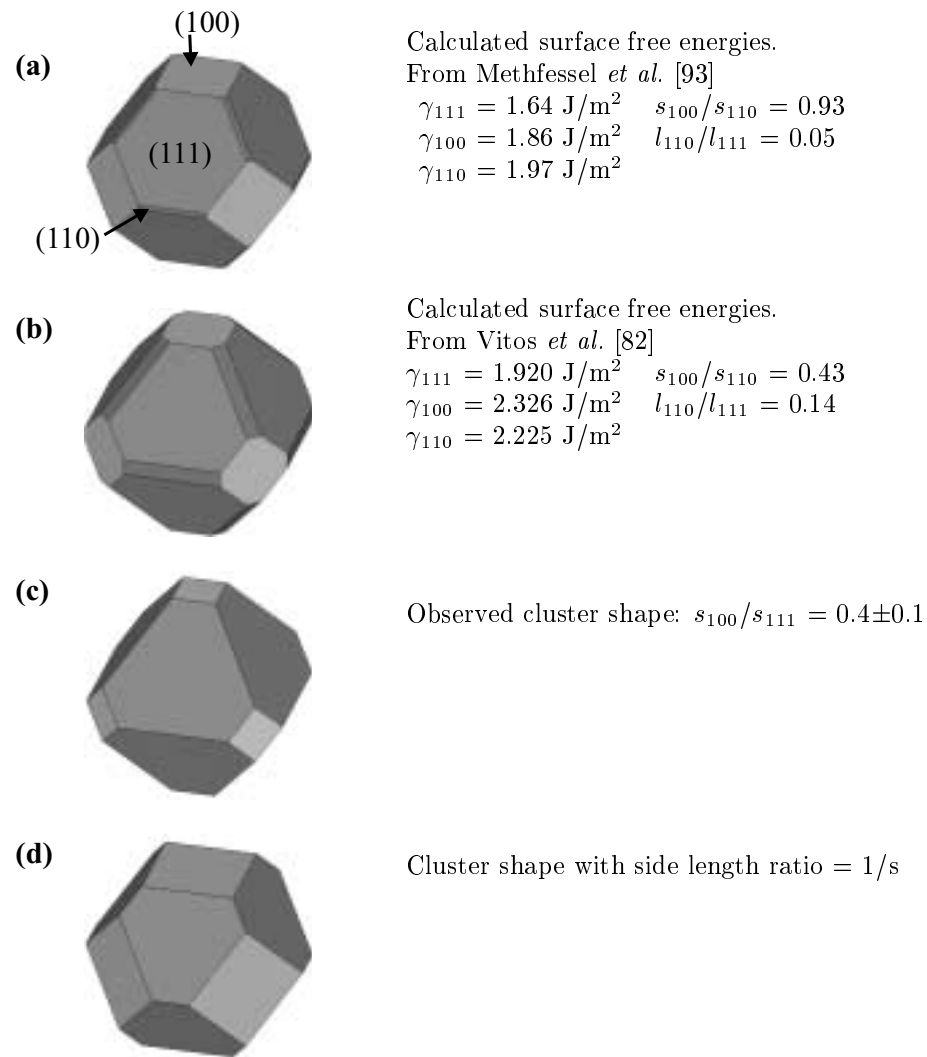


Figure 4.23: (a) and (b) Wulff construction obtained from calculated surface free energies. (c) and (d) Wulff constructions derived from the measured s_{100}/s_{111} value.

Our point of view is that since the theoretical surface free energies lead to a cluster shape containing a (110) facet, the experimentally observed side length ratio: s_{100}/s_{111} , should be compared to the s_{100}/s_{110} ratio. Good agreement between the observed and the calculated side length ratios is then found for the values of Vitos *et al.*, whereas the side length ratio of 0.93, obtained using the values from Methfessel *et al.*, does not compare well to the observed ratio of 0.4. The side length ratio depends strongly on the ratios between the surface free energies. The surface free energies of Methfessel *et al.* can be brought into the observed side length by changing the ratio: $\gamma_{100}/\gamma_{111}$ by 8%, or by changing $\gamma_{110}/\gamma_{111}$ by 13% while keeping the other fixed. If both ratios are changed simultaneously a change of only a few percent is needed.

4.12.3 The (110) facet

The Wulff shapes in both Figs. 4.23(a) and (b) show the presence of a (110) facet. For a nanocrystal to develop a genuine (110) facet, the facet should be two lattice constants wide, thus the width of the top facet should be larger than: $2 \times c_{110}/(l_{110}/l_{111})$ (see Fig. 4.6 and Eq. (4.28)). A nanocrystal should develop a (110) facet if the top facet is larger than:

	Vitos <i>et al.</i> :	Methfessel <i>et al.</i>
(110) facet	$l_{111} > 56 \text{ \AA}$	$l_{111} > 311 \text{ \AA}$
(110) step	$l_{111} > 28 \text{ \AA}$	$l_{111} > 156 \text{ \AA}$

The cluster shown in Fig. 4.14 is $\sim 75 \text{ \AA}$ wide, thus, according to the values from Vitos *et al.*, the cluster is large enough to possess a (110) facet, but clearly it does not. In this case the values from Methfessel *et al.* compare best to the observed cluster shape. As for the side length ratio, the presence of the (110) facet is critically dependent on the ratio, $\gamma_{110}/\gamma_{111}$. If $\gamma_{110}/\gamma_{111} < \sqrt{3/2}$ the (110) facet would not develop for any cluster size (see Eq. (4.27)). Changing the surface free energy ratio of Vitos *et al.* by merely 6% would remove the (110) facet from the Wulff construction.

The two theoretical Wulff shapes are somewhat different. The observed cluster shape lies in between and compares better to one with respect to the side length ratio, and better to the other with respect to the presence of the (110) facet. Taking into account that the Wulff construction is a continuum model neglecting edges and corners, that we have neglected the finite temperature and the uncertainties in the theoretical values, good agreement is, however,

actually found between the observed nanocrystal shape and both of the Wulff shapes obtained from calculated surface free energies.

4.12.4 The h/w ratio

A variation in the height-to-width ratio with nanocrystal size (Fig. 4.21), seems at first to oppose that the nanocrystals possess their equilibrium shape. The variation can, however, be rationalized. It may be a size effect related to a contribution from corners and edges to the total surface free energy. For very small clusters a such effect can be present. The smallest nanocrystals are, however, already quite large. If the surface free energies of clusters with a top facet larger than 20-25 Å depended on the cluster size, the variation of h/w should be accompanied by a variation in the side length ratio as the side length ratio is a direct function of the surface free energies of the various facets. Since such a variation is not observed, the variation of the height-to-width ratio is rather an effect of the interface.

All nanocrystals nucleate on domain boundaries, and as they grow larger they spread beyond the boundary zone and onto the regular film surface. This means that very small clusters are only in contact with a domain boundary, whereas very large clusters are mainly in contact with the regular film. The ratio between bottom facet area and domain boundary area shows a weak linear dependence on the cluster size. Clusters which have a top facet smaller than ~ 15 Å are solely in contact with domain boundary. With a top facet ~ 55 Å the fraction is 2.5, whereas for clusters around 80 Å it is 4. Assuming that the binding between the Pd cluster and the domain boundary is different from the binding between the Pd cluster and the oxide domain, the total binding of a Pd cluster is a mean value between the actual area in contact with the different kinds of surface. If the mixed interface leads to a correlation between cluster size and adhesion energy, such that the effective adhesion energy is lower for smaller clusters than for larger clusters, the variations in h/w with the width of the top facet is consistent with the assumption that the Pd nanocrystals possess their equilibrium shape. The structural details of the Pd/domain boundary interface are, however, unknown. It would be very interesting to perform HRTEM experiments to clarify how the bottom of the Pd nanocrystals accommodate to the mixed substrate surface.

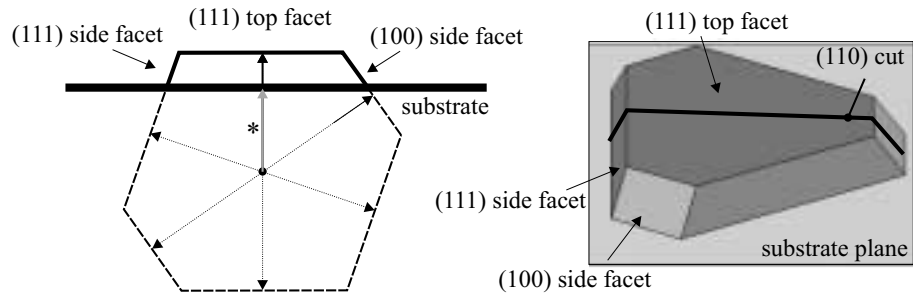


Figure 4.24: Observed supported Wulff shape of the Pd nanocrystals.

4.12.5 Growth shape or equilibrium shape?

We find that the data are consistent with the notion that the Pd nanocrystals possess their equilibrium shape, rather than a kinetically determined growth shape. The basis for this statement is the following observations.

The nanocrystals form spontaneously. The majority of nanocrystals do not have steps on the top facet as one would expect if the nanocrystal possessed a growth shape. The larger ones possess a rather well defined shape, which compares, within a few percent, to the one expected from calculated surface free energies.

The supported Wulff shape, corresponding to the observed Pd nanocrystal shape, is presented in Fig. 4.24.

4.13 Adhesion energy

Having established that nanocrystals possess their equilibrium shape, the adhesion energy can be extracted from the measured shape.

The adhesion energy, W_{adh} , is a measure of the bonding properties of the cluster to the oxide film. It is defined as the work per unit area needed to pull the system apart into its constituents, assuming no plastic or diffusional modifications. The adhesion energy has already been discussed in more general terms in section 4.3.3.

In the case where no (110) facet is present in the crossing between the top facet and the side facet, it is possible to express the relative adhesion

energy (Eq. (4.39)) by parameters which are purely experimentally observable. Including the (110) facet in this equation, it is no longer possible to express $\widetilde{W}_{\text{adh}}$ purely in experimental parameters, since there are no other experimental parameters available.

The relative effective surface free energy and adhesion energy are derived from Eqs. (4.37) and (4.39):

$$\begin{aligned}\widetilde{\gamma}^* &= -0.7 \pm 0.1 \\ \widetilde{W}_{\text{adh}} &= 1.7 \pm 0.1\end{aligned}$$

In order to find an absolute value of the adhesion energy, it is necessary to multiply the relative adhesion energy with the theoretical γ_{111} , or use Eq. (4.38) resulting in:

Without (110)	With (110)
$W_{\text{adh, meth}} = 2.8 \pm 0.2 \text{ J/m}^2$	$W_{\text{adh, meth}} = 2.9 \pm 0.2 \text{ J/m}^2$
$W_{\text{adh, vit}} = 3.3 \pm 0.2 \text{ J/m}^2$	$W_{\text{adh, vit}} = 3.4 \pm 0.2 \text{ J/m}^2$

Taking the mean value as our experimentally value, we obtain:

$$W_{\text{adh, exp}} = 3.1 \pm 0.2 \text{ J/m}^2$$

The error bar on W_{adh} comprises both statistical errors and a possible systematic error in cluster height of $\sim 1\text{-}2 \text{ \AA}$, originating from the compensation for the oxide film thickness.

The table above shows that the absolute size of the adhesion energy is not sensitive to whether or not the (110) facet is present, and equation Eq. (4.39) can be used to inspect the robustness of W_{adh} with respect to minor errors in h/w and s_{100}/s_{111} . This is done in Fig. 4.25. It can be seen from (b) that if h/w is kept constant, changing s_{100}/s_{111} does not have much of an effect, as expected. Changing h/w of course has an effect. The adhesion energy is, however, clearly robust with respect to minor errors in the measurement of h/w .

For most metal-on-oxide systems, the work of adhesion is either unknown or badly determined, and the theoretical understanding of the metal-oxide interface is still quite limited due to the complexity of such systems. Studies of trends have been undertaken based on semi-empirical cluster and slab calculations (for a review, see Ref. [95]). Only recently have *ab initio* density-functional

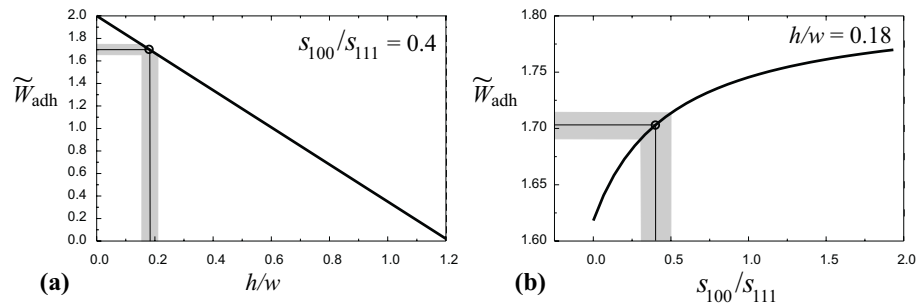


Figure 4.25: Graph of Eq. (4.39). (a) Keeping s_{100}/s_{111} fixed. (b) Keeping h/w fixed. Shaded area indicates the uncertainty related to the error bars.

calculations been carried out by Bogicevic and Jennison [63] on metal adsorption atop a 5 Å oxide film on Al(111) and Ru(0001). For a full monolayer of Pd on the thin aluminum oxide, a work of adhesion of 1.7 J/m² was derived, using the local-density approximation (LDA). For a 4 ML Pd film, this value changed to 1.95 J/m², while a calculation using the general gradient approximation (GGA) for the exchange-correlation term resulted in a value of only 1.05 J/m².

The values obtained by Bogicevic and Jennison deviate substantially from our experimental value of 3.1 J/m². Possible explanations for this discrepancy will now be discussed. The main concern is the structure of the ultra-thin Al_2O_3 film on Al(111) [63] which most likely deviates from the Al_2O_3 film grown on NiAl(110) [64]. If the film structure deviates to such an extent that γ^* is dramatically changed, a comparison is of course not relevant. In this light it is surprising to note that the value we have extracted from a similar analysis for the adhesion energy of Cu compares well to the calculations by Bogicevic and Jennison (see section 4.16). This agreement may, however, be coincidental. While the experimentally derived adhesion energy appears well-defined, the large dependency of the calculated adhesion energy on details of the computational approach (LDA vs. GGA) seems very surprising. A work of adhesion of 1.05 J/m² would correspond to a h/w ratio of ~ 0.6 , 3-4 times higher than the measured values. There is clearly a need for reliable data on other metal-oxide systems to allow for further comparison between experimental and theoretical results. Jennison and Bogicevic themselves have investigated the

discrepancy between the measured and their calculated adhesion energy [64]. Without taking a clear stand, they seem to believe that their film structure and the real structure of the Al_2O_3 film are too different for an agreement to be expected. Still they find a mechanism which can explain the discrepancy. If the two uppermost Al layers are free to relax when the structure is optimized, Al is freed from the substrate and moves into the film to form direct contact with the Pd clusters. This direct contact raises the adhesion to 4.5 J/m^2 if LDA is used, and to 3.8 J/m^2 if GGA is used. Thus, the adhesion can be larger than the experimental value. It is an interesting effect, that the adhesion can be increased by getting direct Pd-Al contact, but whether this effect, or that the two films are too different is the source of the disagreement, remains uncertain.

4.14 Temperature dependence of cluster morphology

The analysis presented above is based on the assumption that the Pd nanocrystals have their equilibrium shape. In order to stimulate the formation of equilibrium-shaped clusters, deposition of Pd above RT was investigated. It has already been shown that even a moderate increase in temperature by 100 K leads to a loss of Pd due to penetration of the oxide film [96]. We, however, speculated that for the material which actually stayed on the film, the enhanced thermal energy would stimulate nanocrystal growth. This is not the case.

At Pd deposition temperatures up to $100 \text{ }^\circ\text{C}$, no change in the overall appearance of the STM images, in the Pd AES signal or in the height-to-width ratio can be detected. However, between 100 and $150 \text{ }^\circ\text{C}$ drastic changes occur; the AES Pd signal decreases, which is in line with earlier LEED intensity measurements [96]; the height-to-width ratio increases (see Fig. 4.26), and the number of nanocrystals decreases dramatically. Two new types of clusters appear: (i) Very large clusters, which probably originate from a thermal increase in the mobility of the diffusing atoms. (ii) Flat clusters, which are most probably areas where Pd has penetrated into the film. An STM image of Pd deposited at $150 \text{ }^\circ\text{C}$ is shown in Fig. 4.26(a). Above $200 \text{ }^\circ\text{C}$ virtually no well ordered clusters are observed, and from $300 \text{ }^\circ\text{C}$ also the general cluster shapes are completely distorted by sintering of the clusters and severe incorporation into the film. An STM image of Pd deposition at $300 \text{ }^\circ\text{C}$ is presented in Fig. 4.27. It is interesting to note that some of the clusters are apparently completely flat, as shown by the line scan, and should allow for atomically resolved imag-

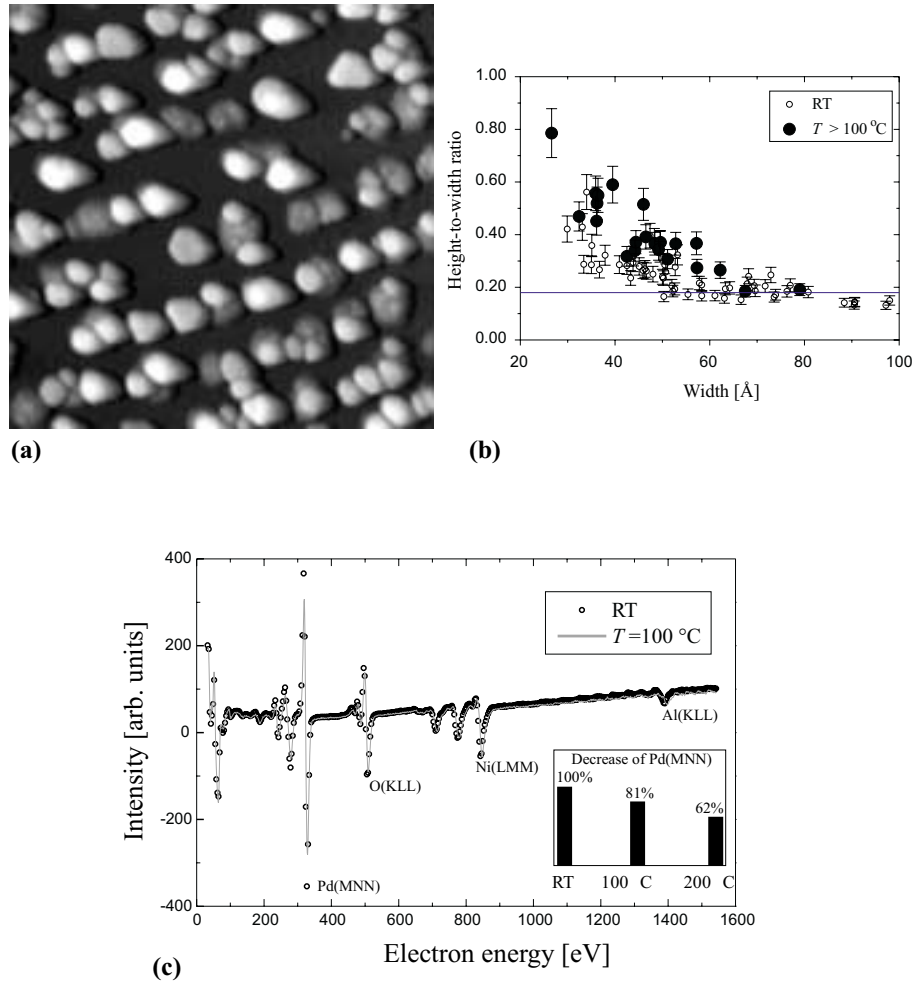


Figure 4.26: (a) STM image of ~ 2 ML of Pd deposited at $150\text{ }^\circ\text{C}$. $1000 \times 1000\text{ \AA}^2$, $U_s = 1.1\text{ V}$, $I_t = 0.9\text{ nA}$. (b) Height-to-width ratio of 24 clusters deposited at $T > 100\text{ }^\circ\text{C}$, together with the RT measurement. (c) Auger electron spectrum of 2 ML of Pd deposited at $100\text{ }^\circ\text{C}$.

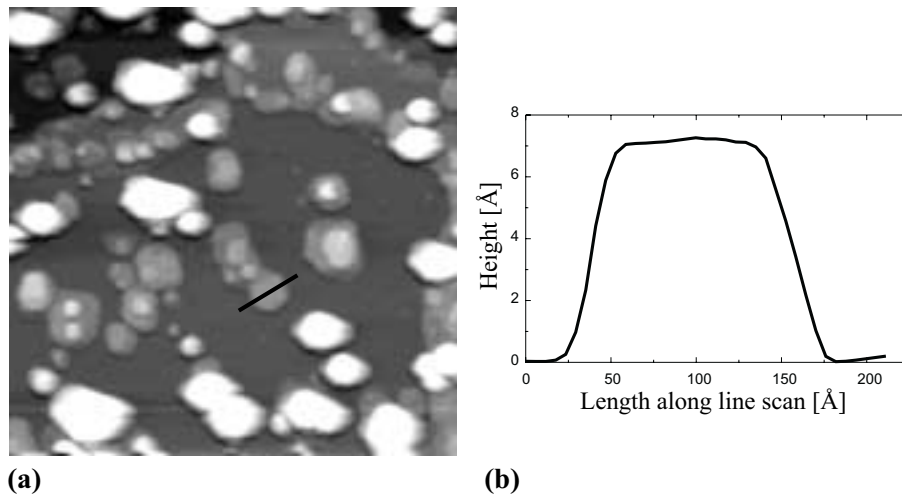


Figure 4.27: (a) STM image of ~ 2 ML of Pd deposited at $300\text{ }^{\circ}\text{C}$. $1500 \times 1500\text{ }^{\text{Å}}^2$, $U_s = 2.1\text{ V}$, $I_t = 1.8\text{ nA}$. (b) Line scan along the indicated line in (a).

ing. This has, however, not been pursued. For Pd deposition above $600\text{ }^{\circ}\text{C}$ all material penetrates through the film, leaving an almost clean film behind.

To relate the observed changes to the Pd amount on the surface, AES was obtained for Pd deposited at different sample temperatures. This is shown in Fig. 4.26(c). The Al, Ni and O peaks are unaffected by the increasing temperature, whereas a clear decrease in the Pd signal is observed. This is exemplified by the size of the Pd(MNN) peak in the lower right corner.

Due to the large difference in formation enthalpy of PdO (85 kJ/mol) and Al_2O_3 (1653 kJ/mol) [89], it is more likely that Pd deposited at high temperatures is incorporated into the film rather than reducing the Al_2O_3 to form PdO. The clusters which are incorporated into the film are situated at the domain boundaries and at step edges, but the extent of the incorporated clusters is larger than the extent of the domain boundaries, and the incorporation is not just at the boundary zone but at the entire contact area. The shape change of the nanocrystals which is observed when Pd is deposited at elevated temperature, as shown in Fig. 4.26(b) where the aspect ratio is observed to have increased, can be explained by Pd incorporation into the film. The geometry of

the interface is completely altered, hence the adhesion energy also changes and therefore the height-to-width ratio. Another factor is strain. If the nanocrystal becomes strained due to the incorporation into the film, the height-to-width ratio also changes [97].

4.15 Pd nanocrystals in a high-pressure hydrogen ambient

Few experiments have been conducted on clusters in a high-pressure of hydrogen. The experiments presented in this section are basically test experiments which were conducted to explore the potential of a newly built high-pressure cell, and the amount of obtained data only allows for a few conclusions to be extracted.

4.15.1 The high-pressure cell

The high-pressure (HP) cell in which the high-pressure STM is situated is a unit attached to an ordinary UHV system. The sample is first cleaned and prepared in UHV and then placed in the cell with a manipulator and sealed off with a valve. The STM itself is in all major aspects identical to the STM design presented in section 1.3. It can operate in the entire range from UHV up to 1 atm. To avoid the pressure regime where discharges may occur [34], argon is added until the total pressure exceeds the problematic pressure regime between $\sim 10^{-3}$ and ~ 100 torr. The main concern of the high-pressure cell is the chemical reactivity of the surroundings and the cleanliness of the gas. To ensure chemical inertness the volume of the high-pressure cell is small ($V \approx 500$ ml) and all metal parts of the HP-STM, as well as the walls of the HP-cell, are electrochemically gold-plated. The present experiments were performed with 99.9997% purity H_2 gas used as delivered without further cleaning.

4.15.2 The structure of Pd nanocrystals under high pressure

It has not been possible to scan over the same area from UHV conditions up to a pressure of 1 atm. It turned out to be practically impossible to keep the tip stable for a long enough period of time.

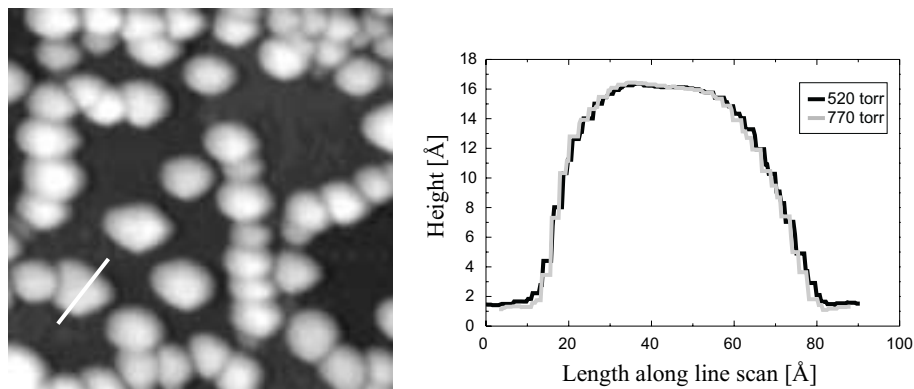


Figure 4.28: (a) STM image acquired in a background of 770 torr of hydrogen. $500 \times 500 \text{ \AA}^2$, $U_s = -0.9 \text{ V}$, $I_t = -0.4 \text{ nA}$. (b) Line scan along the indicated line in (a) both on the image presented and on an image of the same area, but acquired at a background pressure of 520 torr of hydrogen.

An image of 2 ML of Pd on the Al_2O_3 film in 770 torr of hydrogen is presented in Fig. 4.28(a). The image is acquired in a series of measurements where the pressure was gradually turned up, the starting pressure being 410 torr, ending at 770 torr. The time scale of such a measurement is 1 hour. Figure 4.28(b) shows two line scans obtained along the indicated line, of two different images of the same area obtained at different pressures. The result can be interpreted in two ways, either the cluster shape is stable under the hydrogen ambient (for at least one hour) or a shape change has occurred with respect to the UHV shape. This high-pressure shape is, however, pressure independent in the regime 410 to 770 torr.

Almost all *in-situ* studies of oxide-supported metal clusters in high-pressure are interesting as all industrial catalysts operate at high-pressures. It may not be possible to obtain atomic resolution, but it would also be extremely interesting to perform experiments to clarify possible shape changes, sintering and cluster diffusion in different gases, and maybe even while running a reaction.

4.16 Metals on Al₂O₃/NiAl(110)

Experiments have been conducted on many different metals dispersed on the Al₂O₃/NiAl(110) film, and STM images have been acquired of most systems. The bulk part of the STM work has concentrated on cobalt, rhodium and palladium (see e.g. [25, 52]).

The nucleation behaviour of all the studied metals seems to be dominated by the defects of the film [25, 68], i.e. all metals exhibit heterogeneous nucleation. All metals grow according to the Volmer-Weber growth mode, but the average particle size and morphology vary quite a lot. The variations are partly attributed to variations in the metal support interaction strength, which can be evaluated from the morphology of the deposits, i.e. the flatter the deposit, the stronger the interaction with the substrate. This can be understood from the discussion in section 4.3.3.

The metals studied by STM fall roughly in three groups according to the growth behavior at RT: The first group contains only Ag [98]. Of all metals studied up to now Ag interacts the weakest with the Al₂O₃ film. Silver forms very large clusters which nucleate at the step edges. The second group consists of: Cu, Pd [27, 68], Rh [65, 68, 85, 99] and possibly Au [100]. These metals nucleate almost exclusively at step edges and at the domain boundaries, and (exclusive Au) are the only metals which have been observed to spontaneously form nanocrystals. The third group contains: Co [25, 65, 68], Pt [86, 101], Al [102], Ir [68] and V [73]. These metals nucleate at point defects on the oxide domains, and do not, or only weakly, seem to prefer nucleation at domain boundaries and step edges. Also bimetallic clusters of Co-Pd have been prepared and imaged with the STM [103].

The growth behaviour of the various metals can be roughly correlated with the formation enthalpy of the respective metal oxide compounds: M_xO_y. Only Pt deviates substantially from what is expected from the formation enthalpy of PtO₂, which is similar to the formation enthalpies of PdO and RhO [15, 52]. It is not understood why Pt falls out of line compared to Rh and Pd.

In Fig. 4.29 two STM images are presented to illustrate how the overall structure of a metal, which interacts strongly with the oxide film differs from the overall structure of a weakly interacting metal. The two images are low coverage images with the approximately same coverage of Pt in (a) and Cu in (b). The deposition has in both cases been performed at RT. The Cu clusters at first sight seem to be much larger than the Pt clusters, but this is due to the electronic effects discussed in section 4.8, that clusters scanned at low bias

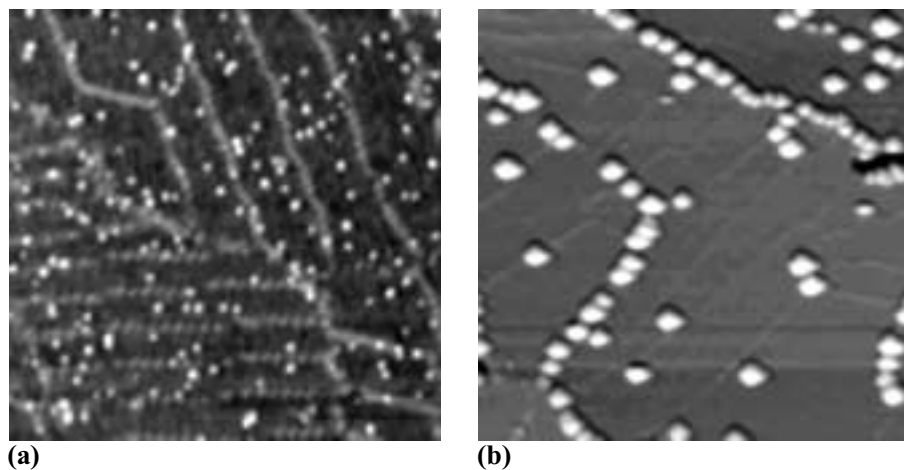


Figure 4.29: (a) Pt deposited onto the Al₂O₃ film at RT. $1000 \times 1000 \text{ \AA}^2$, $U_s = 3.5 \text{ V}$, $I_t = 0.7 \text{ nA}$. (b) Cu deposited onto the Al₂O₃ film at RT. $1000 \times 1000 \text{ \AA}^2$, $U_s = 1.1 \text{ V}$, $I_t = 0.6 \text{ nA}$.

appear $\sim 5 \text{ \AA}$ larger than they are. The Cu clusters are actually only slightly larger than the Pt clusters. The Pt clusters are dispersed more or less randomly on the surface without preference for nucleation at the domain boundaries (or steps). This is in contrast to Cu, which has nucleated exclusively along steps and domain boundaries. As in the case of Pd, the distribution of Cu clusters is determined by the distribution of the underlying domain boundaries. The Pt image contains ~ 160 clusters, whereas the Cu image contains ~ 80 clusters, thus the number density of (a) is twice that of (b).

Atomic resolution on Cu nanocrystals have also been obtained (this is described in more details in Ref. [IV]). The atomic arrangement of both the Pd and Cu top facets are hexagonally close-packed, as shown in the inset in Fig. 4.30 along with an overview image showing the cluster shape. The nanocrystal shapes of Pd and Cu are different, as the side length ratio of Cu is: $s = 1.0 \pm 0.1$, and the height-to-width ratio for larger nanocrystals is: $h/w = 0.4 \pm 0.1$. The smaller Cu nanocrystals exhibited a variation of the h/w ratio with the size of the top facet, similar to the situation for Pd. From an analysis identical to the one of the Pd nanocrystals, an adhesion energy of

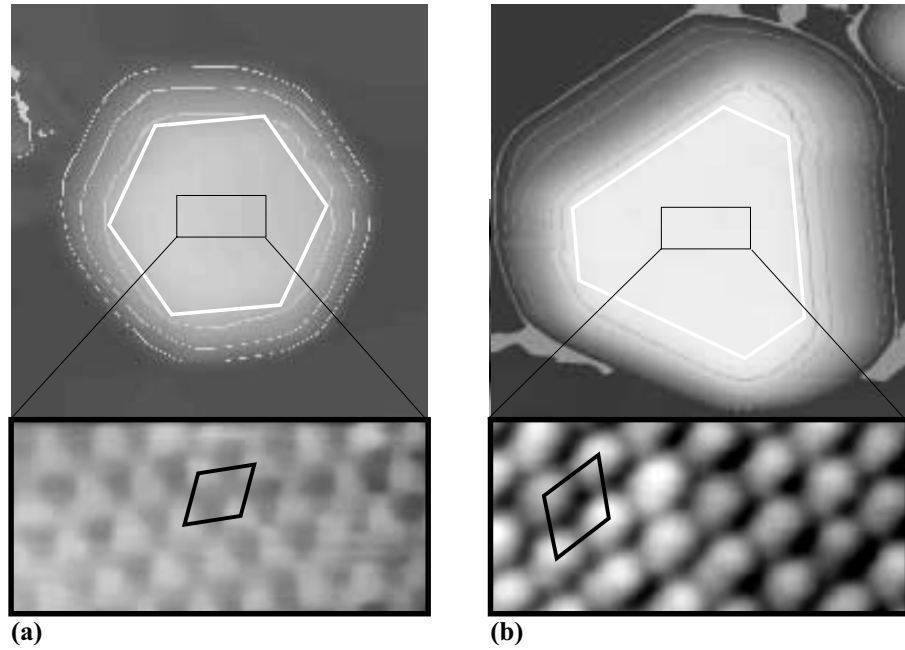


Figure 4.30: Two STM images of hexagonal metal clusters on an Al_2O_3 film. (a) $90 \times 90 \text{ \AA}^2$ image of a Cu nanocrystal. Solid white line indicates a regular hexagon. Inset is a $20 \times 9 \text{ \AA}^2$ image showing atomic resolution. (b) $150 \times 150 \text{ \AA}^2$ image of a Pd nanocrystal. Solid white line indicates a hexagon with a side length ratio: $s = 0.4$. Inset is a $18 \times 9 \text{ \AA}^2$ image showing atomic resolution. The apparent difference in slopes of equivalent sides of the Pd cluster is an artifact due to broadening from an asymmetric tip. None of the insets are from the shown clusters.

$\text{Cu}/\text{Al}_2\text{O}_3/\text{NiAl}(110)$ was found: $W_{\text{adh}} = 2.8 \pm 0.2 \text{ J/m}^2$. This is very close to the adhesion energy found for Pd. This is purely accidental, as the value of W_{adh} is derived from an interplay between geometrical parameters and surface energies.

4.17 Conclusion

The main part of this chapter has dealt with the Pd nanocrystals which appear spontaneously for deposition at RT. It was shown that a clear bias dependence on the measured cluster height exists. The apparent height of the Pd clusters decreases by 5 Å in the bias interval from +2 V to +4 V and is independent of bias voltage outside this range. A similar effect could be observed for metal clusters on thin insulating films grown on conducting substrates in general. If not taken properly into account, the effect could seriously distort, e.g., the results of size distribution measurements of metal clusters. Atomic resolution has been demonstrated on clusters with a diameter above ≈ 40 Å, allowing a crystallographic identification of the cluster facets. It was found that virtually all nanocrystals were non-planar. This is not readily understood, but possible explanations were discussed. The nanocrystals were found to possess their equilibrium shape which allowed the extraction of the adhesion energy from a detailed comparison between the observed shape of the clusters and that resulting from a Wulff construction based on calculated surface energies. For Pd on Al₂O₃ we have obtained a value of $W_{\text{adh}} = 3.1 \pm 0.2$ J/m². It was then shown that even a moderate increase in the deposition temperature to $T > 100$ °C had a drastic effect on the obtained cluster shape, partly related to the incorporation of Pd in the thin oxide film. Preliminary high-pressure experiments were briefly discussed, and it was shown that the shape of the Pd nanocrystals is stable under a high pressure of hydrogen. Finally, different metals on the Al₂O₃/NiAl(110) film were discussed, where atomic resolution on Cu nanocrystals was also demonstrated.

Adsorption of oxygen on Pd(111) and on Pd nanocrystals

In this and the following chapter adsorption of simple molecules on the nanocrystals is discussed. Atomically resolved adsorption (and reaction) studies on nanosize transition-metal clusters are potentially very interesting, in order to access direct insight at the atomic-scale into a possible influence, on adsorbate structure and reaction rates from the reduced size of the metal. For example, to what extent does the presence of edges and corners influence an overlayer? Is it possible to detect communication between different facets, or even between the cluster and the substrate?

The main topic in this chapter is a discussion of atomically resolved images of oxygen adsorbed on the Pd nanocrystals. Palladium is well known as an efficient catalyst for oxidizing hydrocarbons and carbon monoxide, which is the reason why palladium may be used in the automotive exhaust catalyst. The dissociative adsorption of oxygen is the first step in these reactions and oxygen adsorption on Pd(111) surface have, partly for that reason, received considerable attention (most lately e.g. [104–106]). As a basis for interpretation of the STM data, a brief overview of oxygen adsorption on Pd(111) is provided in the beginning; then the imaging of oxygen on Pd(111) is discussed, mainly to support the findings on the nanocrystals, which are discussed in the rest of the chapter. The results presented in this chapter are intended to form the basis of a publication (Ref. [VI]).

5.1 Experimental details

The Pd(111) crystal is cleaned by cycles of sputtering with 2 keV neon ions for 10 to 15 minutes, and subsequent annealing to 900 K for 10 to 15 minutes. The cleanliness of the sample was controlled with the STM, and the surface was accepted to be clean if only a few point defects could be detected on a $\sim 1000 \times 1000 \text{ \AA}^2$ scale. Oxygen (99.999% pure) was introduced into the chamber via a leak valve up to pressures of 1×10^{-7} torr and the measurement was performed with oxygen present in the background.

5.2 Oxygen adsorption on Pd(111)

Oxygen adsorbs dissociatively above 200 K and desorbs associatively at 780 K [107]. At RT a p(2×2) overlayer with a coverage of 0.25 ML is developed, which saturates after a dose of 30 L. At saturation the sticking probability drops almost to zero [105,106]. Oxygen adsorbs into the threefold hollow sites of the Pd(111) surface. According to DFT calculations the FCC site is preferred [108,109], whereas a low-energy ion scattering experiment found that only the HCP site was consistent with the obtained data [104].

At low coverage, stable tunnel conditions could not be obtained when attempting to image isolated oxygen atoms, or clusters of oxygen atoms, but once a saturated overlayer was completed, a p(2×2) structure was readily imaged. This is ascribed to a high mobility of the oxygen atoms in an unsaturated overlayer. Oxygen is easily removed from the surface by small amounts of H₂ and CO [104–106], and we found that even trace amounts of H₂ or CO in the rest gas were sufficient to destabilize the oxygen overlayer. Stable imaging conditions could be obtained by maintaining a small background pressure of oxygen, and all experiments were performed in an oxygen pressure between 5×10^{-8} torr and 1×10^{-7} torr.

5.3 STM imaging of O/Pd(111)

In the case of oxygen on Pd(111) and nanocrystals, the character of the tip is of utmost importance for the obtained STM images. To illustrate the strong dependence a series of images is presented in Fig. 5.1.

The images in Fig. 5.1 are acquired in an oxygen pressure of 5×10^{-8} torr. The images have been obtained in time intervals of approximately 15 minutes and are all $70 \times 70 \text{ \AA}^2$ in size. The image in Fig. 5.1(a) was recorded a few minutes after the oxygen was leaked into the chamber. A saturated overlayer has not yet built up and only bright glitches can be observed on top of the Pd(111) surface. These are ascribed to oxygen atoms diffusing in and out of the tunnel region. In Fig. 5.1(b) a saturated p(2×2) overlayer has built up, which is readily imaged.

A very important point is that for getting from (b) to (c) the tip is deliberately indented into the surface. This usually only has the effect of either improving or destroying the resolution, but in the case of oxygen on Pd(111) it is possible to shift from imaging the (2×2) symmetry of the overlayer to a

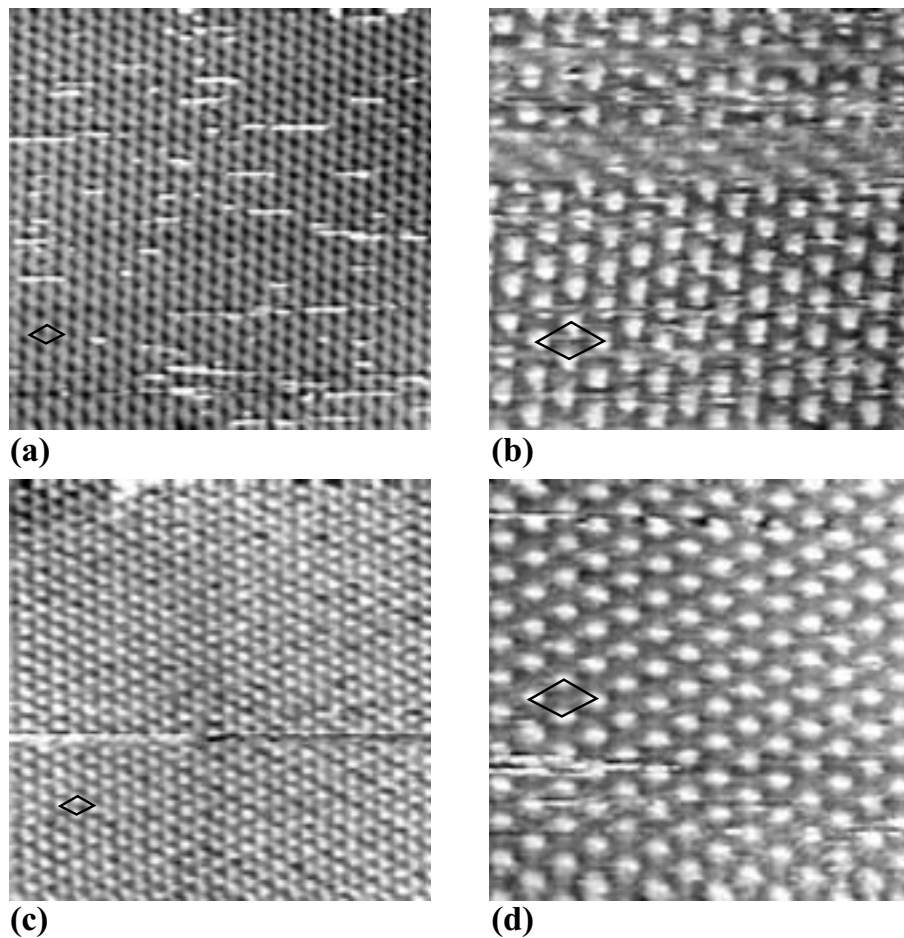


Figure 5.1: STM images of Pd(111) obtained in an oxygen pressure of 5×10^{-8} torr. Images were acquired successively with ca. 15 minutes in between. (1×1) and (2×2) unit cells are indicated. (a) Image of Pd(111) right after the oxygen was leaked into the chamber. $70 \times 70 \text{ \AA}^2$, $U_s = -11.8 \text{ mV}$, $I_t = -1.8 \text{ nA}$. (b) $p(2 \times 2)$ oxygen overlayer. $70 \times 70 \text{ \AA}^2$, $U_s = -6.8 \text{ mV}$, $I_t = -1.2 \text{ nA}$. (c) After the tip has been indented into the surface, showing a (1×1) periodicity. $70 \times 70 \text{ \AA}^2$, $U_s = -0.6 \text{ mV}$, $I_t = -1.4 \text{ nA}$. (d) After the tip has been indented into the surface, re-exhibiting the (2×2) periodicity. $70 \times 70 \text{ \AA}^2$, $U_s = -0.6 \text{ mV}$, $I_t = -2.1 \text{ nA}$.

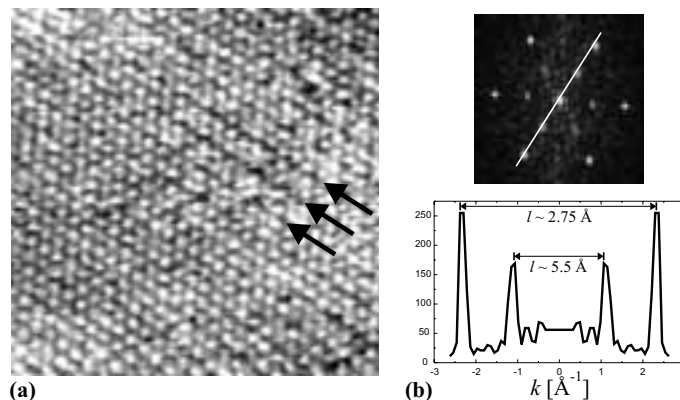


Figure 5.2: (a) STM images of Pd(111) obtained in an oxygen pressure of 5×10^{-8} torr. Arrows indicate double periodicity. $70 \times 70 \text{ \AA}^2$, $U_s = -8.2 \text{ mV}$, $I_t = -1.5 \text{ nA}$. (b) Fourier transform of the image in (a), and a line scan along the indicated line.

(1×1) periodicity, presumably of the substrate. The indentation of the tip into the surface may have to be repeated a few times to make the shift. In order to obtain the image in Fig. 5.1(d) the tip has again been indented into the surface, resulting in a re-appearance of the (2×2) periodicity.

The interpretation of why Fig. 5.1(c) suddenly shows (1×1) periodicity, and (d) (2×2) periodicity, is that depending upon the tip characteristics, i.e. the shape, and maybe more importantly whether oxygen has been incorporated into the tip apex, either the symmetry of the underlying substrate or the symmetry of the overlayer is probed. The same effect is also present for oxygen adsorption on the (111) top facet of the nanocrystals (see section 5.5).

According to STM image simulation oxygen is expected to be imaged as a depression on Pd(111) [37]. This is not the case for the images presented in Figs. 5.1(b) and (d), the reason for this being inverse corrugation effect (see section 1.4).

On images where the (1×1) substrate periodicity predominates, also the (2×2) periodicity may be present. An example is given in Fig. 5.2. The (2×2) periodicity can be seen by Fourier transforming the image as shown in (b). Two sets of spots are present, one set corresponding to the lattice periodicity, and the other corresponding to the overlayer periodicity. A closer look at the

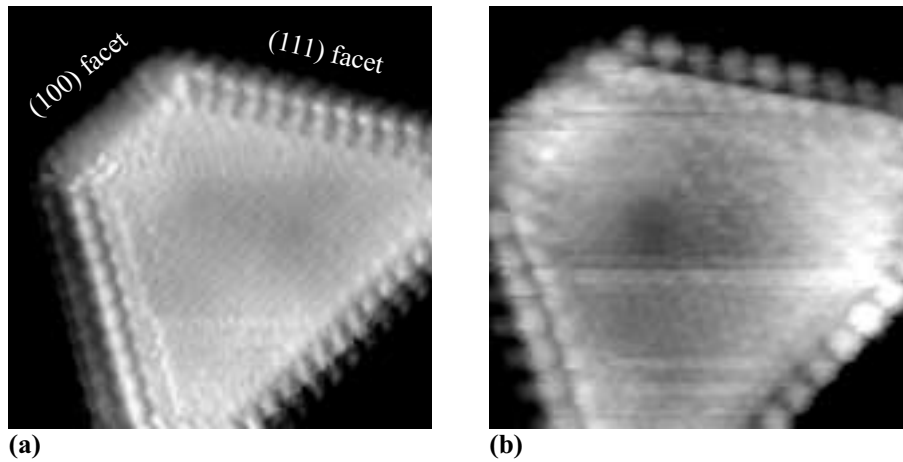


Figure 5.3: STM images of the same clusters in an oxygen pressure of 5×10^{-8} torr. (a) Total exposure less than 1 L, $100 \times 100 \text{ \AA}^2$, $U_s = 1.1 \text{ V}$, $I_t = 1.2 \text{ nA}$. (b) Total exposure $\sim 175 \text{ L}$, $70 \times 70 \text{ \AA}^2$, $U_s = -3.1 \text{ mV}$, $I_t = -1.1 \text{ nA}$.

STM image reveals, also in real space, the double periodicity. This is indicated with the arrows on the image in (a).

The imaging of oxygen on palladium is in a sense similar to the imaging of waves on NiAl. Changing the character of the tip makes imaging of different characters of the system possible: atoms vs. waves \leftrightarrow (1×1) periodicity vs. (2×2) periodicity, and even both characters in a superposition.

5.4 Adsorption of oxygen on Pd nanocrystals

We now shift to the Pd nanocrystals. When oxygen is introduced into the chamber, a clear effect on the Pd clusters is immediately observed. An example is given in Fig. 5.3. The cluster in (a) was exposed to only $\sim 1 \text{ L}$ of oxygen, whereas the cluster in (b) was exposed to $\sim 175 \text{ L}$ of oxygen. In the figures, clear protrusions along the (111) edges are observed, whereas the top facet appears to be unaffected. The (100) edges also appear unaffected by the presence of oxygen, but this is due to the loss of resolution at these edges. Few examples exist where the cluster exhibits a double periodicity along the (100) edges. Here

we concentrate on the (111) edges.

The oxygen dose in Fig. 5.3(a) is only ~ 1 L, and it may be that the dose is too small for a $p(2\times 2)$ overlayer to build up on the top facet. It is expected from d -band theory that the edges are influenced first by the presence of oxygen [109,110]. Palladium atoms at the edge will have a higher d -band center because of a lower metal coordination. A major result from d -band theory is that if everything else is equal then the higher the d -band center, the stronger the binding. Consequently, if an adsorbate prefers absorption in a specific site (e.g. threefold hollow), it would rather bind at such a site next to the edge of a cluster than at the facet of a cluster. In (b) the same cluster has been exposed to ~ 175 L; it will be shown below that this dose is sufficient to saturate the (111) top facet. The apparent lack of oxygen on the top facet is not an effect of insufficient exposure. The edges are special, but first oxygen on the top facet will be discussed.

5.5 Oxygen on the top facet

Oxygen adsorption on the (111) top facet of the nanocrystals leads to the formation of a $p(2\times 2)$ overlayer just as in the case of O/Pd(111). An example is given in Fig. 5.4. In (a) a (111) edge is shown, and it can be seen that the (2×2) overlayer extends all the way to the edge. The overlayer structure is little affected by the edge. In (b) a 3D image of the same cluster is shown. In the 3D view it can be seen that the resolution has been maintained two layers down on the side facet. The side facet protrusions fall between two edge protrusions. This indicates that a (2×2) overlayer is present also on the side facet. The type of overlayer, and hence the type of facet cannot be extracted from just one row of protrusions. A $p(2\times 2)$ overlayer, also on the side facets is, however, consistent with the findings on the clean clusters – that the large side facets are (111) facets.

If scanned in an oxygen background, the clusters usually appear like the one in Fig. 5.3, i.e. showing clear protrusions along the edges and apparently nothing on the top facet. On the oxygen-covered extended Pd surface it was possible to shift between imaging the symmetry of the substrate and that of the overlayer by changing the tip character. On the clusters, it is not easy to change the state of the tip, as in most cases the tip will drop so much material that the cluster will be almost covered with it (see e.g. Fig. 1.3). In few cases it has been possible to have only a small tip change without covering the entire

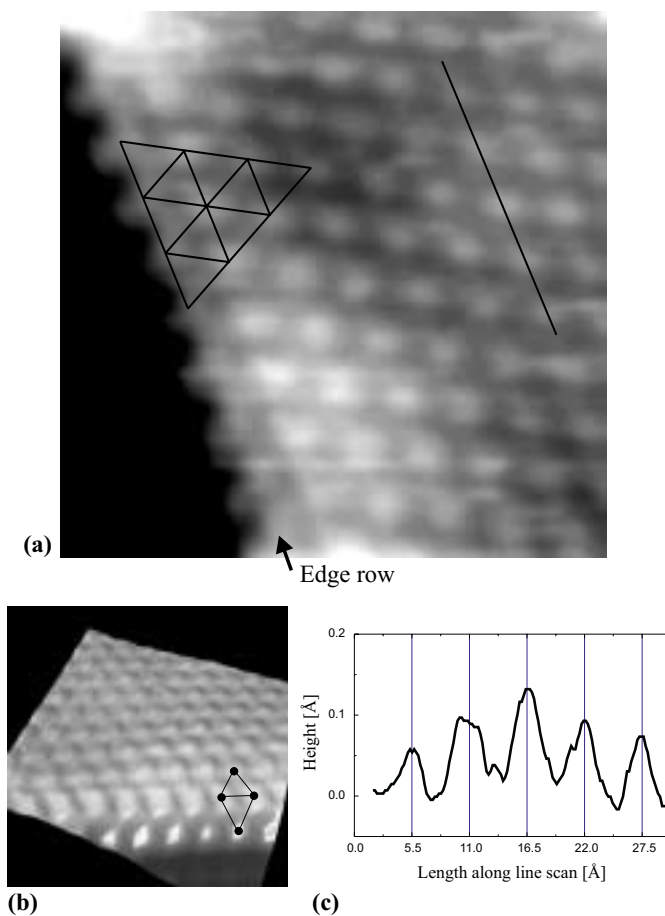


Figure 5.4: STM image showing the $p(2 \times 2)$ oxygen overlayer, the image was acquired in an oxygen pressure of 1×10^{-7} torr. (a) $50 \times 50 \text{ \AA}^2$, $U_s = 17 \text{ V}$, $I_t = 1.5 \text{ nA}$. (b) 3D view of (a) showing the registry of the second-to-next top layer. Dots indicate oxygen protrusions consistent with a $p(2 \times 2)$ overlayer. (c) Line scan along the indicated line in (a).

cluster. These changes were in some cases intentionally induced by applying small voltage or current pulses, but normally the tip crashed by itself after a certain amount of time. These tip changes have led to tunnel conditions making it possible to image the p(2×2) overlayer.

As the shifting between imaging of a (1×1) and (2×2) overlayer is atypical, two examples showing the shift on the same cluster are presented in Fig. 5.5 and 5.6. Figure 5.5 shows three images of the same cluster obtained within 10 minutes in an oxygen background of 5×10^{-8} torr. The cluster in (a) appears similar to the cluster in Fig. 5.3, except that atomic resolution of the top facet has been obtained and a fairly clear (1×1) periodicity can be seen. Two line scans, one along a close-packed Pd row on the top facet and one along the edge, are presented in (d), showing that the edge protrusions are spaced with a double periodicity. The image resolution in (a) is not too good. In order to improve the resolution small tip changes have been invoked. The result is shown in (b), where the tip has dropped a small amount of material on the cluster. By zooming in on the unaffected part, a clear (2×2) periodicity is observed, as shown in (c).

Figure 5.6 is the second example. Again the background pressure is 5×10^{-8} torr. On the cluster in Fig. 5.6(a), a (1×1) periodicity is again observed on the central part of the cluster. The edges of the cluster are quite fuzzy because of a blunt tip, but exhibit double periodicity. Figure 5.6(b) was obtained 10 minutes after the image in (a). The tip has changed character by dropping material on the cluster (the blob in the upper right side), and as in Fig. 5.5(c) the unaffected part now exhibits (2×2) periodicity.

Another important factor, which must be considered, is the influence of the tunnel parameters. The images presented in this chapter were acquired with such different bias voltage as -0.6 mV in Fig. 5.5(a) to 46 mV in Fig. 5.10. From the image in Fig. 5.1(d) on Pd(111), it is shown that even with such low bias voltage as 0.6 mV it is possible to image the (2×2) oxygen overlayer. No correlation between the tunnel conditions and the appearance of the oxygen covered clusters can be established. It is, however, easier to keep the tip stable while imaging the p(2×2) overlayer with bias voltages larger than ~ 10 mV (undoubtedly because the tip distance to the surface is longer).

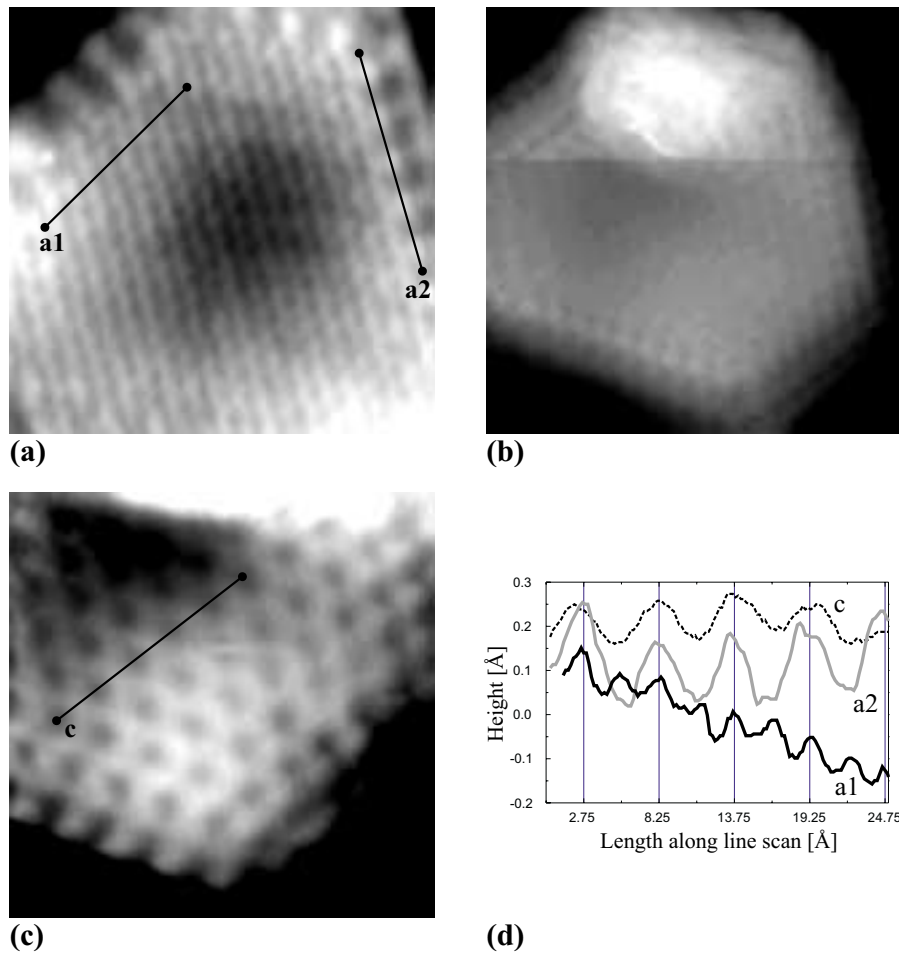


Figure 5.5: STM images showing the (1×1) to (2×2) periodicity transition in connection with a tip change. Images were acquired in an oxygen pressure of 5×10^{-8} torr. (a) $50 \times 50 \text{ \AA}^2$, $U_s = -0.6 \text{ mV}$, $I_t = -1.5 \text{ nA}$, the total exposure is 380 L. (b) $100 \times 100 \text{ \AA}^2$, $U_s = 39 \text{ mV}$, $I_t = 0.7 \text{ nA}$, the total exposure is 395 L. (c) $50 \times 50 \text{ \AA}^2$, $U_s = -28 \text{ mV}$, $I_t = -1.3 \text{ nA}$, the total exposure is 405 L. (d) Line scans along the indicated lines.

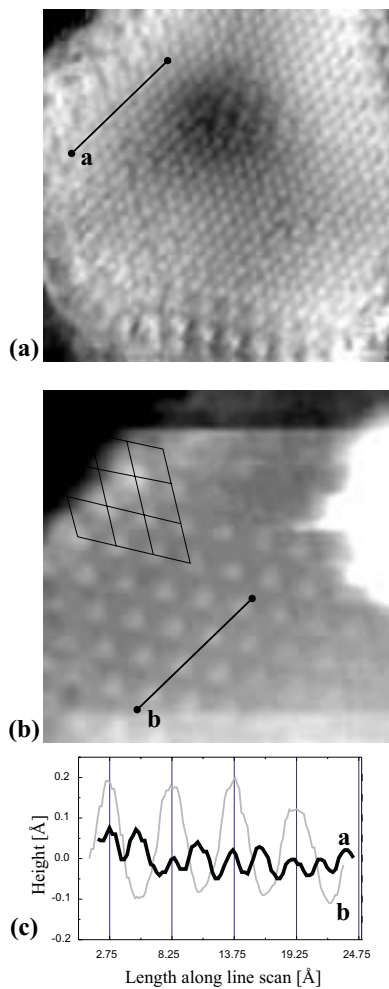


Figure 5.6: STM images showing the (1×1) to (2×2) periodicity transition in connection with a tip change. The images were acquired in an oxygen pressure of 5×10^{-8} torr. (a) $70 \times 70 \text{ \AA}^2$, $U_s = -1.5 \text{ mV}$, $I_t = -1.1 \text{ nA}$, the total exposure is 36 L. (b) $50 \times 50 \text{ \AA}^2$, $U_s = -3.1 \text{ mV}$, $I_t = -1.3 \text{ nA}$, the total exposure is 66 L. (c) Line scans along the indicated lines.

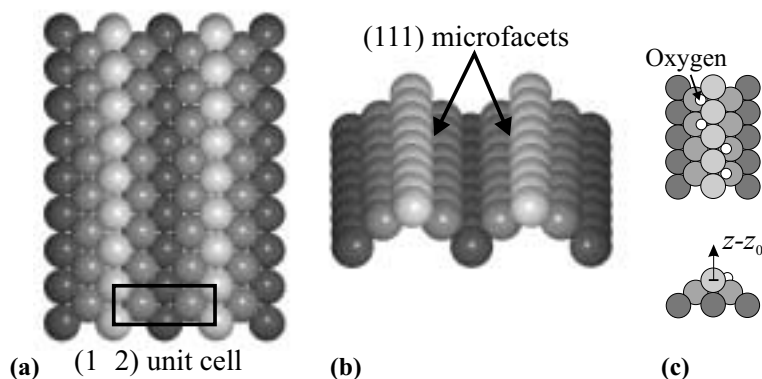


Figure 5.7: Ball model of the (1×2) missing row FCC(110) reconstruction. (a) Top view, (b) inclined view and (c) oxygen configuration on Pt, from [111].

5.6 The edge atoms

In this section we focus on the (111) edges, i.e. the transition from the (111) top facet to the (111) side facet. At the edges the binding properties deviate significantly from the (111) facets due to the reduced coordination of the Pd atoms. The edge resembles geometrically a ridge on the (1×2) missing row reconstructed FCC(110) surface. Recently, a combined STM and DFT study provided new insight into adsorption of oxygen on such a surface [111]. This is the inspiration of the model presented of the O/Pd-edges, and we therefore present a short summary of the O/Pt(110)- (1×2) missing row reconstruction [111].

In Figs. 5.7(a) and (b) top and inclined views of the (1×2) missing row reconstruction of an FCC(110) surface are shown. The surface consists of adjacent (111) microfacets meeting in a single row of atoms (the ridge). The ridge atoms mimic the edge atoms along the (111) edge on the nanocrystals, as both systems possess a row of atoms situated between two (111) facets.

In the case of oxygen adsorption on the missing row Pt(110)- (1×2) surface it was found that oxygen atoms could be adsorbed in several configurations in the threefold hollow sites along the ridge. An example of an oxygen configuration is shown in Fig. 5.7(c). The oxygen induced a relaxation of the surface. The Pt ridge atoms were pushed outwards and the protrusions observed in the STM images were actually the displaced Pt atoms [111]. The explanation why Pt

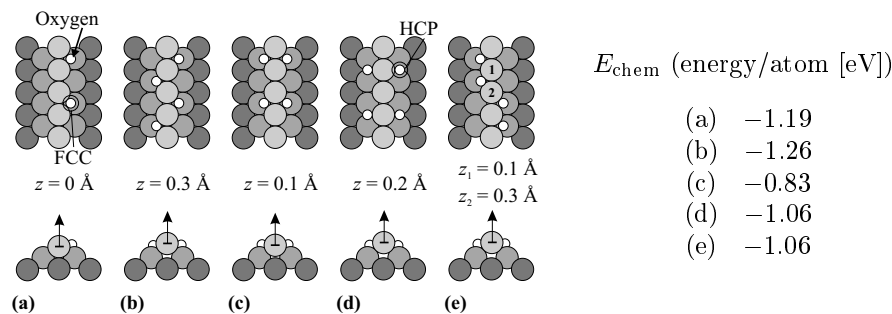


Figure 5.8: DFT calculations of different oxygen configurations on the (1×2) missing row reconstruction of Pd(110). The table shows average chemisorption energies per oxygen atom. Calculations by Ž. Šljivančanin, using the GGA-PW91 functional.

ridge atoms are lifted out, is based on the d -band model. By lifting the Pt atoms the effective coordination is lowered, which results in an upshift of the d -band center. The higher the atom is lifted, the stronger the oxygen atom is bound to the threefold hollow site. Combining the adsorption energy gain from lifting the ridge atom and the energy cost of the deformation, a new position of the Pt ridge atoms is found further outwards than the equilibrium position.

In the case of oxygen adsorption on Pd(110) experimental studies have been performed with ARUPS, LEED and STM [112–115]. Pd(110) does not spontaneously form a missing row reconstruction if sputtered and annealed in UHV, as Pt(110) does. Exposing the Pd(110) surface to oxygen while annealing, different missing row reconstructions can, however, be produced e.g. the (1×2) and (1×3) missing row reconstructions. In these experiments a double periodicity along the ridge rows was also found. A detailed atomistic picture has, however, not been established.

To clarify the adsorption behaviour of oxygen on nanocrystal edges, DFT model calculations of oxygen on the missing row reconstruction of Pd(110) have been carried out by Ž. Šljivančanin. Five different oxygen configurations were calculated and are presented in Fig. 5.8. The configurations in (a) and (b) are energetically the most stable structures, while the configuration in (c) is the least stable structure. The experiments are acquired in a background pressure, and the structure in (a) will therefore quickly be replaced by the structure in (b) which corresponds to a higher coverage. The structure in (b) gives rise to a uniform lifting of the ridge atoms, whereas the structures in (d) and (e) lift every second ridge atom, resulting in a geometrical double periodicity.

5.7 Oxygen-induced edge structures

Returning now to the edge structures on the nanocrystals, it is interesting to notice that on the clusters presented in Figs. 5.9, 5.10, 5.11 and 5.12, four different edge structures are observed. All, however, exhibit double periodicity along the edge. We will go through all four clusters and propose an oxygen configuration which, at least tentatively, can explain the edge structures.

To explain the observed edge structures we will rely on the results presented above that a $p(2\times 2)$ oxygen overlayer structure is present on the top facet, and the reason why we do observe a (1×1) periodicity on the top facet is the tip character. For the oxygen configuration at the edge, we will adapt the DFT model calculations and for reasons of consistency assume the DFT site determination of oxygen on the (111) top facet, i.e. oxygen adsorbs in a threefold FCC hollow site [109].

We start out with the discussion of the edge configuration of the cluster presented in Fig. 5.9(a). A zoom of the indicated area is presented in (b), where a lattice has been placed in registry with the atoms on the facet and extended to the edge. The unit cell of the edge protrusions consists of peanut-shaped protrusions and a round clear depression. In (c) an atomic model is presented which tentatively accounts for the observed protrusions.

The oxygen overlayer is split in two parts: (i) The oxygen configuration at the edge, and (ii) a $p(2\times 2)$ overlayer on the (111) top facet. The oxygen configuration along the edge is assumed to be the lowest energy configuration found in the DFT model calculation, which is the zigzag configuration from Fig. 5.8(b). A $p(2\times 2)$ overlayer structure can be fixed at one of four inequivalent FCC threefold hollow sites (I to IV). It can now be understood why the model calculations only considered the very edge. To take the overlayer into account at least five rows on the top facet should be included. This is too large a task with the computer power available to us.

By fixing the overlayer at point I, a rectangular oxygen lattice is formed at the edge. The rectangular cell it proposed to be the origin of the rectangular configuration of the protrusions observed along the edge. From the lattice in (b), the exact position of the protrusions can be found. The outermost protrusions are situated between two edge atoms. In the model calculations presented in Fig. 5.8(b) all the ridge atoms are equally lifted 0.3 \AA outwards. We propose that this symmetry is broken by an interaction with the facet overlayer, which possesses a double periodicity. It seems reasonable that the origin of the protrusions is an oxygen-induced lifting of the edge atoms, but

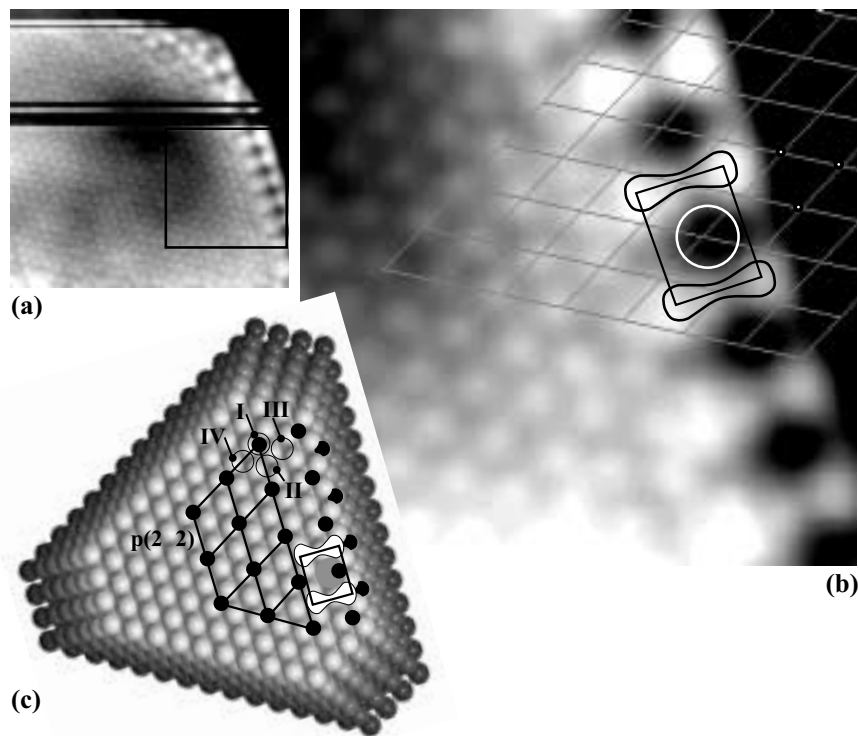


Figure 5.9: STM images showing (1×1) periodicity on the top facet and double periodicity along the edge. The image was acquired in an oxygen pressure of 5×10^{-8} torr. Total exposure is 65 L. (a) $70 \times 70 \text{ \AA}^2$, $U_s = -7 \text{ mV}$, $I_t = -1.3 \text{ nA}$. (b) Cut-out of (a), $30 \times 30 \text{ \AA}^2$ (c) Ball model of the proposed oxygen configuration. Solid black balls correspond to oxygen. Bright peanut shapes correspond to protrusions, and grey circle to area of depression.

in pairs, as indicated on the ball model in (c). The origin of the inner row of protrusions is unknown. It could again be a geometric effect, but as the protrusions are situated three rows away from the edge, it is more likely to be an electronic effect. The clear depressions in the center of the rectangular unit cell is situated more or less at the threefold hollow site occupied by oxygen. It was argued above that oxygen was not imaged in this mode, but the depressed areas are right at the cluster edge, and surely the tunnel conditions are influenced by that. Assuming that oxygen can, in fact, be imaged right at the edge, it fits very nicely with the fact that oxygen is imaged as a depression on Pd(111) [37].

The cluster in Fig. 5.10(a) is the second example with a clear (1×1) periodicity on the top facet and a double periodicity along the edge. As in Fig. 5.9, a zoom of the indicated area is presented in (b), and in (c) an atomic model is presented accounting for the observed protrusions. The symmetry of the edge protrusions is in this case triangular.

To explain the observed structure we follow the same procedure as above. The oxygen configuration along the edge is again taken as the lowest energy configuration found in the DFT model calculations presented in Fig. 5.8(b). In this case the overlayer structure is fixed at point II, and a triangular oxygen lattice is formed at the edge. The situation is similar to the one above, except from the positioning of the inner protrusion, which in this case is situated at a lattice position, one row further back on the cluster.

We now turn to the image presented in 5.11(a), which possesses only one row of protrusions, positioned at a lattice position. A $p(2 \times 2)$ overlayer structure is now fixed at point III. This results in oxygen from the facet overlayer being very closely spaced to the oxygen at the edge, which is energetically unfavorable. By displacing the outermost oxygen atoms in the facet overlayer from the FCC site to the neighboring HCP site and rearranging the edge structure such that the configuration (c) in Fig. 5.8 is obtained, a less dense configuration is obtained at the edge. This rearrangement assumes that the energy cost of adsorption in HCP sites is less than the energy gain from the less dense phase.

The edge configuration results in a situation where every second Pd edge atom is situated between two HCP-coordinated oxygen atoms. According to the DFT model calculations this results in a doubly spaced protruding row along the edge, which fits nicely with the fact that the edge protrusions are situated at Pd positions.

Finally, the image in 5.12(a) is discussed. The image is interesting as two edges are imaged on the same cluster. First we concentrate on the edge in the upper left corner. The observed protrusions are as in Fig. 5.9 peanut-shaped,

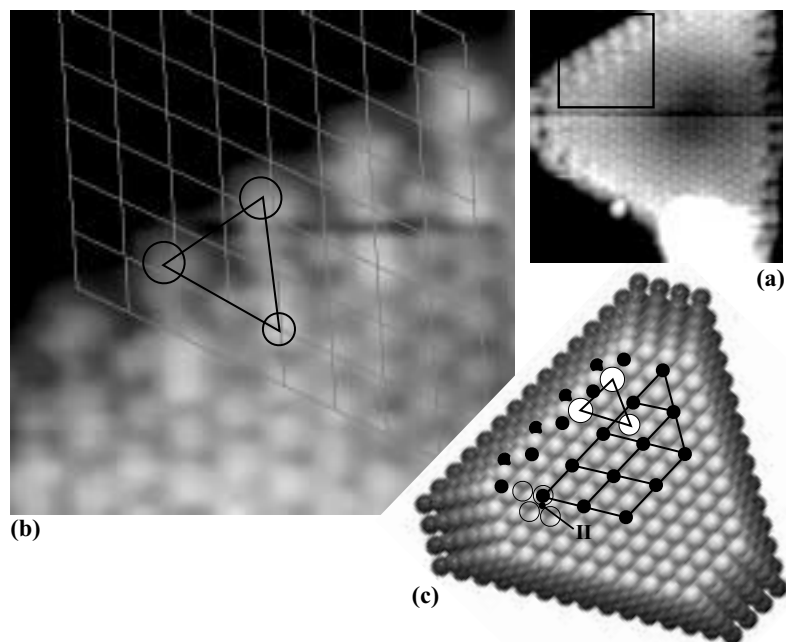


Figure 5.10: STM images showing (1×1) periodicity on the top facet and double periodicity along the edge. The image was acquired in an oxygen pressure of 1×10^{-7} torr. Total exposure is 15 L. A small tip crash has occurred on the cluster. (a) $70 \times 70 \text{ \AA}^2$, $U_s = 46 \text{ mV}$, $I_t = 0.9 \text{ nA}$. (b) Cut-out of (a), $30 \times 30 \text{ \AA}^2$. (c) Ball model of the proposed oxygen configuration. Solid black balls correspond to oxygen, white circles to protruding areas.

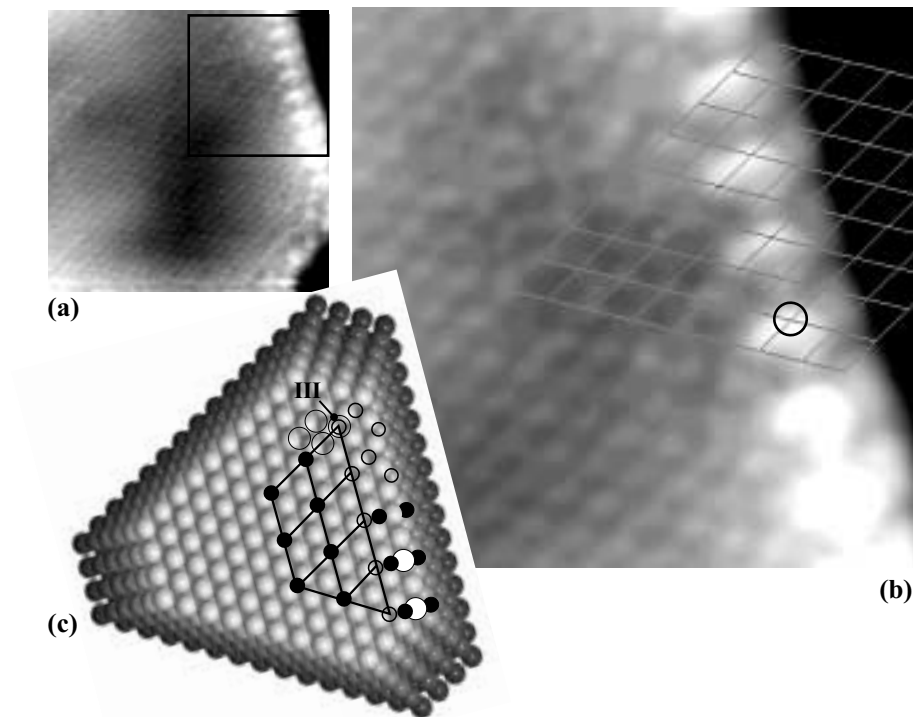


Figure 5.11: STM images showing (1×1) periodicity on the top facet and double periodicity along the edge. The image was acquired in an oxygen pressure of 5×10^{-7} torr. Total exposure is 50 L. (a) $70 \times 70 \text{ \AA}^2$, $U_s = 46 \text{ mV}$, $I_t = 0.9 \text{ nA}$. (b) Cut-out of (a), $30 \times 30 \text{ \AA}^2$ (c) Ball model of the proposed oxygen configuration. Solid black balls correspond to oxygen, open black circles correspond to FCC threefold hollow sites, white circles to lifted edge atoms.

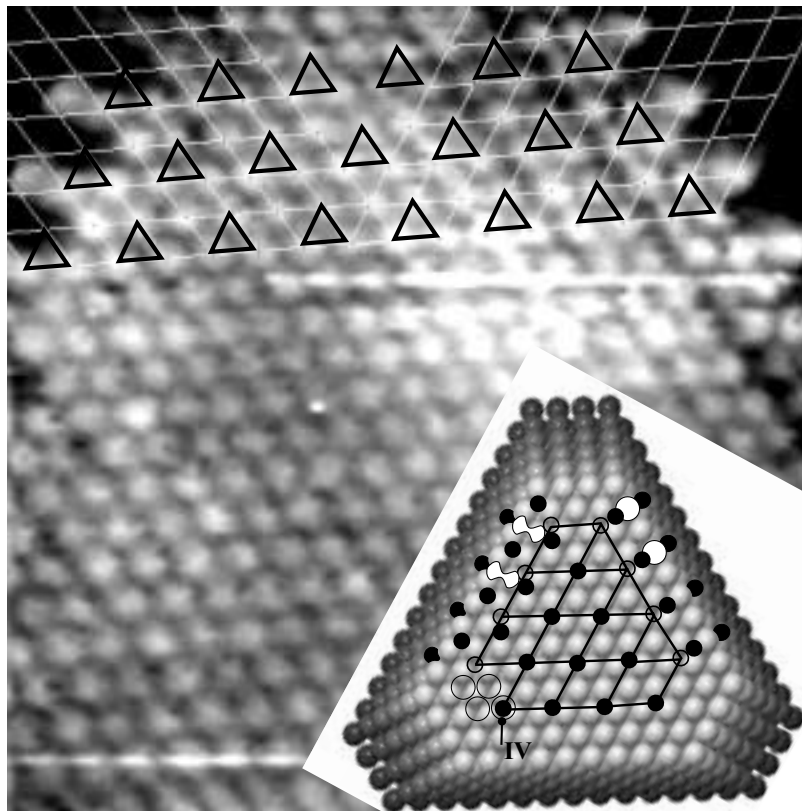


Figure 5.12: STM images showing (1×1) periodicity on the top facet and double periodicity along the edge. The image was acquired in an oxygen pressure of 1×10^{-7} torr. Total exposure is 600 L. $50\times 50 \text{ \AA}^2$, $U_s = -4 \text{ mV}$, $I_t = -1.2 \text{ nA}$. The black triangles indicate FCC positions. Inset: Ball model of the proposed oxygen configuration: Solid black balls correspond to oxygen, transparent black circles to FCC sites, white peanut shapes to areas which protrude.

but the distance between the two protrusions is in this case smaller.

Again the starting point is the zigzag edge structure. The $p(2 \times 2)$ overlayer structure is fixed at point IV. As in Fig. 5.11, the oxygen atoms from the facet lattice are very close to the edge oxygen atoms. In this case the edge structure is kept fixed, and the oxygen-oxygen distance is enlarged by moving the outermost row to a neighboring HCP site. The origin of the protruding outermost row of atoms is again proposed to be oxygen-induced lifting of Pd atoms. The second protruding row is here situated at the second most outer row. Thus, in this case it seems reasonable that also the origin of these protrusions is a geometrical effect, i.e. an oxygen-induced lifting.

The edge in the upper right corner is similar to the edge in Fig. 5.11, i.e. a single protruding row with the protrusions at lattice positions. Fixing the $p(2 \times 2)$ oxygen overlayer at the left edge makes it possible to extend the overlayer to the right edge, and it is seen that a configuration of the situation in Fig. 5.11 is obtained.

It has not been possible to find an atomic model, which could in detail account for the edge protrusions. The diversity in the observed edge structures does not suggest that a such model exists. The fact that different edge structures are found is not surprising as the clusters have different sizes, and the $p(2 \times 2)$ overlayer on the top facet will inevitably meet the edge in different ways. It is reasonable to assume that the outermost edge protrusions are related to an oxygen-induced lifting of the Pd edge atoms as suggested by the DFT model calculation. The protrusions on the facets have not been included in the model calculations and are not readily understood, but configurations of oxygen, which possess the symmetry of the observed structures, can readily be produced at the cluster edges. Whether the protrusions further away from the edge are due to a geometrical or electronic effect is uncertain. The depressions found are always situated near or at oxygen atoms suggesting that these are related to adsorbed oxygen which is expected to be imaged as a depression. This, however, seems to be opposed by the fact that the cluster lattice is resolved and hence the oxygen should not be imaged at all. As this is oxygen situated right at, or very near to, the edge, the tunneling situation is certainly different from that of oxygen on the central part of the cluster. A way of supporting the proposed model would be to obtain a large amount of images exhibiting clear atomic resolution on the top facet as well as two or three edges showing double periodicity (as Fig. 5.12) and test to what degree the edge structures can be correlated. This is, however, practically impossible due to the difficulties in these experiments.

5.8 Removal of oxygen

In section 5.2 it was mentioned that oxygen could be removed via reaction with small amounts of CO and H₂ in the background to form CO₂ or H₂O. In Fig. 5.13 four images are presented, which were acquired after the oxygen had been pumped out of the chamber. The images in (a) to (c) show the same cluster as in Fig. 5.4. The image in (d) is from a different cluster. The image in (a) is obtained 4 minutes after the oxygen has been pumped away, showing that the p(2×2) overlayer is still stable. The image in (b) has been obtained 10 minutes after the oxygen has been pumped away; at a point where the resolution is suddenly lost. After this point it was not possible to image a (2×2) overlayer anymore, however, images as presented in (c) could be obtained. This series of images indicates that oxygen is reacted away from the top facet first. One should, of course, be aware of the imaging problem with the (2×2) overlayer. The cluster presented in (d) was acquired approximately one hour after oxygen has been pumped away, and it shows that eventually oxygen is completely removed, leaving no trace at the cluster edges.

Oxygen uptake of palladium clusters residing on Al₂O₃/NiAl(110) has recently been addressed by Meusel *et al.* [116] in a combined molecular beam and STM study. They monitored the CO₂ production rate for the 2CO+O₂ reaction, where the palladium clusters were saturated with oxygen before CO was introduced into the chamber. Drastic changes in the CO₂ rate were observed when subsequent reaction cycles were performed. Only after approximately three cycles the reaction system became stable. It was found that the Pd clusters rapidly incorporate large amounts of oxygen, starting at sample temperatures just below RT. The oxygen uptake saturated only at stoichiometries of PdO_{>0.5}. In STM measurements neither the density nor the overall morphology of the Pd particles were found to be affected by the oxygen uptake; atomic resolution was, however, not obtained.

In the present study atomic resolution on clusters during and after oxygen exposure was obtained. Subsequent 2CO+O₂ reaction cycles were, however, not performed, but the oxygen impinging rate onto the surface was similar to the study by Meusel *et al.* Oxygen-induced edge structures were observed, but no overall morphological changes or lattice distortion on the top facet were found. It seems unlikely that a large amount of oxygen can be incorporated in the nanocrystal without having an observable effect on the top facet. One possible explanation is that subsequent CO₂ reactions are required for an appreciable oxygen uptake to take place. Another possibility is that oxygen is

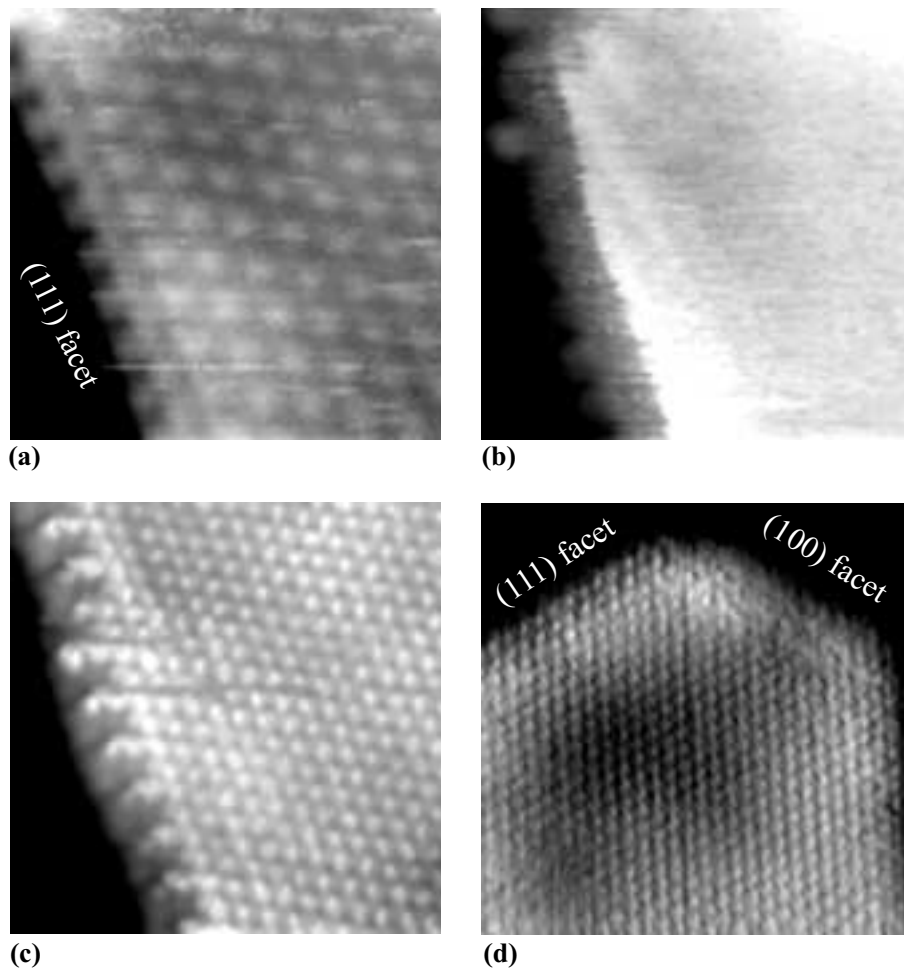


Figure 5.13: STM images acquired after oxygen has been pumped away. (a) After 4 minutes. $50 \times 50 \text{ \AA}^2$, $U_s = 17 \text{ mV}$, $I_t = 1.5 \text{ nA}$. (b) Same cluster as in (a) after 10 minutes. $50 \times 50 \text{ \AA}^2$, $U_s = 5 \text{ mV}$, $I_t = 1.5 \text{ nA}$. (c) Same cluster as in (a) after 19 minutes. $50 \times 50 \text{ \AA}^2$, $U_s = -0.6 \text{ mV}$, $I_t = -1.5 \text{ nA}$. (d) Cluster different from (a) to (c). After 1 hour. $70 \times 70 \text{ \AA}^2$, $U_s = -5 \text{ mV}$, $I_t = -1.6 \text{ nA}$.

incorporated in Pd clusters through kink sites, such that it is the unordered and/or smaller clusters which are responsible for the uptake and not the large, nearly perfect crystallites. The present experiments have, however, not been correlated with TPD measurements or other experiments which could reveal an uptake.

5.9 Conclusion

In this chapter the imaging of oxygen on both Pd(111) and on the top facet of the Pd nanocrystals has been discussed. It is found that the tip character has a strong influence on the images. It was shown on both the Pd(111) surface and the Pd nanocrystals that, depending on the tip character, it was possible to image either the symmetry of the substrate or the symmetry of the oxygen overlayer. A $p(2\times 2)$ overlayer builds up on the top facet of the nanocrystals, as on the extended Pd(111) surface. The $p(2\times 2)$ overlayer most likely extends down the (111) side facets. The presence of oxygen was found to have a clear influence on the edges. Different edge configurations were found, all exhibiting a double periodicity along the (111) edges on the clusters, but possessing different configurations of the observed protrusions. In order to explain the observed edge structures DFT calculations were performed to explore the most stable oxygen configuration right at the edge. By combining the DFT edge configuration with the different ways a $p(2\times 2)$ overlayer can meet the edge, a general model was proposed, which could tentatively explain the observed protrusions.

Finally, it was shown that oxygen could be removed by residual gas, most likely H_2 and CO. No overall morphological changes were found in connection with the oxygen exposures.

Adsorption of nitric oxide on Pd(111) and Pd nanocrystals

The fundamental steps in the reduction of NO by transition metal surfaces are of great practical importance as the reduction of NO is a key reaction in the automotive exhaust catalyst. Despite the important role of Pd in the automotive exhaust catalyst [9, 10], a complete understanding of the dense overlayers of NO on Pd(111) has not yet been established. STM images of NO on Pd(111) are not available in the literature, but three ordered structures of NO on Pd(111) have been reported. STM images along with DFT calculations of these three structures are presented in the first part of this chapter. The results are intended for publication (Ref. [V]). The last part of the chapter deals with the adsorption of NO on the Pd nanocrystals.

6.1 Experimental details

The Pd(111) crystal was cleaned as described in section 5.1. Nitric oxide (99.0% pure) was introduced into the chamber via a leak valve up to pressures of 5×10^{-5} torr, and the STM measurements were performed both with NO present in the background and with the NO predosed onto the sample. The STM images of NO/Pd(111) were recorded at both RT and in the temperature regime between 150 K and 200 K. Images of NO on the Pd nanocrystals were acquired only at RT.

6.2 Nitric oxide adsorption on Pd(111)

Four different overlayer structures of NO on Pd(111) have been reported in the literature where NO is adsorbed onto Pd(111) in the temperature regime between 100 K and 300 K. Three of the structures have been assigned to distinct desorption states, normally designated as α -, β - and γ -states. The γ -state cannot be correlated with any structure with long-range order, it has a coverage

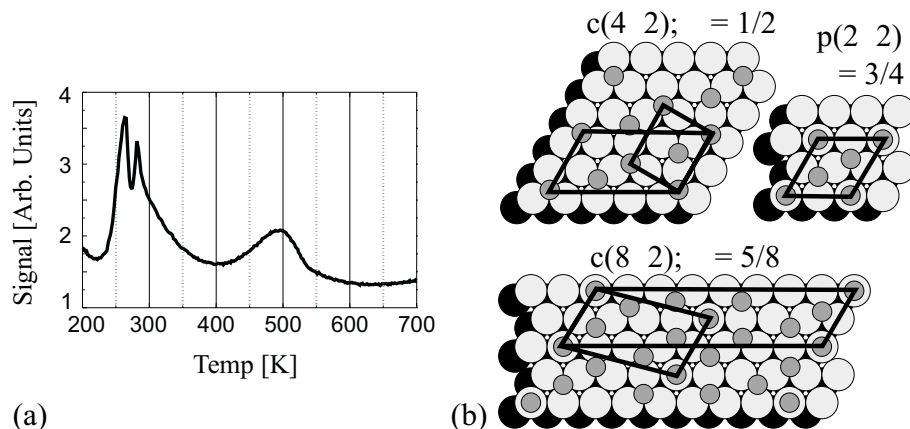


Figure 6.1: (a) TPD spectrum of NO/Pd(111), acquired after an NO background exposure of 1×10^{-6} torr with the sample at 150 K. (b) The three ordered structures of NO/Pd(111).

of $1/4$ ML and desorbs at 510 K [117,118]. The β -state has been correlated with a $c(4 \times 2)$ structure with a coverage of $1/2$ ML and desorbs at 285 K [117–119]. The α -state has been correlated with a $p(2 \times 2)$ structure with a coverage of $3/4$ ML and desorbs at 257 K [117–119]. The fourth structure has only been reported by Chen and Goodman [119] and was assigned to a $c(8 \times 2)$ structure with a coverage of $5/8$ ML. A TPD spectrum is shown in Fig. 6.1 with the three adsorption states assigned along with ball models showing the three ordered structures of NO/Pd(111). The spectrum is equivalent to earlier published spectra (see e.g. Refs. [117,119,120]).

Some discrepancies exist concerning the assignment of the adsorption site of NO in the ordered structures, e.g. the $c(4 \times 2)$ structure has been modeled by adsorption into bridge sites by Conrad *et al.*, Bertolo and Jacobi, and Chen and Goodman [117–119], but into atop sites by Wickham *et al.* [120], whereas a recent DFT study by Loffreda *et al.* points towards a mixed structure consisting of FCC and HCP threefold hollow sites [121]. The NO sites on Fig. 6.1(b) are those obtained from the DFT calculations, as found by Loffreda *et al.*, as well as B. Hammer and Ž. Šljivančanin (see section 6.4).

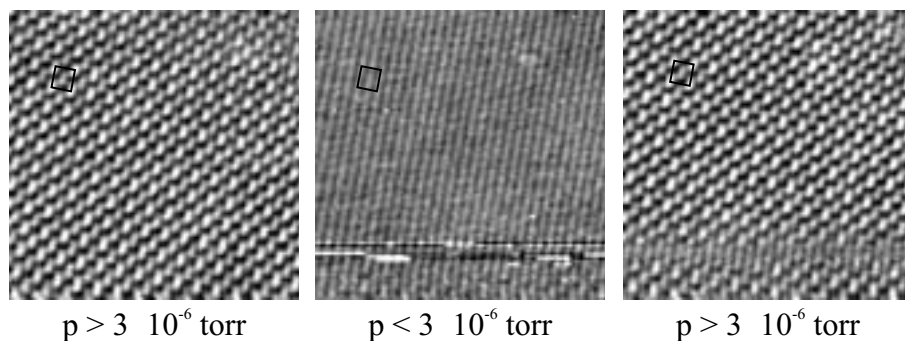


Figure 6.2: STM images of the $c(4\times 2)$ NO/Pd(111) structure acquired over the same area while the pressure is varied slightly around 3×10^{-6} torr. Rectangles indicate $c(4\times 2)$ unit cell. $70\times 70 \text{ \AA}^2$, $U_s = -4 \text{ mV}$, $I_t = -1.2 \text{ nA}$.

6.3 STM imaging of NO/Pd(111)

STM images were obtained at temperatures down to 150 K, but it was not possible to image single molecules or clusters of molecules before an almost saturated overlayer was built up. This is ascribed to a high mobility of the NO molecules in an unsaturated overlayer. Unfortunately this inhibits a clear site determination from the STM images, because in order to extract the adsorption site it would be necessary to determine the registry of the overlayer relative to the substrate.

6.3.1 Adsorption at room temperature

Adsorption of NO onto Pd(111) at room temperature leads to a competition between adsorption into the unstable $c(4\times 2)$ structure (β desorption state) and the unordered low density phase (γ desorption state). By maintaining a relatively high NO pressure the desorption rate from the ordered structure can be surpassed by the adsorption rate, thus stabilizing the $c(4\times 2)$ structure.

The transition between the unordered low density phase and the ordered $c(4\times 2)$ phase is rather sharp in terms of NO pressure and occurs at $\sim 3\times 10^{-6}$ torr. At pressures much lower than 3×10^{-6} torr only very noisy STM images were obtainable, which is ascribed to a high mobility of adsorbed NO molecules.

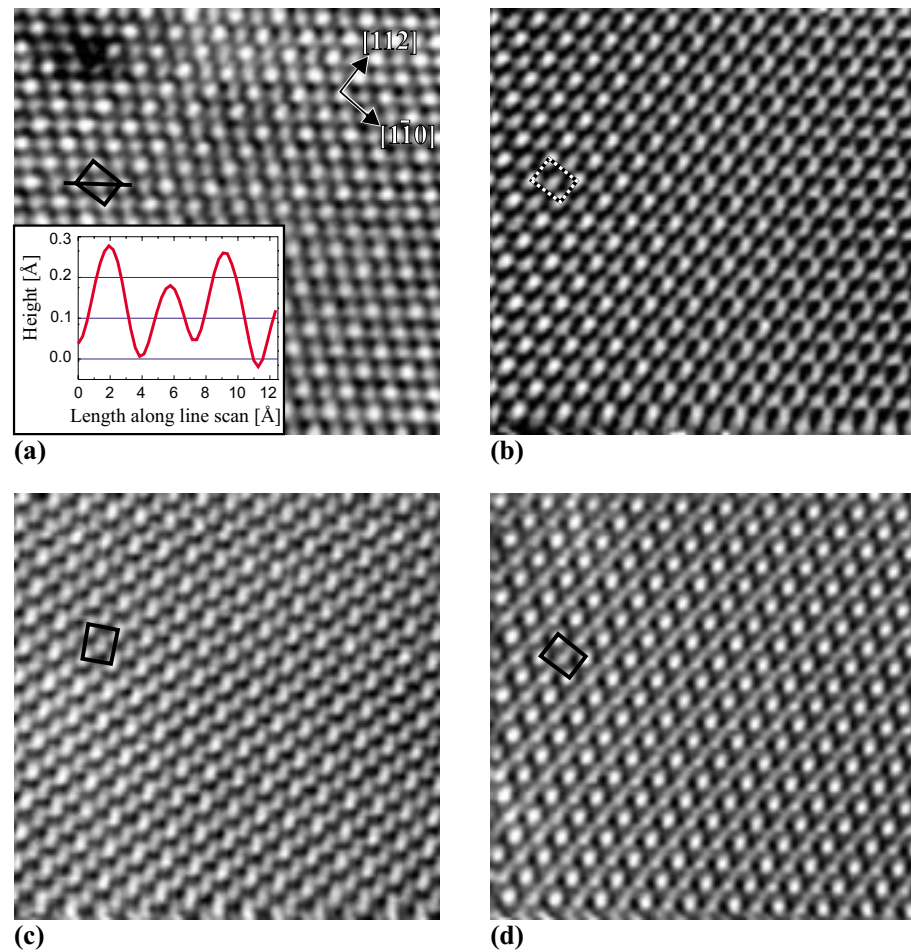


Figure 6.3: STM images of the $c(4 \times 2)$ NO/Pd(111) structure acquired in an NO pressure of 5×10^{-6} torr at room temperature. Rectangles indicate $c(4 \times 2)$ unit cell. (a) $70 \times 70 \text{ \AA}^2$, $U_s = -7 \text{ mV}$, $I_t = -1.5 \text{ nA}$. Inset: line scan along the unit cell diagonal. (b) $70 \times 70 \text{ \AA}^2$, $U_s = -20 \text{ mV}$, $I_t = -1.0 \text{ nA}$. (c) $70 \times 70 \text{ \AA}^2$, $U_s = -4 \text{ mV}$, $I_t = -1.2 \text{ nA}$. (d) $70 \times 70 \text{ \AA}^2$, $U_s = -3 \text{ mV}$, $I_t = -1.3 \text{ nA}$. The image in (c) was acquired in a different domain than the other images.

If the NO pressure is slightly below 3×10^{-6} torr a noisy $c(4 \times 2)$ is observed. As the pressure is raised above 3×10^{-6} torr the NO molecules lock into the $c(4 \times 2)$ structure. The locking-unlocking of the $c(4 \times 2)$ is completely reversible as has been verified by raising and lowering the pressure around the transition pressure several times. This is shown in Fig. 6.2.

NO interacts strongly with the tungsten tip used to obtain the images. The tip was found to be very unstable when scanning both in an NO pressure and with NO preadsorbed onto the surface compared to scanning on the clean Pd(111) surface. The strong interaction of the NO with the tip, and the frequent tip changes had some effect on the acquired images. This is illustrated in Fig. 6.3. The tip effect is much less dramatic than in the O/Pd(111) and NiAl(110) cases. The $c(4 \times 2)$ unit cell of the NO overlayer is imaged in all situations, but the details of the protrusions are influenced. In (a) the protrusions are spherical, in (b) they are elongated in the [112] direction contrary to (c) where they are elongated in the direction perpendicular to [112]. In (d) the center protrusions are connected in the [112] direction.

We believe that the different appearances of the STM images are due to changes in the nature of the tip, including whether or not NO was incorporated in the tip apex. No correlation with tunnel parameters was found. Below STM images of the $p(2 \times 2)$ structure are presented which also appear in different ways. A similar situation is observed for S/Re(0001) which was investigated experimentally and theoretically by Sautet *et al.* [122]. From STM image simulations where the structure and composition of the tip were taken into account, Sautet *et al.* showed that the detailed tip structure clearly affected the shape of the imaged protrusions.

Two different heights are found on the STM image in Fig. 6.3. The center protrusion in the $c(4 \times 2)$ rectangular unit cell is depressed with respect to the corner protrusions. This is shown in the line scan of the unit cell diagonal in (a). The center protrusion is found to be centered in (a), (c) and (d), but is slightly off center in the [112] direction in (b).

6.3.2 Adsorption at low temperature

Adsorption of NO onto Pd(111) between 150 K and 200 K is a little more complex than adsorption at room temperature, as the NO coverage can be increased beyond half a monolayer as adsorbed in the $c(4 \times 2)$ structure.

At first the $c(4 \times 2)$ structure is developed; however, already after a few Langmuir areas with both the $c(4 \times 2)$, a $p(2 \times 2)$ and a transient $c(8 \times 2)$ struc-

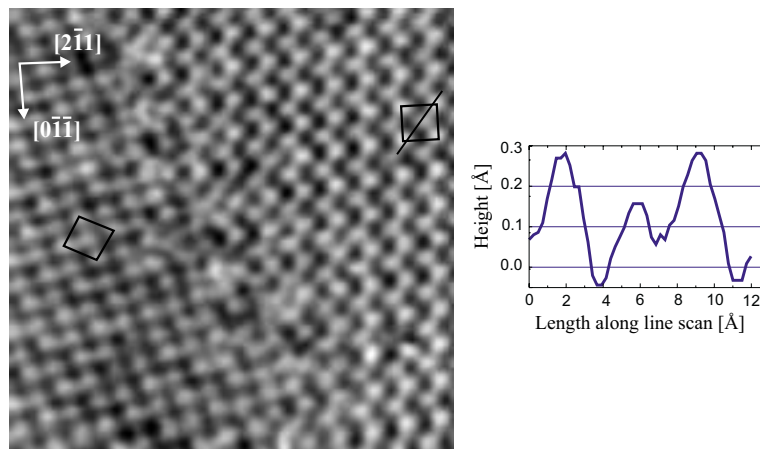


Figure 6.4: STM images of the $c(4 \times 2)$ NO/Pd(111) structure acquired at 200 K after 25 L of NO predosed onto the surface. Rectangles indicate $c(4 \times 2)$ unit cell. $70 \times 70 \text{ \AA}^2$, $U_s = 111 \text{ mV}$, $I_t = 1.0 \text{ nA}$. Line scan is along the unit cell diagonal, as indicated on the image. The image was obtained in the same preparation as the image in Fig. 6.5(a)

ture are found to coexist. The $c(8 \times 2)$ structure was only observed coexisting with the other two ordered structures, and never as a complete overlayer. By prolonged exposure the surface can be covered entirely by the $p(2 \times 2)$ overlayer structure. This is, however, a rather slow process and requires an NO pressure of 1×10^6 torr for several minutes before it can be completed. A similar behaviour has been reported from a LEED study by Conrad *et al.* [117].

An STM image of the $c(4 \times 2)$ structure acquired at 200 K is presented in Fig. 6.4. The surface has been exposed to 25 L, and areas with a $p(2 \times 2)$ overlayer have already built up. This is shown in Fig. 6.5(a) which was obtained during the same preparation. The $p(2 \times 2)$ overlayer builds up in domains which are elongated along one of the close-packed directions of the underlying Pd(111) substrate; the bright protrusions form a (2×2) periodicity and are in registry on the entire surface.

Figures 6.5(b) and (c) show different appearances of the overlayer; again the difference is attributed to a tip effect. Line scans along the diagonal of the

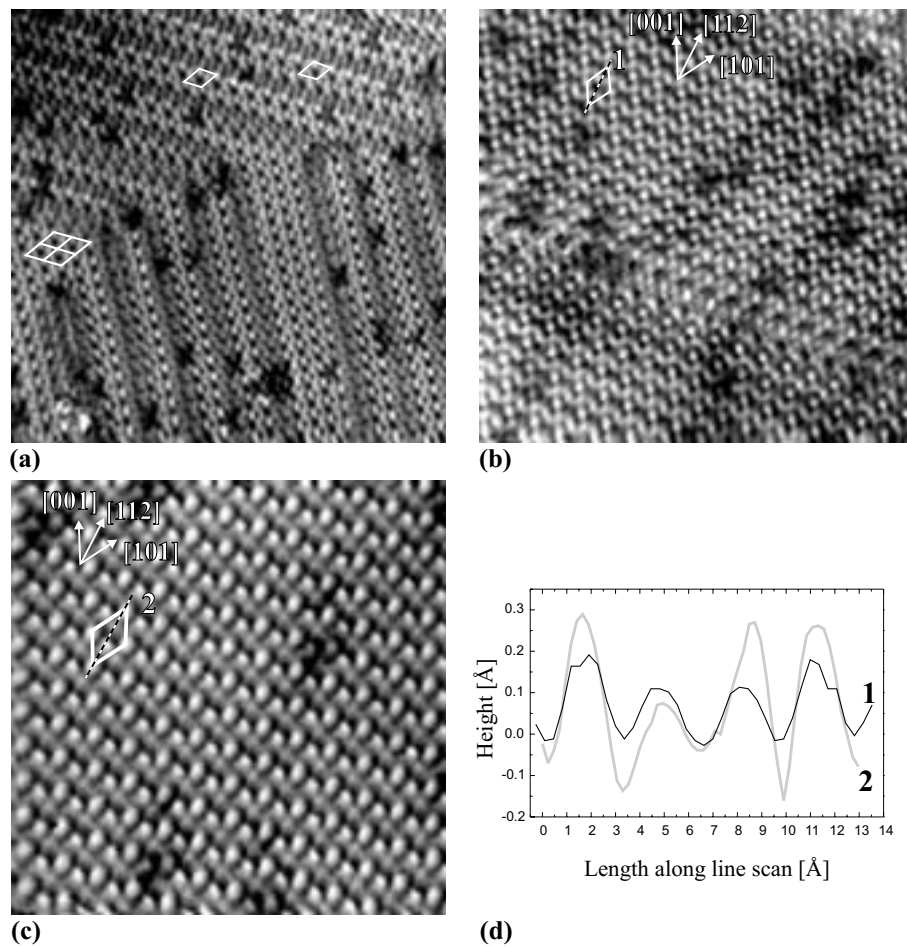


Figure 6.5: STM images of the $p(2 \times 2)$ NO/Pd(111) structure acquired at ~ 200 K. $p(2 \times 2)$ unit cells indicated. (a) Predose of 25 L. $150 \times 150 \text{ \AA}^2$, $U_s = -313$ mV, $I_t = -0.9$ nA. (b) NO pressure of 1×10^{-6} torr, total exposure is 1500 L. $100 \times 100 \text{ \AA}^2$, $U_s = -55$ mV, $I_t = -1.5$ nA. (c) Predose of 2000 L. $70 \times 70 \text{ \AA}^2$, $U_s = 66$ mV, $I_t = 1.3$ nA. (d) Line scan along the unit cell diagonal as indicated in (b) and (c).

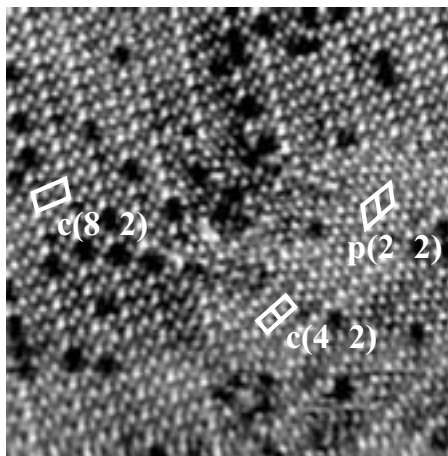


Figure 6.6: STM image of the $c(8 \times 2)$ NO/Pd(111) structure obtained at 170 K with an NO pressure of 5×10^{-7} torr. Total exposure is 200 L. $150 \times 150 \text{ \AA}^2$, $U_s = 625 \text{ mV}$, $I_t = 1.5 \text{ nA}$.

$p(2 \times 2)$ unit cell are presented in Fig. 6.5(d). In the images a $p(2 \times 2)$ lattice is spanned by spherical protrusions. The additional protrusions in Fig. 6.5 (b) form zigzag rows slightly depressed with respect to the spherical protrusions, whereas the additional protrusions in Fig. 6.5(c) are resolved into blobs. The line scans diagonally through the unit cells are rather different in the two cases.

As already mentioned Fig. 6.4 and Fig. 6.5(a) were obtained during the same preparation but at two different places on the surface, showing that the $c(4 \times 2)$ and $p(2 \times 2)$ structures coexist in a certain coverage regime. Figure 6.6 was obtained after an NO exposure of 200 L. It shows an area where the main part is covered with a $c(8 \times 2)$ structure, but in which both the $c(4 \times 2)$ and the $p(2 \times 2)$ structures are also present, clearly showing that these three structures coexist.

In Figs. 6.5(a) and 6.6 black holes are observed. The black holes are assigned to missing NO molecules. They diminish in number with increased exposure and can be completely removed in the saturated $p(2 \times 2)$ structure, as in Figs. 6.5(b) and (c).

6.4 DFT calculations

In order to investigate the preferred NO adsorption sites and the development of the overlayer at increasing coverages, DFT calculations were performed by B. Hammer and Ž. Šljivančanin using the GGA-PW91 functional. The theoretical findings are summarized here, but they will be presented in their full extent in Ref. [V].

The NO chemisorption energies have been calculated for different site configurations of the $c(4\times 2)$, the $p(2\times 2)$ and the $c(8\times 2)$ structures, and the structures with the minimum total energy have been found. These structures are shown in Fig. 6.1(b). The $c(4\times 2)$ structure consists of NO molecules in adjacent HCP and FCC sites. The $p(2\times 2)$ and $c(8\times 2)$ structures consist of NO molecules occupying HCP, FCC and atop sites. The calculated NO chemisorption energies of the three structures are:

Structure	E_{chem} (energy [eV]/NO)
$c(4\times 2)$ ($\theta = 1/2$ ML)	-2.03
$c(8\times 2)$ ($\theta = 5/8$ ML)	-1.83
$p(2\times 2)$ ($\theta = 3/4$ ML)	-1.65

The coverage increases from the $c(4\times 2)$ structure to the $c(8\times 2)$ structure and to the $p(2\times 2)$ structure, but the chemisorption energy decreases. This is due to repulsive adsorbate-adsorbate interaction. This repulsion is probably responsible for governing the slow completion of the $p(2\times 2)$ overlayer structure observed in the STM measurements. Moreover, the molecule chemisorption energy decreases linearly with increasing coverage. In particular, the total energy of an ensemble of NO molecules on Pd(111) is practically the same if all the molecules form a $c(8\times 2)$ overlayer, or if one half of the molecules form a $c(4\times 2)$ overlayer and the other half a $p(2\times 2)$ overlayer. This explains why coexistence of the $c(4\times 2)$, $c(8\times 2)$ and $p(2\times 2)$ domains, as found in the STM experiments, is possible.

6.5 Discussion of the obtained STM images

The $c(4\times 2)$ structure was earlier proposed to be comprised of NO molecules adsorbed into either bridge sites [117–119] or atop sites [120]. This is not consistent with the STM images which show a structure with two different adsorption heights. The obtained STM images are only consistent with adsorption into

the mixture of threefold hollow FCC and HCP sites, or into atop mixed with threefold hollow sites. It is unfortunately not possible to distinguish between these two situations in a simple analysis of the positions within the unit cell. The DFT calculations favor the HCP-FCC threefold hollow site mixture, but the clear, apparent height difference observed on the images for the two species cannot readily be understood in this situation.

In the case of CO on Ni(111) [123], a very similar situation is encountered, i.e. the images were acquired in a high CO pressure. The observed $c(4\times 2)$ structure clearly showed two distinct species in the STM images and line scans along the unit cell diagonal were similar to the ones presented here. For CO/Ni(111) a mixture of threefold HCP and FCC sites was also proposed, and the difference in apparent height was explained in terms of adsorbate-induced buckling of the substrate. In the calculations by Hammer and Šljivančanin even though the two uppermost Pd layers were free to relax, only very little relaxation is observed.

The $p(2\times 2)$ structure has been modeled as adsorption into either atop sites [119, 120] or bridge sites [117]. Again the STM images show adsorption into different sites, as also found in DFT calculations. The $c(8\times 2)$ structure has been proposed to be comprised of adsorption into a mixture of bridge and atop sites by Chen and Goodman [119].

In order to reconcile the STM images with the calculated structures it would be necessary to perform image simulations which include the tip structure and composition. Simple image simulations using only the LDOS of the substrate and a Tersoff-Hamann scheme are not sufficient to explain neither the large height difference between adjacent FCC and HCP hollow sites in the $c(4\times 2)$ and $p(2\times 2)$ structures, nor the large diversity in the observed images. From simple analysis of the positions of the protrusions on the STM images and comparison with the DFT structure shown in Fig. 6.1(b) fairly good agreement is found.

6.6 Nitric oxide adsorption on the Pd nanocrystals

We now turn to NO adsorption on nanocrystals. In the light of the difficulties in imaging nanocrystals with atomic resolution combined with the strong NO tip interaction, STM studies of NO adsorption on Pd nanocrystals are quite challenging. A series of STM images at different NO pressures are presented

in Fig. 6.7.

When scanning on a Pd nanocrystal with NO present in the background, the course of action with respect to stabilizing the overlayer is similar to NO adsorption on an extended Pd(111) surface as described in section 6.3.1. At low NO pressures only diffuse, noisy images can be obtained, but as the pressure is raised, the overlayer at some point stabilizes.

In Fig. 6.7(a) an image has been acquired at an NO pressure of 1×10^{-7} torr. The lattice of the top facet is resolved, but only poorly and with a lot of noise. The noise is most likely due to NO diffusing in and out of the tunnel junction. Ignoring the edges for a moment, the appearance of the top facet is as expected as the NO pressure is below 3×10^{-6} torr – the stabilization pressure of NO on Pd(111). In Fig. 6.7(b), the NO pressure has been increased above the critical pressure to 5×10^{-6} torr, and now a $c(4 \times 2)$ overlayer is stabilized.

In Fig. 6.7(c), an STM image of the cluster with an NO pressure of 5×10^{-5} torr is shown. Here a well-resolved $c(4 \times 2)$ overlayer is observed. The enhanced resolution of the image in (c) with respect to that of (b) is probably unrelated to the pressure; most likely a small tip change has occurred between the two images. The appearance of the NO overlayer in Fig. 6.7(c) is different from the one presented in Fig. 6.3. The protrusions are elongated and only small and random intensity variations are observed. In both cases the overlayers possess $c(4 \times 2)$ symmetry. The different appearance of the overlayer compared to Fig. 6.3 can again be ascribed to the tip. A model of an NO overlayer on the top facet of a Pd nanocrystal is presented in Fig. 6.7(d). It is proposed that the origin of the zigzag rows is that adjacent FCC and HCP hollow sites are incompletely resolved.

In the image in Fig. 6.7(a) it can be seen that NO forms stable protrusions at the edges at a lower pressure than the stabilization pressure of the $c(4 \times 2)$ overlayer. This can be understood from the relationship between the d -band center and the adsorption strength, as briefly discussed in section 5.4. The edge protrusions are not regular in neither spacing, nor intensity. This is in contrast to the oxygen-induced edge protrusions discussed in section 5.7. The irregularities are not yet understood.

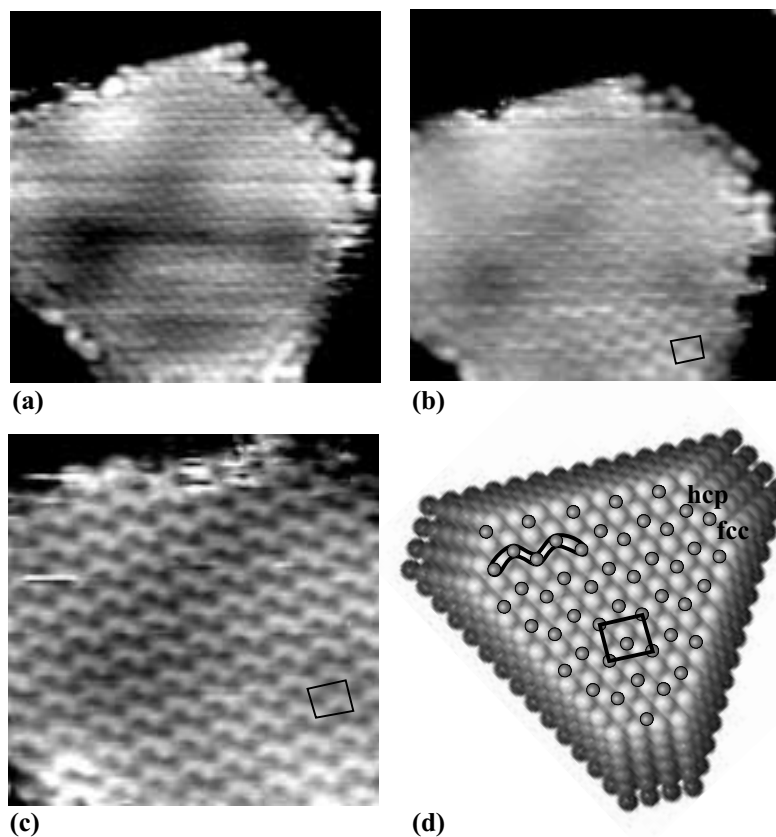


Figure 6.7: STM images of a Pd nanocrystal in different NO pressures acquired at room temperature. Rectangles indicate $c(4 \times 2)$ unit cell. (a) $p = 1 \times 10^{-7}$ torr $70 \times 70 \text{ \AA}^2$, $U_s = 17 \text{ mV}$, $I_t = 0.8 \text{ nA}$. (b) $p = 5 \times 10^{-6}$ torr $70 \times 70 \text{ \AA}^2$, $U_s = 17 \text{ mV}$, $I_t = 0.8 \text{ nA}$. (c) $p = 5 \times 10^{-5}$ torr $50 \times 50 \text{ \AA}^2$, $U_s = 2.1 \text{ mV}$, $I_t = 0.9 \text{ nA}$. (d) Ball model of the $c(4 \times 2)$ NO overlayer.

6.7 Conclusion

The present chapter has dealt mainly with NO adsorption on Pd(111), but also with NO adsorption on the nanocrystals. STM images were obtained of all ordered structures of NO/Pd(111) reported in the literature, including the $c(8\times 2)$ structure. The $c(8\times 2)$ was shown to be a transient structure coexisting with the $c(4\times 2)$ and $p(2\times 2)$ structures. Its transient nature has been explained with the help of DFT calculations.

Nitric oxide adsorption on the nanocrystals was also studied. This turned out to be an almost impossible task due to the strong interaction between NO and the tip, making the tip extremely unstable. It was, however, possible to obtain images which show that, like on Pd(111), a $c(4\times 2)$ structure builds up on the (111) top facet.

Conclusion and outlook

Each chapter contains a conclusion concerning the results presented therein. This conclusion is broader and only concerned with the main results of the entire thesis, especially those which may serve as a basis for future experiments.

Palladium nanoclusters supported on $\text{Al}_2\text{O}_3/\text{NiAl}(110)$ is a versatile model catalytic system, which has been and still is studied extensively (see e.g. Ref. [25] and references therein). The main part of these investigations applies averaging techniques, e.g. electron and photon spectroscopies. The work presented in this thesis is complementary to these studies as emphasis has been on local characterization at the atomic-scale.

Many different aspects of the system: $\text{Pd}/\text{Al}_2\text{O}_3/\text{NiAl}(110)$ have been investigated and presented in this thesis, but focus has been on three aspects of the Pd nanocrystals: atomically resolved imaging of clean nanocrystals, the crystal shape, and atomically resolved adsorption studies of O_2 and NO on nanocrystals.

The atomically resolved images of the Pd nanocrystal, as presented in chapter 4, are the first STM images published of atomic resolved nanosize metal clusters supported on an oxide. It was possible to obtain resolution on both the top facet and a few layers down on the side facets thereby providing a positive determination of the entire nanocrystal shape.

The overall shape of the nanocrystals was analyzed in terms of the Wulff construction, and it was found that the nanocrystals possess their equilibrium shape. This conclusion enabled us to extract a value for the adhesion energy of the system, a quantity which is not easily accessible with other methods. The adhesion energy was compared to and found in variance with a recent theoretical value derived from DFT. Possible reasons for this discrepancy were discussed. The important point, however, is not whether agreement could be achieved or not, but rather that the field of metal-on-oxide studies, both experimentally and theoretically, has reached a level where atomic-scale quantities can be accessed from both points of view, such that a synergy effect can be established.

The atomic-resolution on the top facet opens up opportunities of atomically resolved chemistry on top of a nanocrystal. Here adsorption studies of O_2 and NO were conducted. While the interpretation of the oxygen adsorption studies is hampered by a large tip influence, it was shown for both adsorbates that

the top facet overlayers were similar to those on a Pd(111) surface. Oxygen, however, had a clear influence on the nanocrystal edges. With the help of DFT calculations this could be ascribed to oxygen-induced edge reconstruction. For NO, only little effect could be detected on the edges. Both O and NO overlayers were found to be unstable on the nanocrystals at RT, and the experiments had to be performed in a background pressure. This is undesirable for controlled reaction studies, where it is preferable to adsorb the first species and then react it away with the second. Such studies may be achieved at low temperature. Low temperature investigations were also conducted on the nanocrystals, but for CO adsorption. The low temperature experiments were, however, extremely difficult due to extensive piezo creep and were therefore not pursued (or included in the thesis). As reactions on nanosize systems are of general interest, it would be interesting to resume atomically resolved imaging at low temperatures. This would require the development of an experimental procedure to minimize or circumvent piezo creep. Another possibility could be to conduct experiments on a species which is stable on Pd at room temperature, e.g. sulfur, which is also an important reactant in catalytic reactions such as formation of thiophene from acetylene [124].

Strain may have a large influence on the reactivity of a metal [20,21]. The Pd nanocrystals were too large to exhibit any overall strain, and the lattice constant in the (111) top facet is equal to the one in a (111) bulk plane. A possible candidate for a system where strain effects as well as edge effects may be present on clusters large enough for atomically resolved imaging, are the halfway incorporated flat clusters, which can be obtained when Pd is deposited at elevated temperatures.

Together with atomically resolved chemistry on the top facet of a cluster, the subject with the largest future prospects is *in-situ* high-pressure measurements. While atomically resolved STM studies of adsorption on extended single crystal metal surfaces can be realized in a high-pressure ambient [125,126], atomically resolved reaction and adsorption studies on supported nanocrystals may be out of reach; but other and equally interesting phenomena can be probed which does not require the high resolution, e.g. cluster reshaping, as evidenced in *ex-situ* HRTEM for oxygen on Pd/MgO, and cluster mobility leading to a redistribution and/or sintering, as recently observed in *ex-situ* STM for Au and Ag on TiO₂ [26], and wetting non-wetting transition as shown in EXAFS for Cu/ZnO [127]. Such effects are all accompanied by a change in the active surface area, and are therefore of interest for the development of catalysts which maintain the highest possible surface area during operation.

Summary

The present thesis is a scanning tunneling microscopy (STM) study of Pd nanoclusters dispersed on a thin aluminum oxide film supported on a NiAl alloy single crystal.

In order to control the structure at the atomic level as well as the purity of the system, the predominant part of the experiments are conducted under ultra-high vacuum conditions. The operation mode of the STM will not be given here, the important part is that the STM under certain conditions allows imaging of single atoms and molecules in a surface.

The main motivation for the present study is that nanosize metal clusters dispersed on a model oxide support has a fundamental resemblance to a broad class of real catalytic materials, the so-called metal-on-oxide catalysts.

A catalyst is a substance that accelerates the rate of a chemical reaction without being part of the final product. Apart from the interesting physics and chemistry behind the accelerated rate, detailed knowledge of the catalytic process is also desirable due to a significant impact on society from catalysis. This can be illustrated with the catalyst's almost ubiquitous role in minimizing environmental pollution products caused by industry and the modern way of living, ranging from cleaning toxic fumes from industrial plants to the exhaust from the ever increasing number of cars.

Real catalysts are extremely complex materials consisting of porous and rough oxide support where nanosize metal clusters are dispersed in the surface region. The catalytic reactions are often performed at extreme conditions with total pressures up to several hundreds of bar, temperatures of some hundred degrees Celsius and gas speed up to a few thousand km/h. This hampers a characterization of a realistic catalyst at the atomic level. The interesting and important basic steps can be addressed by representing the catalyst with an idealized model system. Traditionally the model system of choice has been single crystal metal surfaces. Whereas a lot has been learned and still can be learned from single crystal studies, the surface science community has now developed the tools to include studies of more realistic sample surfaces such as the oxide-supported nanosize metal clusters. The characterization of a such system at the atomic level, is the subject of this thesis.

The first two chapters deal with the support. This part of the system serves as a model system for the porous and rough oxide support present in

real catalysts. The model system is thus quite idealized as the Al_2O_3 film on top of the metal support is fairly well-ordered and very flat. The main point is, however, that Al_2O_3 is in itself non-conducting, and it is only through the close proximity of the metal substrate that the use of STM is made possible.

The NiAl surface can in principle be regarded as “just” the substrate of the thin aluminum oxide film, but we have gone beyond that opinion, and two interesting phenomena taking place at the surface have been described: (i) That even though both Al and Ni are present in the surface, the STM only depicts the Al atoms, and (ii) the presence of standing waves at room temperature. These two phenomena were understood with the help of electronic structure calculations which became available through a cooperation with theorists.

The Al_2O_3 film has a complex and fascinating appearance when depicted by the STM; this appearance was described rather detailed. An general type of measurements with the STM is size measurements. In such measurements it is important to know the reference level (the zero point) in order to determine the height of an object. This reference level was systematically investigated on the film as a function of the tunnel conditions, and a clear dependence was found. This is an important effect which may distort height measurements of supported metal clusters if not taken properly into account. A simple model has been presented which explains the observed dependence.

The main part of the work presented in this thesis is concerned with small palladium clusters grown on top of the Al_2O_3 film. Palladium was chosen for several reasons, one important reason being that nanosize palladium clusters supported on the surface aluminum oxide is an important catalytic material, e.g. in the car exhaust catalyst. Another important reason is that when palladium is deposited on to the Al_2O_3 film at room temperature, a large fraction of the small clusters are perfectly well-ordered. These clusters are referred to as nanocrystals. An investigation of nanocrystals is again an idealization, as real catalytic clusters may possess a variety of shapes, which may even change during reaction conditions. Even though we demonstrated that atomic resolution could be obtained of the surface of both semi-ordered clusters and well-ordered clusters (nanocrystals), atomically resolved studies of nanocrystals are much more transparent and the emphasis was on these clusters. On the nanocrystals, atomic resolution was obtained both on the top facet as well as down on the side facets, allowing for a complete crystallographic identification of the entire nanocrystal.

The nanocrystals were also characterized with respect to their overall morphology, and we found that the nanocrystals possessed their thermodynami-

cally most stable shape – the so-called Wulff shape. It was then shown how the cluster shape could be used to derive an important thermodynamical quantity, the adhesion energy, a quantity not easily accessible from other methods. The overall cluster shape was furthermore characterized at elevated temperatures and in a high-pressure ambient, as these conditions are important in order to investigate the system under real reaction condition. While the Pd nanocrystals were found sensitive to even a moderate increase in the temperature, they were observed to be stable under a high-pressure of hydrogen. That the system can be investigated during the presence of high-pressure is a very important point which can be used to explore the connection between idealized model conditions and real catalytic conditions.

In this part of the thesis a small section concerned with various metals on the $\text{Al}_2\text{O}_3/\text{NiAl}(110)$ film is also presented, where e.g. atomic resolution was also demonstrated on Cu nanocrystals.

The final part of the thesis is concerned with atomically resolved studies of adsorption of oxygen and nitric oxide on the nanocrystals. Atomically resolved adsorption (and reaction) studies on nanosize transition-metal clusters are potentially very interesting in order to directly access insight at the atomic-scale into a possible influence on adsorbate structures and reaction rates from the reduced size of the metal. For example, to what extent does the presence of edges and corners influence an overlayer?

Atomic resolution was achieved for both oxygen and nitric oxide overlayers, and it was found in both cases that the overlayer structures were the same as those found on the extended Pd(111) surface. Oxygen, however, had a prominent effect on the nanocrystal edges, which with the help of theoretical calculation could be assigned to an oxygen-induced edge reconstruction. Adsorption studies of both oxygen and nitric oxide were also conducted on the Pd(111) surface in order to compare to and support the finding on the nanocrystals.

References

- [1] G. A. Somorjai, *Introduction to surface chemistry and catalysis* (John Wiley & Sons, Inc., New York, 1994).
- [2] V. E. Henrich and P. A. Cox, *The surface science of metal oxides* (Cambridge University Press, Cambridge, 1994).
- [3] H.-J. Freund, H. Kuhlenbeck, and V. Staemmler, "Oxide surfaces", *Rep. Prog. Phys.* **59**, 283 (1996).
- [4] H.-J. Freund, "Oxide surfaces", *Faraday Discuss.* **114**, 1 (1999).
- [5] S. C. Street, C. Xu, and D. W. Goodman, "The physical and chemical properties of ultrathin oxide films", *Annu. Rev. Phys. Chem.* **48**, 43 (1997).
- [6] R. Franchy, "Growth of thin, crystalline oxide, nitride and oxynitride films on metal and metal alloy surfaces", *Surf. Sci. Rep.* **38**, 195 (2000).
- [7] J. M. Thomas and W. J. Thomas, *Principles and practice of heterogeneous catalysis* (VCH, Weinheim, 1997).
- [8] G. Ertl and H.-J. Freund, "Catalysis and surface science", *Physics Today* **52**, 32 (1999).
- [9] M. Shelef and R. W. McCabe, "Twenty-five years after introduction of automotive catalysts: what next?", *Catal. Today* **62**, 35 (2000).
- [10] R. J. Farraotu and R. M. Heck, "Catalytic converters: state of the art and perspectives", *Catal. Today* **51**, 351 (1999).
- [11] S. Senkan, "Combinatorial heterogeneous catalysis—a new path in an old field", *Angew. Chem. Int. Ed.* **40**, 312 (2001).
- [12] D. W. Goodman, "Catalysis: from single crystals to the "real world"", *Surf. Sci.* **299/300**, 837 (1994).
- [13] G. A. Somorjai, "The surface science of heterogeneous catalysis", *Surf. Sci.* **299/300**, 849 (1994).

- [14] C. R. Henry, "Surface studies of supported model catalysts", *Surf. Sci. Rep.* **31**, 231 (1998).
- [15] C. T. Campbell, "Ultrathin metal films and particles on oxide surfaces: structural, electronic and chemisorptive properties", *Surf. Sci. Rep.* **27**, 1 (1997).
- [16] S. Dahl, A. Logadottir, R. C. Egeberg, J. H. Larsen, I. Chorkendorff, E. Tornqvist, and J. K. Nørskov, "Role of steps in N₂ activation on Ru(0001)", *Phys. Rev. Lett.* **83**, 1814 (1999).
- [17] M. Valden, X. Lai, and D. W. Goodman, "Onset of catalytic activity of gold clusters on titania with the appearance of nonmetallic properties", *Science* **281**, 1647 (1998).
- [18] V. P. Zhdanov and B. Kasemo, "Simulations of the reaction kinetics on nanometer supported catalyst particles", *Surf. Sci. Rep.* **39**, 25 (2000).
- [19] G. Bamwenda, S. Tsubota, T. Nakamura, and M. Haruta, "The influence of preparation method on the catalytic activity of platinum and gold supported on TiO₂ for CO oxidation", *Cat. Lett.* **44**, 8 (1997).
- [20] M. Gsell, P. Jacob, and D. Menzel, "Effect of substrate strain on adsorption", *Science* **280**, 717 (1998).
- [21] M. Mavrikakis, B. Hammer, and J. K. Nørskov, "Effect of strain on the reactivity of metal surfaces", *Phys. Rev. Lett.* **81**, 2819 (1998).
- [22] F. Besenbacher, "Scanning tunnelling microscopy studies of metal surfaces", *Rep. Prog. Phys.* **59**, 1737 (1996).
- [23] F. M. Leibsle, P. W. Murray, N. G. Condon, and G. Thornton, "Scanning tunnelling microscopy studies of reactions on metal surfaces and model oxide supports", *J. Phys. D* **30**, 741 (1997).
- [24] D. Bonnell, "Scanning tunneling microscopy and spectroscopy of oxide surfaces", *Prog. Surf. Sci.* **57**, 187 (1998).
- [25] M. Bäumer and H.-J. Freund, "Metal deposition on well-ordered oxide films", *Prog. Surf. Sci.* **61**, 127 (1999).

- [26] X. Lai and D. W. Goodman, "Structure-reactivity correlations for oxide-supported metal catalysts: new perspectives from STM", *J. Mol. Cat. A* **162**, 33 (2000).
- [27] M. Bäumer, J. Libuda, A. Sandell, H.-J. Freund, G. Graw, Th. Bertrams, and H. Neddermeyer, "The growth and properties of Pd and Pt on $\text{Al}_2\text{O}_3/\text{NiAl}(110)$ ", *Ber. Bunsenges Phys. Chem.* **99**, 1381 (1995).
- [28] G. Binnig, H. Rohrer, C. Gerber, and E. Weibel, "Surface studies by scanning tunneling microscopy", *Phys. Rev. Lett.* **49**, 57 (1982).
- [29] G. Binnig and H. Rohrer, "Scanning tunneling microscopy – from birth to adolescence", *Rev. Mod. Phys.* **59**, 615 (1987).
- [30] The Nobel committee press release from 1986 can be found at: <http://www.nobel.se/physics/laureates/1986/press.html>.
- [31] J. Tersoff and D. R. Hamann, "Theory and application of the scanning tunneling microscope", *Phys. Rev. Lett.* **50**, 1998 (1983).
- [32] J. Tersoff and D. R. Hamann, "Theory of the scanning tunneling microscope", *Phys. Rev. B* **31**, 805 (1985).
- [33] J. Bardeen, "Tunneling from a many-particle point of view", *Phys. Rev. Lett.* **6**, 57 (1961).
- [34] C. Chen, *Introduction to scanning tunneling microscopy* (Oxford University Press, New York, 1993).
- [35] N. D. Lang, "Vacuum tunneling current from an adsorbed atom", *Phys. Rev. Lett.* **55**, 230 (1985).
- [36] N. D. Lang, "Theory of single-atom imaging in the scanning tunneling microscope", *Phys. Rev. Lett.* **56**, 1164 (1986).
- [37] I. S. Tilinin, M. K. Rose, J. C. Dunphy, M. Salmeron, and M. A. V. Hove, "Identification of adatoms on metal surfaces by STM: experiment and theory", *Surf. Sci.* **418**, 511 (1998).
- [38] *Binary alloy phase diagrams*, 2nd ed., edited by T. B. Massalski (ASM International, Ohio, 1992).

- [39] H. L. Davis and R. Noonan, “Rippled relaxation in the (110) surface of the ordered metallic alloy NiAl”, *Phys. Rev. Lett.* **54**, 566 (1985).
- [40] S.-C. Lui, J. W. Davenport, E. W. Plummer, D. M. Zehner, and G. W. Fernando, “Electronic structure of NiAl”, *Phys. Rev. B* **42**, 1582 (1990).
- [41] N. D. Lang, “Apparent size of an atom in the scanning tunneling microscope as a function of bias”, *Phys. Rev. Lett.* **58**, 45 (1987).
- [42] L. Petersen, Ph. Hoffmann, E. W. Plummer, and F. Besenbacher, “Fourier transform-STM: determining the surface Fermi contour”, *J. Elec. Spec. Rel. Phen.* **109**, 97 (2000).
- [43] L. Petersen, *Scanning tunneling microscopy studies of the electronic structure of metal surfaces*, Ph.D. thesis, University of Århus, Århus, Denmark, 1999.
- [44] A. Zangwill, *Physics at surfaces* (Cambridge University Press, Cambridge, 1988).
- [45] L. Petersen, P. T. Sprunger, Ph. Hofmann, E. Lægsgaard, B. G. Briner, M. Doering, H.-P. Rust, A. M. Bradshaw, F. Besenbacher, and E. W. Plummer, “Direct imaging of the two-dimensional Fermi contour: Fourier-transform STM”, *Phys. Rev. B* **57**, R6858 (1998).
- [46] L. Petersen, P. Laitenberger, E. Lægsgaard, and F. Besenbacher, “Screening waves from steps and defects on Cu(111) and Au(111) imaged with STM: contribution from bulk electrons”, *Phys. Rev. B* **58**, 7361 (1998).
- [47] S.-C. Lui, M. H. Kang, E. J. Mele, and E. W. Plummer, “Surface states on NiAl(110)”, *Phys. Rev. B* **39**, 13149 (1989).
- [48] Z. Song, J. I. Pascual, H. Conrad, K. Horn, and H.-P. Rust, “Imaging surface electronic structure of NiAl(110) using low temperature scanning tunneling microscopy”, *App. Phys. A*. Accepted, (2001).
- [49] B. C. Lippens and J. J. Steggerda, “Active alumina”, in *Physical and chemical aspects of adsorbents and catalysts*, edited by B. G. Linsen (Academic Press, London, 1970), pp. 171–208.
- [50] P. Gassmann, R. Franchy, and H. Ibach, “Investigations on phase transitions within thin Al₂O₃ layers on NiAl(001) - HREELS on aluminum oxide films”, *Surf. Sci.* **319**, 95 (1994).

- [51] S. Blonski and S. H. Garofalini, "Molecular dynamics simulations of α -alumina and γ -alumina surfaces", *Surf. Sci.* **295**, 263 (1993).
- [52] H.-J. Freund, M. Bäumer, J. Libuda, H. Kuhlenbeck, T. Risse, K. Al-Shamery, and H. Hamann, "Metal aggregates on oxide surfaces: structure and adsorption", *Cryst. Res. Technol.* **33**, 977 (1998).
- [53] X. Lai, C. C. Chusuei, K. Luo, Q. Guo, and D. W. Goodman, "Imaging ultrathin Al_2O_3 films with scanning tunneling microscopy", *Chem. Phys. Lett.* **330**, 226 (2000).
- [54] J. Libuda, F. Winkelmann, M. Bäumer, H.-J. Freund, T. Bertrams, H. Neddermeyer, and K. Müller, "Structure and defects of an ordered alumina film on $\text{NiAl}(110)$ ", *Surf. Sci.* **318**, 61 (1994).
- [55] S. G. Addepalli, B. Ekstrom, N. P. Magtoto, J.-S. Lin, and J. A. Kelber, "STM atomic-scale characterization of the γ' - Al_2O_3 film on $\text{Ni}_3\text{Al}(111)$ ", *Surf. Sci.* **442**, 385 (1999).
- [56] A. Rosenhahn, J. Schneider, C. Becker, and K. Wandelt, "Oxidation of $\text{Ni}_3\text{Al}(111)$ at 600, 800, and 1050 K investigated by scanning tunneling microscopy", *J. Vac. Sci. Technol. A* **18**, 1923 (2000).
- [57] R. M. Jaeger, H. Kuhlenbeck, H.-J. Freund, M. Wuttig, W. Hoffmann, R. Franchy, and H. Ibach, "Formation of a well-ordered aluminium oxide overlayer by oxidation of $\text{NiAl}(110)$ ", *Surf. Sci.* **259**, 235 (1991).
- [58] S. Stempel. Private communication.
- [59] M. Bäumer. Private communication.
- [60] C. T. Campbell and S. M. Valone, "Design considerations for simple gas dosers in surface science applications", *J. Vac. Sci. Technol. A* **3**, 408 (1985).
- [61] H. Isern and G. R. Castro, "The initial interaction of oxygen with a $\text{NiAl}(110)$ single crystal: a LEED and AES study", *Surf. Sci.* **211/212**, 865 (1989).
- [62] M. B. Lee, J. H. Lee, B. G. Frederick, and N. V. Richardson, "Surface structure of ultra-thin Al_2O_3 films on metal substrates", *Surf. Sci.* **448**, L207 (2000).

- [63] A. Bogicevic and D. R. Jennison, "Variations in the nature of metal adsorption on ultrathin Al_2O_3 films", *Phys. Rev. Lett.* **82**, 4050 (1999).
- [64] D. R. Jennison and A. Bogicevic, "Ultrathin aluminum oxide films: Al-sublattice structure and the effect of substrate on ad-metal adhesion", *Surf. Sci.* **464**, 108 (2000).
- [65] S. Stempel, *Nukleation, Wachstum und Struktur kleiner Metallpartikel auf einer geordneten Aluminiumoxidunterlage*, Ph.D. thesis, Freien Universität, Berlin, Germany, 1998.
- [66] S. Andersson, P. A. Brühwiler, A. Sandell, M. Frank, J. Libuda, A. Giertz, B. Brena, A. J. Maxwell, H.-J. Freund, and N. Mårtensson, "Metal-oxide interaction for metal clusters on a metal-supported thin alumina film", *Surf. Sci.* **442**, L964 (1999).
- [67] A. Y. Lozovoi, A. Alavi, and M. W. Finnis, "Surface stoichiometry and the initial oxidation of $\text{NiAl}(110)$ ", *Phys. Rev. Lett.* **85**, 610 (2000).
- [68] M. Bäumer, M. Frank, M. Heemeier, R. Kühnemuth, S. Stempel, and H.-J. Freund, "Nucleation and growth of transition metals on thin alumina film", *Surf. Sci.* **454-456**, 957 (2000).
- [69] Th. Bertrams, A. Brodde, and H. Neddermeyer, "Tunneling through an epitaxial film: Al_2O_3 on $\text{NiAl}(110)$ ", *J. Vac. Sci. Technol. B* **12**, 2122 (1994).
- [70] *Chemisorption and reactivity on supported clusters and thin films*, edited by R. Lambert and P. Pacchioni (Kluwer Academic Publishers, Dordrecht, 1997).
- [71] J. A. Venables, "Atomic processes in crystal growth", *Surf. Sci.* **299/300**, 798 (1994).
- [72] O. Dulub, W. Hebenstreit, and U. Diebold, "Imaging cluster surfaces with atomic resolution: the strong metal-support interaction state of Pt supported on $\text{TiO}_2(110)$ ", *Phys. Rev. Lett.* **84**, 3646 (2000).
- [73] M. Bäumer, J. Biener, and R. J. Madix, "Growth, electronic properties and reactivity of vanadium deposited onto a thin alumina film", *Surf. Sci.* **432**, 189 (1999).

- [74] I. V. Markov, *Crystal growth for beginners* (World Scientific, Singapore, 1995).
- [75] C. Herring, “The use of classical macroscopic concepts in surface energy problems”, in *structure and properties of solid surfaces*, edited by R. Gomer and C. S. Smith (The University of Chicago Press, Chicago, 1953), pp. 5–82.
- [76] G. Wulff, “Zur Frage der Geschwindigkeit der Wachstums und der Auflösung der Krystallflächen”, *Z. Kristallogr.* **34**, 449 (1901).
- [77] W. L. Winterbottom, “Equilibrium shape of a small particle in contact with a foreign substrate”, *Acta Metall.* **15**, 303 (1967).
- [78] W. R. Tyson and W. A. Miller, “Surface free energies of solid metals: estimation from liquid surface tension measurements”, *Surf. Sci.* **62**, 267 (1977).
- [79] C. R. Henry, C. Chapon, S. Giorgio, and C. Goyhenex, in *Chemisorption and reactivity on supported clusters and thin films*, edited by R. Lambert and G. Pacchioni (Kluwer Academic Publishers, Dordrecht, 1997), pp. 117–152.
- [80] G. D’Agostino, A. Pinto, and S. Mobilio, “Simulated gold clusters and relative extended x-ray-absorption fine-structure spectra”, *Phys. Rev. B* **48**, 14447 (1993).
- [81] C. Henry, “Growth, structure and morphology of supported metal clusters studied by surface science techniques”, *Cryst. Res. Technol.* **33**, 1119 (1998).
- [82] L. Vitos, A. V. Ruban, H. L. Skriver, and J. Kollár, “The surface energy of metals”, *Surf. Sci.* **411**, 186 (1998).
- [83] J. S. Villarrubia, “Morphological estimation of tip geometry for scanned probe microscopy”, *Surf. Sci.* **321**, 287 (1994).
- [84] D. J. Keller and F. S. Franke, “Envelope reconstruction of probe microscope images”, *Surf. Sci.* **294**, 409 (1993).
- [85] S. Stempel, M. Bäumer, and H.-J. Freund, “STM studies of rhodium deposits on an ordered alumina film – resolution and tip effects”, *Surf. Sci.* **402-404**, 424 (1998).

- [86] Th. Bertrams, F. Winkelmann, Th. Uttich, H.-J. Freund, and H. Neddermeyer, "Structural characterization of a model catalyst: Pt/Al₂O₃/NiAl(110)", *Surf. Sci.* **331-333**, 1515 (1995).
- [87] M. Tinkham, "Coulomb blockade and an electron in a mesoscopic box", *Am. J. Phys.* **64**, 343 (1996).
- [88] P. J. M. van Bentum, R. T. M. Smokers, and H. van Kempen, "Incremental charging of single small particles", *Phys. Rev. Lett.* **60**, 2543 (1988).
- [89] *Handbook of chemistry and physics*, 72nd ed., edited by D. R. Lide (CRC Press, Boston, 1991-1992).
- [90] M. Amman, R. Wilkins, E. Ben-Jacob, P. D. Maker, and R. C. Jaklevic, "Analytic solution for the current-voltage characteristic of two mesoscopic tunnel junctions coupled in series", *Phys. Rev. B* **43**, 1146 (1991).
- [91] M. Klimenkov, S. Nepijko, H. Kuhlenbeck, M. Bäumer, R. Schlögl, and H.-J. Freund, "The structure of Pt-aggregates on a supported thin aluminum oxide film in comparison with unsupported alumina: a transmission electron microscopy study", *Surf. Sci.* **391**, 27 (1997).
- [92] S. A. Nepijko, M. Klimenkov, M. Adelt, H. Kuhlenbeck, R. Schlögl, and H.-J. Freund, "Structural investigations of Pd clusters on γ -Al₂O₃(111)/NiAl(110) with transmission electron microscopy", *Langmuir* **15**, 5309 (1999).
- [93] M. Methfessel, D. Henning, and M. Scheffler, "Trends of the surface relaxations, surface energies, and work function of the 4d transition metals", *Phys. Rev. B* **46**, 4816 (1992).
- [94] *Cohesion in metals*, edited by F. R. de Boer, R. Boom, W. C. M. Mattens, A. R. Miedema, and A. K. Niessen (North-Holland Physics Publishing, Amsterdam, The Netherlands, 1988).
- [95] M. W. Finnis, "The theory of metal-ceramic interfaces", *J. Phys. C* **8**, 5811 (1996).
- [96] A. Sandell, J. Libuda, M. Bäumer, and H.-J. Freund, "Metal deposition in adsorbate atmosphere: growth and decomposition of a palladium carbonyl-like species", *Surf. Sci.* **346**, 108 (1996).

- [97] P. Müller and R. Kern, "Equilibrium shape of epitaxially strained crystals (Volmer-Weber case)", *J. Cryst. Growth* **193**, 257 (1998).
- [98] H.-J. Freund, B. Dillmann, D. Ehrlich, M. Hassel, R. M. Jaeger, H. Kühlenbeck, C. A. V. Jr., F. Winkelmann, S. Wohlrab, C. Xu, Th. Bertrams, A. Brodde, and H. Neddermeyer, "Adsorption and reaction of molecules on surfaces of metal-metal oxide systems", *J. Mol. Cat.* **82**, 143 (1993).
- [99] M. Bäumer, M. Frank, J. Libuda, S. Stempel, and H.-J. Freund, "Growth and morphology of Rh deposits on an alumina film under UHV conditions and under the influence of CO", *Surf. Sci.* **391**, 204 (1997).
- [100] T. Worren. Unpublished.
- [101] P. Thostrup and K. Højrup Hansen. Unpublished.
- [102] M. Heemeier, M. Frank, J. Libuda, K. Wolter, H. Kühlenbeck, M. Bäumer, and H.-J. Freund, "The influence of OH groups on the growth of rhodium on alumina: a model study", *Cat. Lett.* **68**, 19 (2000).
- [103] M. Heemeier and K. Højrup Hansen. Unpublished.
- [104] A. Steltenpohl and N. Memmel, "Adsorption site of oxygen on Pd(111)", *Surf. Sci.* **443**, 13 (1999).
- [105] F. P. Leisenberger, G. Koller, M. Sock, S. Surnev, M. G. Ramsey, F. P. Netzer, B. Klötzer, and K. Hayek, "Surface and subsurface oxygen on Pd(111)", *Surf. Sci.* **445**, 380 (2000).
- [106] G. Zheng and E. I. Altman, "The oxidation of Pd(111)", *Surf. Sci.* **462**, 151 (2000).
- [107] X. Guo, A. Hoffman, and J. J. T. Yates, "Adsorption kinetics and isotropic equilibrium of oxygen adsorbed on the Pd(111) surface", *J. Chem. Phys.* **90**, 5787 (1989).
- [108] D. Loffreda, D. Simon, and P. Sautet, "Molecular and dissociative chemisorption of NO on palladium and rhodium (100) and (111) surfaces: a density-functional study", *J. Chem. Phys.* **108**, 6447 (1998).
- [109] B. Hammer, "Reactivity of a stepped surface: NO dissociation on Pd(211)", *Faraday Discuss.* **110**, 323 (1998).

- [110] B. Hammer and J. K. Nørskov, "Theory of adsorption and surface reactions", in *Chemisorption and reactivity on supported clusters and thin films*, edited by R. M. Lambert and G. Pacchioni (Kluwer Academic Publishers, Netherland, 1997), pp. 285–351.
- [111] S. Helveg, H. T. Lorensen, S. Horch, E. Lægsgaard, I. Stensgaard, K. W. Jacobsen, J. K. Nørskov, and F. Besenbacher, "Oxygen adsorption on Pt(110)-(1×2): new high-coverage structures", *Surf. Sci.* **430**, L533 (1999).
- [112] H. Tanaka, J. Yoshinobu, and M. Kawai, "Oxygen-induced reconstruction of the Pd(110) surface: an STM study", *Surf. Sci.* **327**, L505 (1995).
- [113] H. Niehus and C. Achete, "Oxygen-induced mesoscopic island formation at Pd(110)", *Surf. Sci.* **369**, 9 (1996).
- [114] B. Brena, G. Comelli, L. Ursella, and G. Paolucci, "Oxygen on Pd(110): substrate reconstruction and adsorbate geometry by tensor LEED", *Surf. Sci.* **375**, 150 (1997).
- [115] K. Yagi and H. Fukutani, "Oxygen adsorption site of Pd(110)c(2×4)-O: analysis of ARUPS compared with STM image", *Surf. Sci.* **412/413**, 489 (1998).
- [116] I. Meusel, J. Hoffmann, J. Hartman, M. Heemeiner, M. Bäumer, J. Libuda, and H.-J. Freund, "The interaction of oxygen with alumina-supported palladium particles", Submitted, (2000).
- [117] H. Conrad, G. Ertl, J. Küppers, and E. E. Latta, "Interaction of NO and O₂ with Pd(111) surfaces. I.", *Surf. Sci.* **65**, 235 (1977).
- [118] M. Bertolo and K. Jacobi, "NO adsorption on Pd(111) in the temperature range between 20 and 300 K", *Surf. Sci.* **226**, 207 (1990).
- [119] P. J. Chen and D. W. Goodman, "Ordered high coverage NO overlayers on Pd(111)", *Surf. Sci.* **297**, L93 (1993).
- [120] D. T. Wickham, B. A. Banse, and B. E. Koel, "Adsorption of nitrogen dioxide and nitric oxide on Pd(111)", *Surf. Sci.* **243**, 83 (1991).
- [121] D. Loffreda, D. Simon, and P. Sautet, "Vibrational frequency and chemisorption site: a DFT-Periodic study of NO on Pd(111) and Rh(111) surfaces", *Chem. Phys. Lett.* **291**, 15 (1998).

- [122] P. Sautet, J. C. Dunphy, D. F. Ogletree, C. Joachim, and M. Salmeron, “Imaging a $p(2 \times 2)$ layer of sulphur on Re(0001) with the scanning tunneling microscope: an experimental and theoretical study of the effect of adsorption site and tip structure”, *Surf. Sci.* **315**, 127 (1994).
- [123] P. T. Sprunger, F. Besenbacher, and I. Stensgaard, “STM investigation of the Ni(111)- $c(4 \times 2)$ -2CO structure”, *Chem. Phys. Lett.* **243**, 439 (1995).
- [124] S. Speller, T. Rauch, J. Böermann, P. Borrmann, and W. Heiland, “Surface structure of S on Pd(111)”, *Surf. Sci.* **441**, 107 (1999).
- [125] J. A. Jensen, K. B. Rider, M. Salmeron, and G. A. Somorjai, “High pressure adsorbate structures studied by scanning tunneling microscopy: CO on Pt(111) in equilibrium with the gas phase”, *Phys. Rev. Lett.* **80**, 1228 (1998).
- [126] L. Österlund, P. B. Rasmussen, P. Thostrup, E. Lægsgaard, I. Stensgaard, and F. Besenbacher, “Bridging the pressure gap in surface science at the atomic level: H/Cu(110)”, *Phys. Rev. Lett.* **86**, 460 (2001).
- [127] B. S. Clausen, J. Schiøtz, L. Gråbæk, C. V. Ovesen, K. W. Jacobsen, J. K. Nørskov, and H. Topsøe, “Wetting/non-wetting phenomena during catalysis: evidence from in situ on-line EXAFS studies of Cu-based catalysts”, *Topics in Catalysis* **1**, 367 (1994).